New Adsorbents for Hydrogen Storage and Fuel Desulfurization

By

Hao Chen

A dissertation submitted in partial fulfillment
of the requirements for the degree of
Doctor of Philosophy
(Chemical Engineering)
in the University of Michigan
2013

Doctoral Committee:

Professor Ralph T. Yang, Chair
Professor Erdogan Gulari
Professor Jwo Pan
Professor Johannes W. Schwank

Table of Contents

List of Figures

List of Tables

Abstract

Energy and environment problems have attracted more and more attention in our society. In order to alleviate the potential energy crisis and environmental pollutions, many sustainable solutions have been proposed, one of which is the development of new alternative energy. Hydrogen is considered as a promising and clean alternative energy source and becomes the focus of many researches. However, its wide applications especially as the fuel to power automotives are limited by many factors, one of which is hydrogen storage issue. This thesis discussed about utilizing adsorbents for hydrogen storage at ambient conditions and tried to overcome several challenges involved in this field.

Recent studies have shown that using the hydrogen spillover phenomena is a promising approach for developing new materials for hydrogen storage at ambient temperature. However, the rates need to be improved. Significant catalytic effects on both spillover (i.e., adsorption) and reverse spillover (i.e., desorption) on Pt-doped carbon by TiF_3 were found. By doping 2 wt% TiF_3 on the Pt-doped Maxsorb (a super-activated carbon), both adsorption and desorption rates were significantly increased while the storage capacity decreased only slightly due to decreased surface areas. The effect of the heat-treatment temperature (473K vs. 673K) of the doped TiF_3 on its catalytic effects was also studied. XPS analyses showed that C-F bonds were formed upon heat treatment and that the amount of C-F bonds increased with the heat treatment temperature. The catalytic effects also increased with the heat treatment temperature, indicating that the catalytic mechanism involved the formation of the C-F bonds on the carbon edge sites.

Metal-doping is indeed helpful to increase the hydrogen storage capacities of adsorbents at ambient conditions. But it was found that the final performance of metal

doped adsorbents varies significantly and was influenced by many factors, e.g., synthesis conditions, post-synthesis treatment, operator experience, etc. The reason behind was not well studied. A series of Pt-doped IRMOF-8 samples with different Pt catalyst sizes have been prepared via organometallic chemical-vapor deposition (CVD). The Pt catalyst size effects on the spillover storage on IRMOF-8 (or any MOF) were studied for the first time. Our studies showed that the Pt catalyst size is a crucial factor determining whether a significant enhancement in storage can be achieved in the hydrogen spillover system at ambient temperature. Compared to undoped IRMOF-8, the spillover storage capacities on Pt-doped IRMOF-8 samples were enhanced by factors ranging from 1.1 – 1.9 due to different Pt catalyst sizes. The doped Pt size was controlled by varying the CVD conditions to yield mean sizes of 2.2, 3.9 and 9.1 nm, and the results showed that smaller sizes were needed for spillover. Further studies of Ru size on the storage uptakes of Na-Y consolidate this conclusion.

In order to utilize adsorbents for hydrogen storage application, they must be stable in this process. Most adsorbents are stable with hydrogen but there are some exceptions. The stabilities of three moisture-stable MOFs containing different metal clusters, i.e. HKUST-1 (Cu), MIL-53(Al) and ZIF-8 (Zn), were investigated in dihydrogen and dissociated hydrogen (caused by doped Pt nanoparticles) environments. X-ray diffraction (XRD), X-ray photoelectron spectroscopy (XPS) and X-ray-excited auger electron spectroscopy (XAES) results showed that all three MOFs were stable in dihydrogen environment. However, the structure of Pt-doped HKUST-1 collapsed in the presence of dissociated hydrogen, due to the higher reduction potential of Cu compared with H, and the degree of reduction that occurred to the divalent copper in HKUST-1 increased with

temperature. Unlike HKUST-1, MIL-53 and ZIF-8 maintained their structures in both dihydrogen and dissociated hydrogen environments at temperatures up to 150°C. Moreover, comparison of Pt-doped HKUST-1 samples synthesized by chemical vapor deposition (CVD) and incipient wetness impregnation showed that the contact between the doped Pt particles and MOFs significantly affected hydrogen spillover.

It's known the first step of hydrogen spillover process is the dissociation of dihydrogen molecules on the surface of some catalysts and previous studies have shown most of the catalysts for hydrogen dissociation are noble-metal catalysts, i.e., Pt, Pd, Ru, Rh.., all of which are very expensive. It will be meaningful and reduce the costs significantly to develop non-noble metal catalysts possessing strong interaction with hydrogen. It was found that zinc exchanged zeolites can facilitate the hydrogen dissociation in the process of propane dehydrogenation and aromatization, but the mechanism of the interaction between hydrogen and zeolites and the factors influencing this interaction was not well studied. This work used H_2-TPD to investigate the interaction between hydrogen and zeolites and found that zinc ions play an important role in this interaction, especially for hydrogen chemisorption on the surface of zeolites. Without zinc ion, the chemisorption did not occur. Higher zinc content leads to more hydrogen chemisorbed and stronger interaction between hydrogen and zeolites. Meanwhile, the framework of zeolite also has an impact on the interaction between hydrogen and zeolites. Moreover, it was also found that higher dosing temperature also lead to more hydrogen chemisorbed on zeolites and stronger interaction between hydrogen and zeolites, which is assumed to be related with the energy barrier for hydrogen chemisorption on zeolites.

Another approach to solve the environmental problems is to control the emission of harmful gases. Desulfurization attracted many interests not only due to environmental regulations but also because of the great need from fuel cell applications. π-complexation adsorption was proposed as an efficient way for fuel desulfurization because it does not require high pressure, high temperature hydrogen and large reactors. In this work, desulfurization of JP-5 jet fuel (1172 ppmw S) was investigated by π-complexation adsorption with $AgNO_3$ supported on mesoporous silica SBA-15 and MCM-41. The average pore sizes of $AgNO_3$/SBA-15 and $AgNO_3$/MCM-41 were 48.8 and 19.1 Å, respectively. The results of JP-5 desulfurization showed that significant sulfur breakthrough occurred at ~10.0 and ~15.0 mL/g by $AgNO_3$/SBA-15 and $AgNO_3$/MCM-41, respectively, at a space velocity of 1.25 h^{-1}. The spent $AgNO_3$/MCM-41 was regenerated by a simple process (heating in air at 200°C) and ~50% of the sulfur capacity was recovered after the first cycle. Molecular orbital calculations show that Cu^+ (as that in CuY zeolite) formed stronger π-complexation bonding with the thiophenic compounds than Ag^+ (in $AgNO_3$), as evidenced by experimental heats of adsorption. However, pore diffusion limitation of the large sulfur molecules (alkylated benzothiophenes) became an important factor for desulfurization of high sulfur jet fuels such that the $AgNO_3$-supported mesoporous sorbents yielded substantially better results than Cu(I)Y, although Cu(I)Y was better for a model fuel that contained only small sulfur molecules. Among all sorbents that have been investigated, the $AgNO_3$/MCM-41 sorbent showed the best desulfurization performance for high sulfur jet fuels.

Chapter 1: Catalytic Effects of TiF_3 on Hydrogen Spillover on Carbon for Hydrogen Storage

Introduction

With increasing concerns about the environmental impact by the overuse of fossil fuels, increasing efforts have been devoted to developing new alternative energy sources (and carriers), among which hydrogen is considered as one of the most promising.[1] However, its utilization requires solutions to a series of problems, mainly hydrogen production, transportation, storage and fuel cell technology.[1] Among these problems, hydrogen storage is particularly challenging because at ambient temperature and pressure the volumetric energy density of hydrogen is only 1/3000 of the energy density of gasoline. There are two straightforward methods to increase the volumetric energy density: to liquefy hydrogen at a very low temperature (~ 20K) or to compress hydrogen at a very high pressure (up to 700 atm).[2] However, the first option needs considerable energy cost for cryogenic storage environment and the latter always raises safety concerns. These disadvantages limit their onboard application.

Compared with these two straightforward methods, using adsorbents for hydrogen storage (along with the use of metal hydrides) is considered a potentially promising approach.[2] There have been many studies to develop materials for this purpose, among which carbon nanotubes, activated carbon, metal-organic frameworks and zeolites have received most attention.[3-22] However, at the present time, none of them are capable of meeting the DOE targets for automobile application. The most important targets are gravimetric/volumetric storage capacities and charge/discharge rates, both at near ambient temperature. During the last six years, a new class of promising sorbent materials has emerged by using the approach of hydrogen spillover at ambient

temperature.[23-50] The hydrogen spillover phenomenon is defined as the process in which H_2 molecules are first dissociatively adsorbed on a metal surface and the atomic hydrogen subsequently migrate onto the support surfaces via surface diffusion.[51] Although the storage capacity of the adsorbents could be enhanced significantly by spillover, the slow rates for spillover remains a major issue for its application.[27]

In the apparently unrelated research fields of metal hydrides for hydrogen storage, there have been many efforts focusing on catalysts that have unique effects on the rates of hydriding and dehydriding. Since the 1960s, several organic compounds have been discovered to have catalytic effects on MgH_2.[52] Doping 1% Pd was also found to have significant catalytic effects on Mg_2Ni and $LaNi_5$.[53] In 1997, it was discovered that the rates in both directions could be increased significantly by doping $TiCl_3$ or $TiCl_4$ on $NaAlH_4$.[54] Subsequently, many other transition metal cations (such as Zr, Fe, Mn, Cr, Co, Nd, etc) have also been found to be effective.[55] More recently, catalytic effects were observed for hydrogen spillover.[51] It was seen that after doping 2 wt% $TiCl_3$ or VCl_3 on Pt-doped carbon, the rates of both adsorption and desorption were increased. However, there was a problem in the lack of stability for these two catalysts: $TiCl_3$ will quickly decompose into TiO_2 and HCl once exposes to air; and VCl_3 undergoes disproportionation during sample preparation when heating is required.[56-59]

In this work, TiF_3 was found to be a very effective catalyst for enhancing the rates in both directions. At the same time, doping TiF_3 only decreased the storage capacity of the adsorbents slightly and did not cause the samples to lose reversibility. Moreover, TiF_3 itself is very stable and the decomposition temperature of TiF_3 is 1473K. Based upon these three reasons, TiF_3 is considered as a promising candidate for enhancement of

adsorption and desorption rates. Moreover, during the doping process of TiF_3, heat treatment at a higher temperature was found to result in more enhanced catalytic effects. The adsorbents before and after treatment were characterized by using XPS, XRD and surface and pore analyses.

Experimental Section

Preparation of Pt/Maxsorb. The superactivated carbon, designated Maxsorb, was prepared by activation of carbon precursors in molten KOH at ~800^{o}C and is available commercially (obtained from Tokyo Zairyo Company). Because Maxsorb carbon could absorb moisture from the ambient air, it was dried first at 393K for several hours. Then 400 mg of well-dried Maxsorb carbon was first dispersed in 40 ml of acetone and was stirred for 0.5 h at room temperature. A 4.0 mL aliquot of acetone solution containing 52 mg H_2PtCl_6 (Aldrich, 99.9%) was slowly added to the above solution under vigorous agitation for about 10 min. Next, the slurry was subjected to ultrasonication (100W, 42kHz) at room temperature for 1h followed by magnetically stirring at room temperature for 24 h. After being dried in an oven at 333K overnight to evaporate most of the acetone solvent, the impregnated carbon sample was transferred to a quartz boat, which was slid into a horizontal quartz tube. The sample was further dried in a helium flow at 393K for 2 h to remove residual acetone and also the moisture adsorbed on the sample. Then the helium flow was switched to H_2 and the temperature increased to 573K at a heating rate of 1 K/min and held for 2 h. After slowly cooling to room temperature in H_2 the sample was purged with flowing helium for at least 2 h and was stored under helium atmosphere before further use.

Pt/Maxsorb doped with TiF_3. An incipient-wetness method was method used to prepare Pt/Maxsorb doped with TiF_3. Typically, 8.0 mg of TiF_3 (Aldrich, 99%) was added to 6 ml of diethyl ether solution and stirred for 1 h.[51] After TiF_3 was dissolved, 400 mg of Pt/Maxsorb sample, which was first degassed at 623K for 5 h, was added to the above solution. After volatilization of the diethyl ether at room temperature, the sample was dried in flowing helium at 323K for 2 h. Before its use, the sample was split into two parts evenly. Then the two parts were degassed and calcined at 473K and 673K for 12 h, respectively.

Characterization. Powder X-ray diffraction (XRD) data was recorded on a Rigaku Miniflex diffractometer at 30 kV, 15 mA with Cu Kα (λ = 0.1543 nm) radiation. X-ray photoelectron spectroscopy (XPS) was recorded on a Kratos Axis ultra XPS spectrometer. BET (Brunauer-Emmet-Teller) surface area and low pressure H_2 adsorption isotherms (0-1 atm) were measured with a standard static volumetric technique by using Micromeritics ASAP 2020. Hydrogen adsorption isotherms at 298K and in the pressure range of 1 – 100 atm were measured using a static volumetric technique with a specially designed Sievert's apparatus. The apparatus was previously tested to prove to be leak-free and proven for accuracy through calibration by using $LaNi_5$ and AX-21 at 298K.[60] Prior to measurements, the samples were degassed at 623K for at least 12 h.[51]

Results and Discussion Section

Characterization of samples. The BET surface areas, pore volumes, and median pore diameters of Maxsorb, Pt/Maxsorb, Pt/Maxsorb with doped TiF_3 and calcined at 473K (Pt/Maxsorb-TiF_3-A) and Pt/Maxsorb with doped TiF_3 and calcined at 673K (Pt/Maxsorb-TiF_3-B) are shown in Table 1.

From Table 1, it can be seen that the BET surface area and pore volume decreased slightly after doping 6wt% Pt onto Maxsorb. The decrease in surface area and pore volume was due to blocking or filling of the micropores and mesopores of Maxsorb by Pt particles. A similar phenomenon happened upon doping a small amount of TiF_3 onto Pt/Maxsorb. It is assumed that part of the doped TiF_3 particles blocked or filled the micropores or mesopores and part of TiF_3 reacted with carbon (as to be discussed).

In order to test this assumption, powder XRD was performed. Powder XRD patterns for pure TiF_3, Pt/Maxsorb, Pt/Maxsorb-TiF_3-A and Pt/Maxsorb-TiF_3-B samples are shown in Figure 1.

In Figure 1, TiF_3 shows diffraction peaks at $2\theta=23.1°$, $2\theta=32.7°$, $2\theta=38.7°$, $2\theta=47.2°$, $2\theta=52.9°$ and $2\theta=59.1°$. Among these peaks, the strongest one appears at $2\theta=23.1°$. Pt doped Maxsorb only showed two peaks that are characteristic of cubic platinum metal structure (JCPDS File Card No. 4-802). They are: $2\theta=39.8°$ (111) and $2\theta=46.3°$ (200). With TiF_3 doped on Pt/Maxsorb, only the strongest peak for TiF_3 at $2\theta=23.1°$ appeared because the amount of TiF_3 was too small, only 2 wt%. Moreover, when Pt/Maxsorb doped with TiF_3 and calcined at the higher temperature (673K), the peak at $2\theta=23.1°$ diminished. This indicated that part of the TiF_3 had reacted with carbon during heating at 673K, because the decomposition temperature of TiF_3 is 1473K.

In order to verify whether TiF_3 reacted with Pt/Maxsorb during heating, the detailed scan (core scan) of the X-ray Photoelectron spectroscopy was conducted around the peak of fluorine which is about 685 eV. The X-ray Photoelectron spectra of Pt/Maxsorb-TiF_3-A and Pt/Maxsorb-TiF_3-B are shown in Figure 2.

As shown in Figure 2, fluorine (F) has two split peaks. The peak at 685.8 eV is assigned to F^- which belongs to TiF_3; and the peak at 689.1 eV is assigned to the C-F bond.[61-63] The XPS result is direct evidence that part of the TiF_3 has reacted with carbon during the process of heat-treatment. Moreover, the relative peak height for C-F Bond/TiF_3 increased from 0.25 (heat-treated at 473K) to 0.30 (heat-treated at 673K). That is, more C-F bonds were formed when the heat-treatment temperature was higher.

Hydrogen isotherms at 298K. The low pressure hydrogen isotherms on Pt/Maxsorb, Pt/Maxsorb-TiF_3-A and Pt/Maxsorb-TiF_3-B at 298K were measured by using Micromeritics ASAP 2020, presented in Figure 3. As shown in Figure 3, the hydrogen storage capacity of Pt/Maxsorb decreased slightly after doping with TiF_3 and was further lowered upon heating at a higher temperature (673K). This result can be attributed to the differences in the BET surface areas of these samples.

High-pressure hydrogen isotherms at 298K for Pt/Maxsorb, Pt/Maxsorb-TiF_3-A and Pt/Maxsorb-TiF_3-B were measured by using the Sievert's apparatus, which was mentioned above in the experimental section.[60] The isotherms including both adsorption and desorption branches for Pt/Maxsorb, Pt/Maxsorb-TiF_3-A and Pt/Maxsorb-TiF_3-B are shown in Figures 4, 5 and 6. These isotherms are also compared directly on Figure 7.

As shown in Figure 7, the hydrogen storage capacity of Pt/Maxsorb at 298K under 100 bar was 1.30 wt% which was much higher than pure Maxsorb (0.7wt%); after doping with 2 wt% TiF_3 and calcined at 473K, the capacity decreased slightly to 1.24 wt%. and decreased to 1.19 wt% after being heated at 673K. The decreased capacity was again attributed to decreases in the BET surface area due to doping and heat treatment.

Reversibility was tested by measuring the desorption branches of the isotherms. Although slight hystereses were seen, all adsorbed hydrogen could be desorbed at 298K by degassing. These results showed that the adsorption on Pt/Maxsorb did not lose reversibility after doping with TiF_3 and heating at 473K and 673K.

Adsorption and Desorption Rates at 298K. The adsorption or desorption rates at 298K were measured by following the adsorbed amount vs. time, and this was performed by increasing or decreasing the pressure in steps. For example, the first step was taken by increasing pressure from 0 to 28.6 atm. The high-pressure rates were also measured by using the specially designed Sievert's apparatus mentioned above. For the similar pressure increase step, the uptake rates for Pt/Maxsorb, Pt/Maxsorb-TiF_3-A and Pt/Maxsorb-TiF_3-B are shown in Figure 8. The desorption rates during a comparable pressure decrease step are shown in Figure 9.

From Figures 8 and 9, it is concluded that both the adsorption and desorption rates were increased significantly by doping TiF_3, and that heat-treatment at higher temperature was more effective. Moreover, the desorption rates were higher than the adsorption rates as observed in previous work.[27]

For spillover on carbon and similar materials near room temperature, surface diffusion has been considered as the rate limiting step.[28-29, 64-65] The hydrogen atom has been identified as the diffusing species.[29, 65-67] Thus, the rates could be expressed quantitatively in terms of surface diffusion time constant by estimation from a solution to the surface diffusion equation. The surface diffusion time constant is D/R^2, where D is the surface diffusivity and R is the average characteristic radius of diffusion for spillover.[27, 51] From the data in Figure 5 and 6, the estimates for D/R^2 could be made, and

the results are shown in Table 2. As shown in Table 2, by doping Pt/Maxsorb with TiF3 and heat-treatment at 473K, D/R^2 for both adsorption and desorption rates increased by more than 50%; after doping with TiF_3 and heat-treatment at 673K, D/R^2 of both directions nearly doubled.

In order to understand the mechanism for the catalytic effects of TiF_3 on hydrogen spillover, the samples were studied by XPS analyses. As shown above, C-F bonds were observed on the samples that were doped with TiF_3. As importantly, the amount of C-F bonds increased with the heat treatment temperature that followed the TiF_3 doping. Therefore, the catalytic effects seemed to be related to the formation of the C-F bonds on the edges of the carbon. A tempting explanation for the mechanism would involve the decoration/bonding of the carbon (graphite) edge sites with TiF_3 in some fashion, and consequently the formation of feeder "highway" paths along the edge sites for the migrating H atoms. Such a mechanism would require that the bond between H and the carbon edge sites be weakened when the edge carbon sites are also bonded to TiF_3 in some configuration. However, preliminary molecular orbital calculations showed that the bonding strength between H and the edge sites of carbon was only to increase by simply attaching F atoms to the edge carbon sites. Further studies of the mechanism are warranted.

Conclusions

TiF_3 has been found to be an effective catalyst for hydrogen spillover on Pt doped Maxsorb at 298K. Upon TiF_3 doping, the BET surface area and pore volume of the Pt/Maxsorb decreased slightly, and consequently the hydrogen uptake amount also decreased slightly. However, the hydrogen adsorption and desorption rates on

Pt/Maxsorb after doping TiF_3 were 1.5 times that without TiF_3. Moreover, heat treatment of the doped TiF_3 at a higher temperature (675K vs. 475K) was found to be more effective, which could double both the hydrogen adsorption and desorption rates on Pt doped Maxsorb carbon. XPS analyses showed that C-F bonds were formed upon heat treatment and that the amount of C-F bonds increased with the heat treatment temperature. The catalytic effects also increased with the heat treatment temperature. Thus, the catalytic mechanism seems to involve the formation of the C-F bonds on the carbon edge sites.

Acknowledgement

The authors acknowledge the funding provided by the U.S. Department of Energy's Office of Energy Efficiency and Renewable Energy within Hydrogen Sorption Center of Excellence (HS CoE) as well as the funding from NSF.

Note

The contents of this chapter have been published in Langmuir 2010, 26, 15394.

References:

1. Schlapbach, L.; Züttel, A. *Nature* **2001**, *414*. 353.
2. Li, Y.W.; Yang, R.T. *J. Phys. Chem. B* **2006**, *110*, 17175.
3. Dillon, A. C.; Jones, K. M.; Bekkedahl, T. A.; Kiang, C. H.; Bethune, D. S.; Heben, M. J. *Nature* **1997,** *386*, 377.
4. Dillon, A. C.; Heben, M. *J. Appl. Phys. A: Mater. Sci. Process.* **2001**, *72*, 133.
5. Züttel, A. *Mater. Today* **2003**, *6*, 24.
6. Anson, H.; Benham, M.; Jagiello, J.; Callejas, M.A.; Benito, A.M.; Maser, W.K.; Zuttel, A.; Sudan, P.; Martinez, M.T. *Nanotechnology* **2005**, *15*, 1503.
7. Xu, W.C.; Takahashia, K.; Matsuoa, Y.; Haattoria, Y.; Kumgaia, M.; Ishiyamab, S.; Kanekoc, K.; Iijima, S. *Int. J. Hydrogen Energy* **2007**, *32*, 2504.
8. Choi, M.; Ryoo, R. *J. Mater. Chem.* **2007**, *17*, 4204.
9. Kyotani, T.; Nagi, T.; Inoue, S.; Tomita, A. *Chem. Mater.* **1997**, *9*, 609.
10. Yang, Z.; Xia, Y.; Mokaya, R. *J. Am. Chem. Soc.* **2007**, *129*, 1673.
11. Ryoo. R.; Joo, S.H.; Sun, S. *J. Phys. Chem. B.* **1999**, *103*, 7743.
12. Stphanie-Victorie, F.; Goulay, A.M.; de Lara, E.C. *Langmuir* **1998**, *14*, 7255.
13. Langmi, H.W.; Book.D.; Walton, A.; Johnson, S.R.; Al-Mamouri, M.M.; Speight, J.D.; Edwards, P.P.; Harris, I.R.; Anderson, P.A. *J. Alloys. Compd.* **2005**, *404-406*, 637.
14. Kazansky, V.B.; Borokov, V.Y.; Serich, A.; Karge, H.G. *Micropor. Mesopor. Mater.* **1998**, *22*, 251.
15. Zecchina, A.; Bordiga, S.; Vitillo, J.G.; Ricchiardi, G.; Lamberti, C.; Spoto, G.; Bjrgen, M.; Lillerud, K.P. *J. Am. Chem. Soc.* **2005**, *127*, 6361.
16. Rosi, N.L.; Eckert, J.; Eddaoudi, M.; Vodak, D.T.; Kim, J.; O'Keefee, M.; Yaghi, O.M. *Science* **2003**, *300*, 1127.
17. Chae, H.; Siberio-Perez, D.Y.; Kim, J.; Go, Y.; Eddaoudi, M.; Matzger, A.; O'Keefee, M.; Yaghi, O.M. *Nature* **2004**, *427*, 523.
18. Murray, L.J.; Dinca, M.; Long, J.R. *Chem. Soc. Rev.* **2009**, *38*, 1294.
19. Kaye, S.S.; Dailly, A.; Yaghi, O.M.; Long, J.R. *J. Am. Chem. Soc.* **2007**, *129*, 14176.
20. Kaye, S.S.; Long, J.R. *J. Am. Chem. Soc.***2005**, *127*, 6506.
21. Dinca, M.; Dailly, A.; Liu, Y.; Brown, C.M.; Neumann, D.A.; Long, J.R. *J. Am. Chem. Soc.***2006**, *128*, 16876.
22. Ma, S.; Zhou, H.C. *J. Am. Chem. Soc*. **2006**, *128*, 11734.
23. Lueking, A.; Yang, R. T. *J. Catal.* **2002**, *206*, 165.
24. Lachawiec, A. J.; Qi, G.; Yang, R. T. *Langmuir* **2005**, *21*, 11418.
25. Li, Y. W.; Yang, R. T. *J. Am. Chem. Soc.* **2006**, *128*, 726.
26. Li, Y. W.; Yang, R. T. *J. Am. Chem. Soc.* **2006**, *128*, 8136.
27. Li, Y. W.; Yang, R. T. *J. Phys. Chem. C* **2007**, *111*, 3405.
28. Wang, L.; Yang, R. T. *J. Phys. Chem. C* **2008**, *112*, 12486.
29. Lachawiec, A. J., Jr.; Yang, R. T. *Langmuir* **2008**, *24*, 6159.
30. Anson, A.; Lafuente, E.; Urriolabeitia, E.; Navarro, R.; Benito, A.M.; Maser, W.K.; Martinez, M.T. *J. Phys. Chem. B* **2006**, *110*, 6643.
31. Zacharia, R.; Rather, S.U.; Hwang, S.W.; Nahm, K.S. *Chem. Phys. Lett.* **2007**, *434*, 286.

32. Rather, S.U.; Naik, M.U.D.; Zacharia, R.; Hwang, S.W.; Kim, A.R.; Nahm, K.S.; *Inter. J. Hydrogen Energy* **2009**, *34*, 961.
33. Yoo, E.; Gao, L.; Komatsu, T.; Yagai, N.; Arai, K.; Yamazaki, T.; Matsuishi, K.; Matsumoto, T.; Nakamura, J. *J. Phys. Chem. B* **2004**, *108*, 18903.
34. Kim, S.Y.; Lee, J.W.; Jung, J.H.; Kang, J.K. *Chem. Mater.* **2007**, *19*, 135.
35. Reddy, A.L.M.; Ramaprabhu, S. *Inter. J. Hydrogen Energy* **2008**, *33*, 1028.
36. Miller, M.A.; Wang, C.Y.; Merrill, G.N. *J. Phys. Chem. C* **2009**, *113*, 3222.
37. Tsao, C.S.; Yu, M.S.; Wang, C.Y.; Liao, P.Y.; Chen, H.L.; Jeng, US.; Tzeng, Y.R.; Chung, T.Y.; Wu, H.C. *J. Am. Chem. Soc.* **2009**, *131*, 1404.
38. Kim, B.J.; Lee, Y.S.; Park, S.J. *Inter. J. Hydrogen Energy* **2008**, *33*, 4112.
39. Lupu, D.; Biris, A.R.; Misan, I.; Jianu, A.; Holzhuter, G.; Burkel, E. *Int. J. Hydrogen Energy* **2004**, *29*, 97.
40. Lee, Y.S.; Kim, Y.H.; Hong, J.S.; Suh, J.K.; Cho, G.J. *Catal. Today* **2007**, *120*, 420.
41. Back, C.; Sandi, G.; Prakash, J.; Hranisavljevic, J.; *J. Phys. Chem. B* **2006**, *110*, 16225.
42. Nishihara, H.; Hou, P.X.; Li, L.X.; Ito, M.; Uchiyama, M.; Kaburagi, T.; Ikura, A.; Katamura, J.; Kawarada, T.; Mizuuchi, K.; Kyotani, T. *J. Phys. Chem. C* **2009**, *113*, 3189.
43. Zielinski, M.; Wojcieszak, R.; Monteverdi, S.; Mercy, M.; Bettahar, M.M. *Int. J. Hydrogen Energy* **2007**, *32*, 1024.
44. Campesi, R.; Cuevas, F.; Leroy, E.; Hirscher, M.; Gadiou, R.; Vix-Guterl, C.; Latroche, M. *Micropor. Mesopor. Mater.* **2009**, *117*, 511.
45. Zubizarreta, L.; Mene´ndez, J.A.; Pis, J.J.; Arenillas, A. *Int. J. Hydrogen Energy* **2009**, *34*, 3070.
46. Mu, S.; Tang, H.; Qian, S.; Pan, M.; Yuan, R. *Carbon* **2006**, *44*, 762.
47. Liu, Y.Y.; Zeng, J.L.; Zhang, J.; Xu, F.; Sun, L.X. *Int. J. Hydrogen Energy* **2007**, *32*, 4005.
48. Saha, D.; Deng, S.G. *Langmuir* **2009**, *25*, 12550.
49. Proch, S.; Herrmannsdörfer, J.; Kempe, R.; Kern, C.; Jess, A.; Seyfarth, L.; Senker, J. *Chem.-A Euro. J.* **2008**, *14*, 8204.
50. Cheon, Y.E.; Suh, M.P. *Angew. Chem. Int.Ed.* **2009**,*48*, 2899.
51. Yang, R.T.; Wang, Y.H. *J. Am. Chem. Soc.* **2009**, *131*, 4224.
52. Zaluska, A.; Zaluski, L.; Strom-Olsen, J. O. *J. Alloys Compd.* **1999**, *288*,217.
53. Zaluski, L.; Zaluska, A.; Tessier, P.; Strom-Olsen, J. O.; Schulz,R. *J. Alloys Compd.* **1995**, *217*, 295.
54. Bogdanovic, B.; Schwickardi, M. *J. Alloys Compd.* **1997**, *253-254*, 1.
55. Anton, D. L. *J. Alloys Compd.* **2003**, *356*, 400.
56. Cassaignon, S.; Koelsch, M.; Jolivet, J.P. *J. Phys. Chem. Solids* **2007**, *68*, 695.
57. Kavan, L.; O'Regan, B.; Kay, A.; Grätzel, M. *J. Electroanal. Chem.* **1993**, *346*, 291.
58. Campbell, T.T.; Schaller, J.L.; Block, F.E. *Metallurgical Transactions*. **1973**, *4*, 237.
59. Gupta, C.K. *Chemical metallurgy: principles and practice*, Wiley-VCH, Weinheim, **2002**.
60. Lachawiec, A. J.; DiRaimondo, T. R.; Yang, R. T. *Rev. Sci. Instrum.* **2008**,

79,063906.
61. Carlo, S.R.; Perry, C.C.; Torres, J.; Wagner, A.J.; Vecitis, C.; Fairbrother, H.D. *Appl. Surface Sci.***2002**, *195*, 93.
62. Ramanath, G.; Greene, J.E.; Carlsson, J.R.A.; Allen, L.H.; Hornback, V.C.; Allman, D.J. *J. Appl. Phys.***1999**, *85*, 3.
63. Ma,L.P.; Kang, X.D.; Dai, H.B.; Liang, Y,; Fang, Z.Z.; Wang, P.J.; Wang, P.; Cheng, H.M. *Acta Mater*. **2009**, *57*, 2250.
64. Robell, A. J.; Ballou, E. V.; Boudart, M. *J. Phys. Chem.* **1964**, *68*, 2748.
65. Conner, W. C.; Falconer, J. L. *Chem. Rev.* **1995**, *95*, 759
66. Mitchell, P. C. H.; Ramirez-Cuesta, A. J.; Parker, S. F.; Tomkinson, J.; Thompsett, D. *J. Phys. Chem. B* **2003**, *107*, 6838.
67. Mitchell, P. C. H.; Ramirez-Cuesta, A. J.; Parker, S. F.; Tomkinson, J. *J. Mol. Struct.* **2003**, *651-653*, 781.

Sample	BET SA (m^2/g)	Pore volume (cm^3/g) [a]	Median pore diameter (Å) [a]
Maxsorb	3277	1.60	17.6
Pt/Maxsorb	2882	1.50	14.7
Pt/Maxsorb-TiF_3-A	2825	1.47	14.7
Pt/Maxsorb-TiF_3-B	2801	1.47	14.6

[a] From H-K analysis

TABLE 1: Surface areas, pore volumes and pore diameters of samples

Sample	Adsorption		Desorption	
	Pressure step (atm)	D/R^2 (10^{-4} s^{-1})	Pressure step (atm)	D/R^2 (10^{-4} s^{-1})
Pt/Maxsorb	0-28.6	1.1	77.7-52.8	2.7
Pt/Maxsorb-TiF_3-A	0-28.7	1.7	78.1-53.1	4.1
Pt/Maxsorb-TiF_3-B	0-28.7	2.1	77.9-52.9	5.2

TABLE 2. Estimates for surface diffusion time constant, D/R^2, for spillover on Pt/Maxsorb, Pt/Maxsorb-TiF_3-A and Pt/Maxsorb-TiF_3-B at 298K.

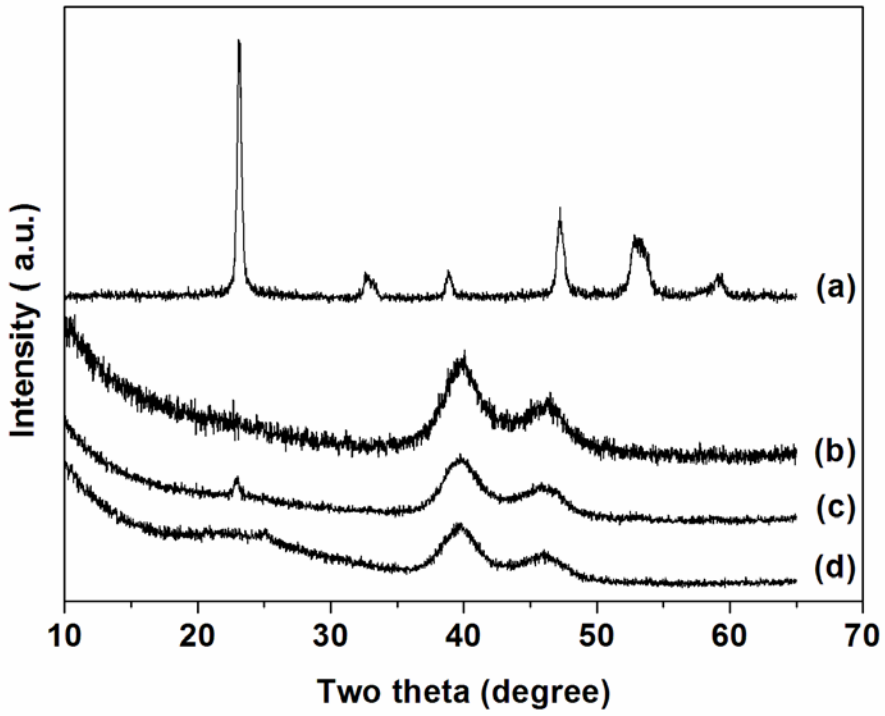

Figure 1. Powder X-ray diffraction patterns. (a): pure TiF_3; (b): Pt/Maxsorb; (c): Pt/Maxsorb-TiF_3-A; (d): Pt/Maxsorb-TiF_3-B.

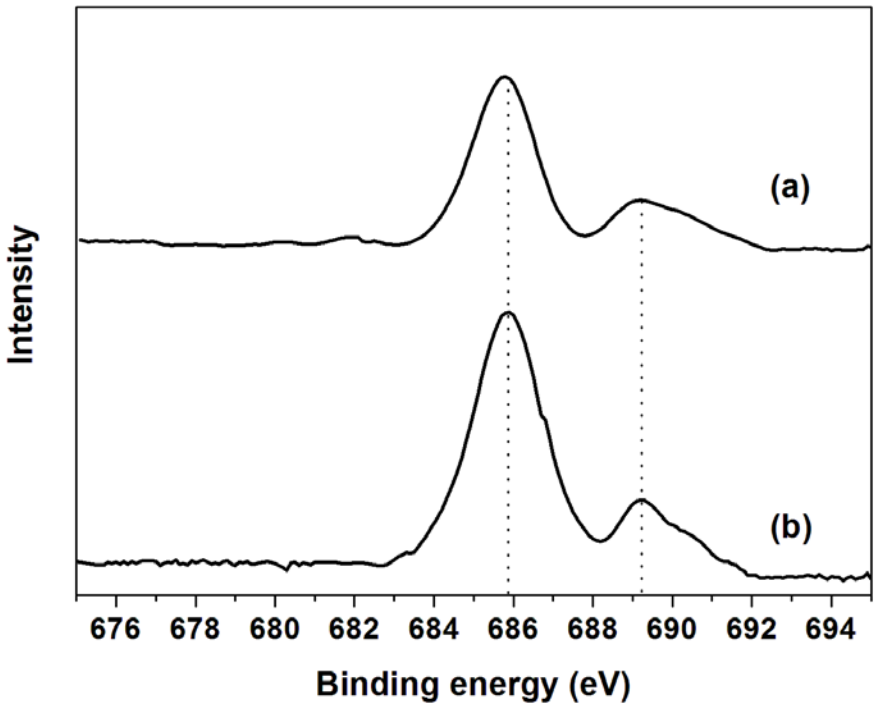

Figure 2. X-ray Photoelectron core scan spectra of F for samples (a): Pt/Maxsorb-TiF_3-A (heat-treated at 473K), and (b): Pt/Maxsorb-TiF_3-B (heat-treated at 673K).

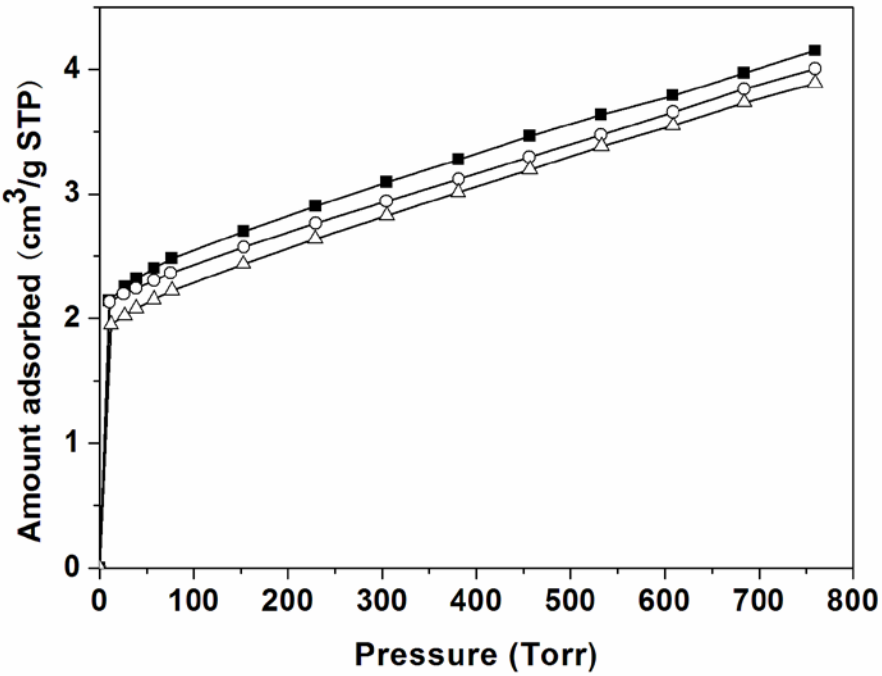

Figure 3. Low-pressure isotherms of H_2 on samples (■: Pt/Maxsorb; ○: Pt/Maxsorb-TiF_3-A; △: Pt/Maxsorb-TiF_3-B).

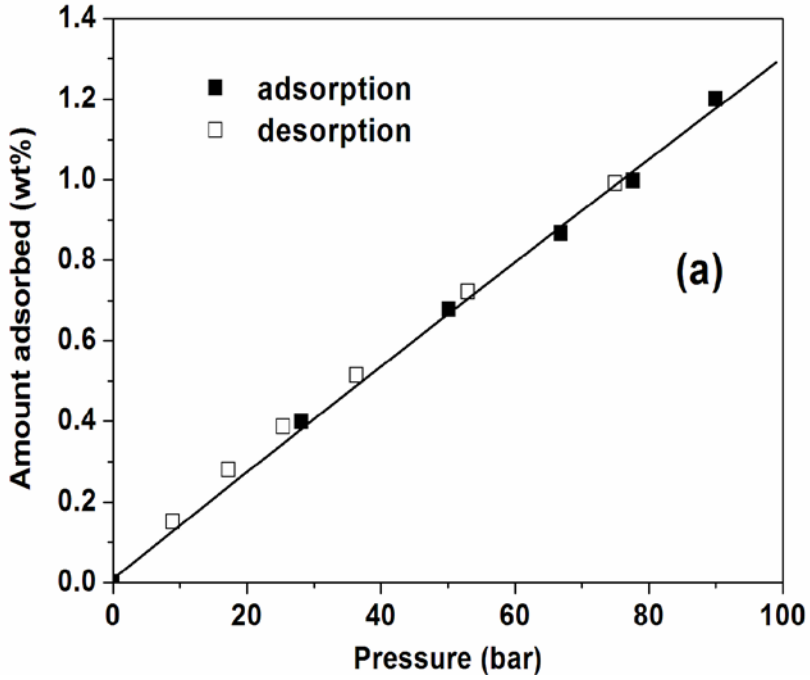

Figure 4. High pressure hydrogen isotherm for Pt/Maxsorb. ■: adsorption; □: desorption

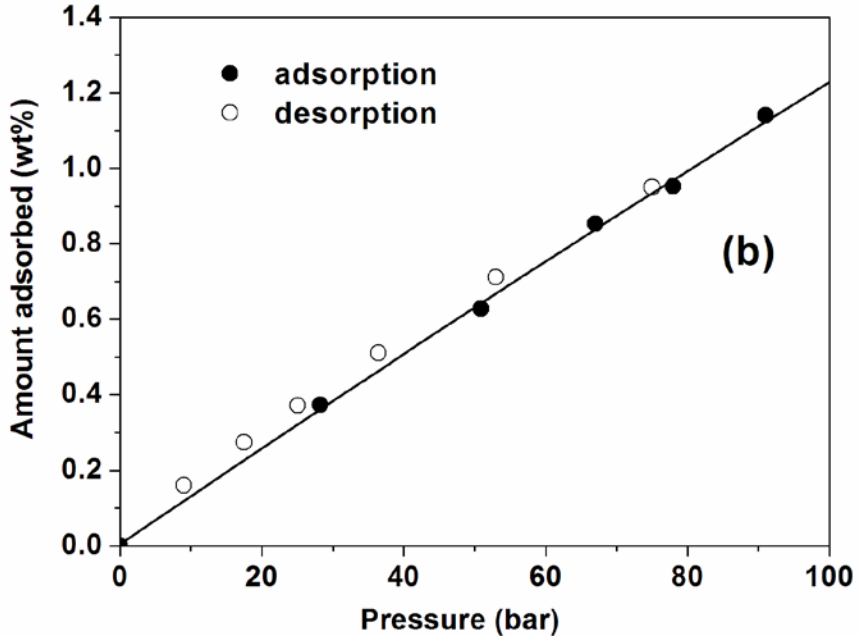

Figure 5. High pressure Hydrogen isotherm for Pt/Maxsorb-TiF_3-A. ●: adsorption; ○:desorption

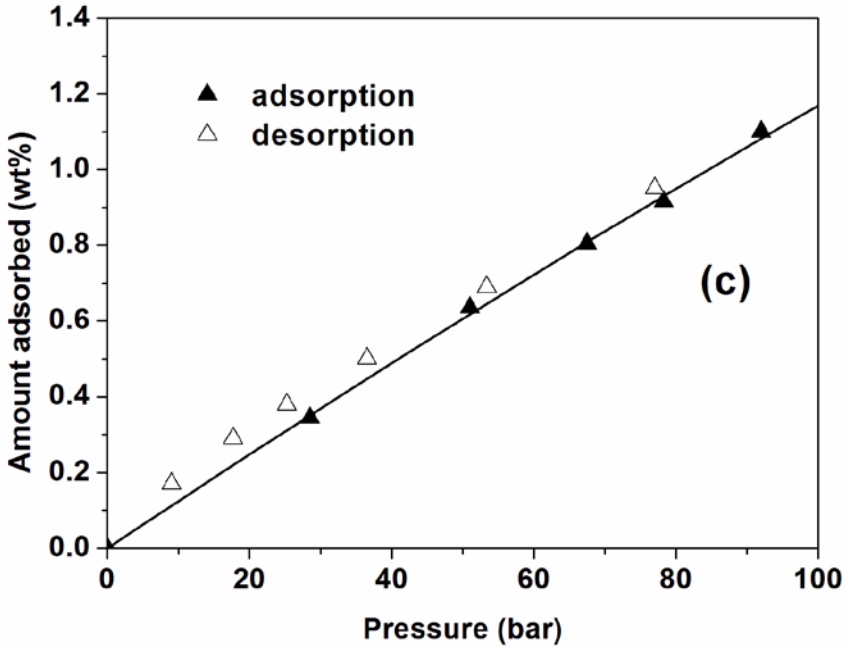

Figure 6. High pressure Hydrogen isotherm for Pt/Maxsorb-TiF_3-B. ▲: adsorption; △: desorption.

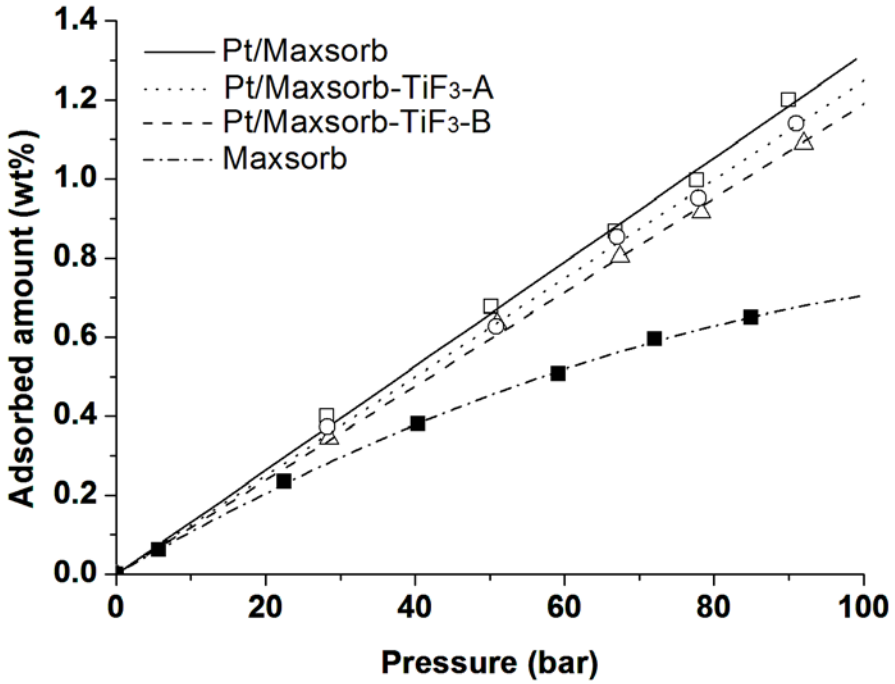

Figure 7. Comparison of hydrogen adsorption isotherms□: Pt/Maxsorb; ○: Pt/Maxsorb-TiF_3-A; △: Pt/Maxsorb-TiF_3-B; ■: Maxsorb.

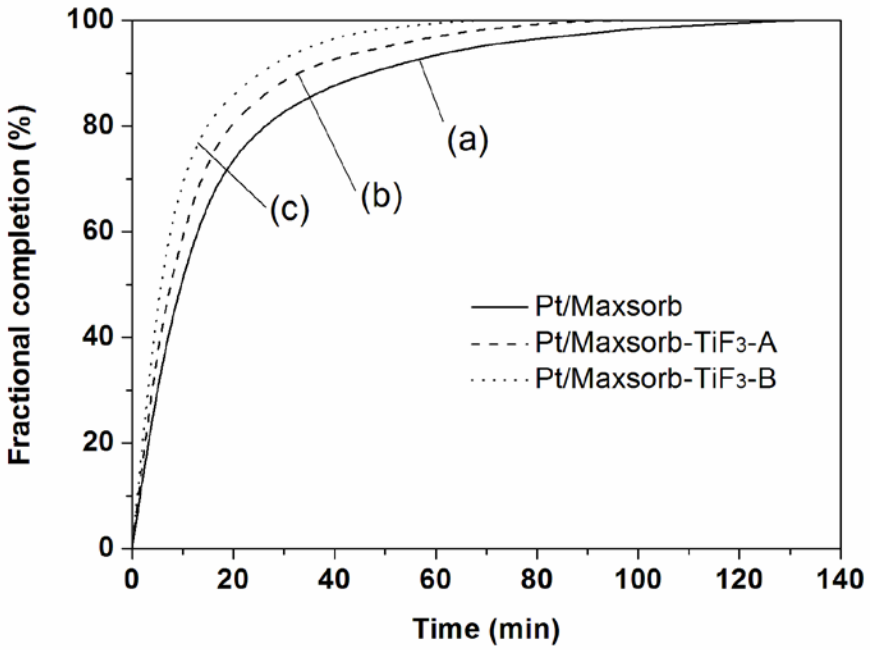

Figure 8. Hydrogen uptake rates on Pt/Maxsorb, Pt/Maxsorb-TiF_3-A and Pt/Maxsorb-TiF_3-B at 298K. Pressure step: (a) 0-28.6 atm for Pt/Maxsorb; (b): 0-28.7 atm for Pt/Maxsorb-TiF_3-A; (c) 0-28.7 atm for Pt/Maxsorb-TiF_3-B.

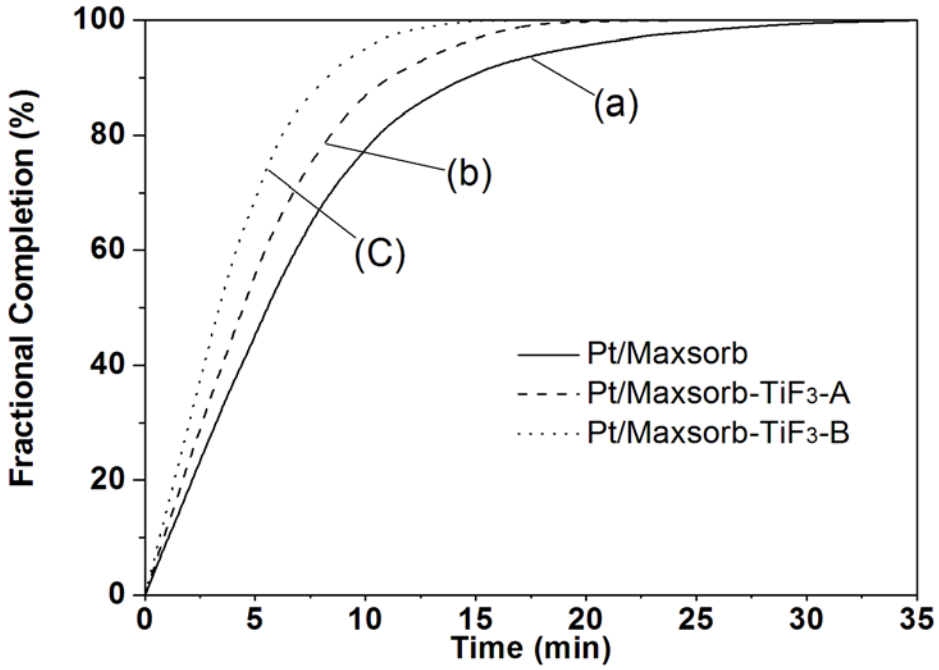

Figure 9. Hydrogen desorption rates on Pt/Maxsorb, Pt/Maxsorb-TiF_3-A and Pt/Maxsorb-TiF_3-B at 298K. Pressure step: (a) 77.7-52.8 atm for Pt/Maxsorb; (b): 78.1-53.1 atm for Pt/Maxsorb-TiF_3-A; (c) 77.9-52.9 atm for Pt/Maxsorb-TiF_3-B.

Chapter 2: Effects of Pt Particle Size on Hydrogen Storage on Pt-Doped Metal-Organic Framework IRMOF-8

Introduction

Hydrogen storage is one of the key issues for the realization of fuel-cell powered vehicles using hydrogen as the energy carrier.[1] Among candidate hydrogen storage adsorbents, metal-organic frameworks (MOFs), a class of porous materials constructed by coordinate bonds between multidentate ligands and metal atoms or small metal-containing clusters, have attracted increasing attention due to their lightweight, high surface area and porosity, and adjustable structures.[2-7] Significant storages at 77K on MOFs with high surface areas have been reported. For example, MOF-177 with a Langmuir surface area of 5640 m^2/g could store the highest 7.5 wt % H_2 at 77 K and 7 MPa.[8,9] The storage capacities of fully activated MIL-101 (Langmuir surface area 5900 m^2/g) at 77 K were 3.75 wt % at 2 MPa and 6.1 wt % at 8 MPa.[10,11] However, these significant storage capacities were achieved only at 77 K. At near ambient temperatures, the storage capacities dropped precipitously. This can be understood because hydrogen adsorption on MOFs is mostly due to weak van der Waals interactions.

To improve the hydrogen storage on adsorbents at room temperature, a most effective approach is by using hydrogen dissociation on an added catalyst followed by spillover. Up to date, more than 100 papers published by ~ 40 groups worldwide have reported significant enhancements in hydrogen storage by spillover at ambient temperatures demonstrating this technique (summarized in ref. 12). Hydrogen spillover can be defined as the dissociative chemisorption of hydrogen on metal nanoparticles, and subsequent migration of hydrogen atoms onto adjacent surfaces of a receptor via surface diffusion.[13-18] Evidence of atomic hydrogen spillover was first observed in studies of ethylene hydrogenation[19] and later observed in the reduction of transition metal oxides with Pt catalyst and hydrogen uptake on transition metals supported on carbon by

Khoobiar and Boudart.[13,20,21] Direct evidence of spillover of atomic hydrogen, *at room temperature,* from Pt to carbon,[22-24] from Pt to glass[25] and from Au to TiO_2[26] has been reported recently. The most important direct evidence for hydrogen spillover at room temperature was obtained by Mitchell et al.[22,23] in their study of commercial Pt/C, Ru/C and PtRu/C fuel cell catalysts dosed with hydrogen, by using inelastic neutron scattering (INS). Their work showed a large continuum in the INS vibration spectra (at >1000 cm^{-1}) that was directly attributed to a layer of mobile H atoms on the carbon support, with a weak binding energy of 15 kJ/mol. Evidence of spillover effects on Pt-doped activated carbon by using INS was also reported by Tsao et al.[24] Meantime, theoretical studies have illustrated the facile pathway for spillover from a Pt particle onto a graphene basal plane is via physisorption of H atoms[22,27,28] and thermodynamically spillover can occur from both the free-standing metal clusters and from the receptor-supported metal clusters.[29,30] DFT studies also showed the facilitated hydrogen spillover on oxygen modified carbons and enhanced interactions between hydrogen atom and boron modified carbons.[31,32] The spillover storage capacities for different MOFs and COF-1 have been calculated by Ganz and coworkers.[33] Among all transition and noble metals, the most difficult one for doping on carbon with high dispersion is Pt; recent results have shown that high dispersion (i. e., in particle sizes less than ~4 nm) is necessary for hydrogen spillover to occur (e.g., Refs. 34-37). Missteps in catalyst preparation and activation (prior to storage measurement) lead directly to diminished or no spillover. Common missteps and pitfalls have been pointed out recently.[34]

Hydrogen spillover on MOFs can be facilitated by building carbon bridges between the dissociation source (e.g., commercial Pt/AC catalyst) and MOFs,[38-43] encapsulation[44]

or direct doping of dissociation metals (Pt, Pd, Ni) on MOFs.[45-48] The thermal-desorption mass spectrometry studies by Miller group have revealed multiple hydrogen binding sites occurring on catalyst bridged-MOFs between 263 and 298 K, substantially higher than that for simple physisorbed dihydrogen.[41] The factors that affect hydrogen spillover on MOFs by bridge building have been discussed.[34] It was suggested that the ideal situation for hydrogen spillover on bridged-MOFs was when all individual catalyst and MOF receptor particles were "bridged," which was highly empirical and difficult to achieve. Studies on direct doping of metals on MOFs for hydrogen spillover started to appear recently. Enhanced hydrogen spillover at room temperature has been observed on Pt-doped MOF-177, Ni-doped MIL-101, Pd-doped redox-active MOF, and Pd-doped MIL-100.[45-48] Unlike the MOF-bridging technique, direct metal doping has the potential of being more controllable and hence the results more reproducible. It is known that direct doping could result in the dispersion of metal particles on MOFs, and physical and energy barriers for transfer of hydrogen atoms from one material to another exist during spillover. Thus the dispersion and the particle size of the metal on MOFs will affect spillover and thereby the hydrogen storage on MOFs. To our knowledge, studies of catalyst dispersion and particle size effects on hydrogen storage on MOFs have not been reported. In this work, we synthesized a series of direct Pt-doped IRMOF-8 samples via organometallic chemical vapor deposition and studied the Pt dispersion and particle size effects on the hydrogen storage.

Experimental Section

Syntheses. (1) Synthesis of IRMOF-8: Typically, 1.19 g of $Zn(NO_3)_2 \cdot 6H_2O$ (freshly opened) and 0.43 g of 2,6-naphtalenedicarboxylic acid were dissolved in 40 mL of

diethylformamide (DEF) during vigorous stirring at room temperature.[49,50] The DEF solution was heated to 393 K for 20 hrs and then cooled to room temperature. The white product was collected by filtering and four thorough washings with DMF. The product was exchanged by $CHCl_3$ 4 times, and then degassed at 423 K for 12 hrs.

(2) Synthesis of Pt-doped IRMOF-8 via chemical vapor deposition (CVD): Pt was doped on IRMOF-8 by chemical vapor deposition of a volatile platinum precursor (Trimethyl)methylcyclopentadienyl platinum (IV). The MOF crystals were ground before CVD. The grounded MOFs (0.6 g) and the organometallic precursor (0.09 g) were placed in a tube separated by a glass frit and degassed to a vacuum of < 10 μmHg at 273 K. After that, the degassing was stopped and the temperature was increased to 303 K and kept at 303 K for 1 hr. The vacuum of this system was renewed each hour for 6 cycles then stayed for another 6 hrs. During this procedure, an off-white composite was yielded and designated as Pt/IRMOF-8-1. For Pt/IRMOF-8-2 sample, the temperature was kept at 308 K and the vacuum was renewed each hour for 4 cycles then stayed for another 8 hrs. For Pt/IRMOF-8-3 sample, the temperature was kept at 318 K and the vacuum was renewed for 1 cycle then stayed 11 hrs. These three samples were reduced in a hydrogen atmosphere at 423 K overnight, and then purged with flowing helium. Finally, the Pt/IRMOF-8-1 with 4.8 wt % Pt, Pt/IRMOF-8-2 with 6.2 wt % Pt, and Pt/IRMOF-8-3 with 7.7 wt % Pt were obtained.

Sample Characterization and Isotherm Measurements. Powder X-ray diffraction (XRD) data were recorded on a Rigaku Miniflex diffractometer at 30 kV, 15 mA for Cu Kα (λ = 0.1543 nm) radiation, with a step size of 0.02° in 2θ. Transmission electron microscopy (TEM) images were obtained on a JEOL 3011 analytical electron microscope

equipped with EDX analysis operated at 300 kV. Nitrogen adsorption and low-pressure H_2 adsorption isotherms (0-1 atm) were measured with a standard static volumetric technique (Micromeritics ASAP 2020). Hydrogen adsorption at 298 K and pressures greater than 0.1 MPa and up to 10 MPa was measured using a static volumetric technique with a specially designed Sieverts-type apparatus. The apparatus was previously tested and proven to be leak-free and accurate through calibration by using $LaNi_5$, AX-21, Maxsorb, zeolites, and MOFs at 298 K.[51] The best standard calibration material for high pressure hydrogen storage measurement is the commercial super-activated carbon, AX-21 or Maxsorb. The storage capacity for AX-21 (BET S.A. = 2800 m^2/g) at 10 MPa and 298 K should be 0.6 wt % while that for Maxsorb (BET S.A. = 3300 m^2/g) should be 0.7 wt % under the same conditions, both with a slightly concave-shaped isotherm. Approximately 200 mg of sample was used for each high-pressure isotherm measurement in this study.

Results and Discussion

Powder X-ray diffraction patterns of IRMOF-8 and Pt/IRMOF-8 samples are shown in Figure 10. The plain IRMOF-8 (Fig. 10 D) showed typical peaks at $2\theta = 6.3°$, in good agreement with previous reports.[49,50] After doping with Pt, the XRD patterns of Pt/IRMOF-8-1, Pt/IRMOF-8-2 and Pt/IRMOF-8-3 samples all exhibited the same peaks as those of plain IRMOF-8 although the peak intensity decreased slightly. This indicates that the microstructure of IRMOF-8 was retained after the doping treatments. Furthermore, the Pt/IRMOF-8 samples all showed two peaks at ca. 40° and 46° characteristic of the metallic platinum particles. These results confirm that Pt metals were successfully doped on IRMOF-8 by applying the CVD method. It is noted that the peaks

corresponding to Pt became narrower from Pt/IRMOF-8-1 to Pt/IRMOF-8-2 and Pt/IRMOF-8-3. This indicates that the Pt particle size increased in the order of Pt/IRMOF-8-1 < Pt/IRMOF-8-2 < Pt/IRMOF-8-3.

Nitrogen adsorption was further employed to evaluate the porosity of plain IRMOF-8 and the doped samples. As shown in Figure 11, the isotherms of IRMOF-8 and Pt/IRMOF-8 samples all exhibited the type I curve, thus revealing the presence of microporosity in the samples. The BET surface area and pore volume of the plain IRMOF-8 are 1430 m^2/g and 0.69 cm^3/g, respectively. These textural properties are in agreement with previous report.[49,50] After doping Pt on IRMOF-8, the BET surface areas and pore volumes of Pt/IRMOF-8-1, Pt/IRMOF-8-2 and Pt/IRMOF-8-3 samples were reduced to 1175, 1071, 1014 m^2/g, 0.59, 0.53 and 0.55 cm^3/g, respectively (Table 3). The BET surface area and pore volume of Pt/IRMOF-8-1, Pt/IRMOF-8-2 and Pt/IRMOF-8-3 were lower than that of the plain IRMOF-8. This is due to the increased weight and partial micropore blockage caused by the doped Pt particles.

High-pressure hydrogen isotherms at 298 K for the plain IRMOF-8, Pt/IRMOF-8-1, Pt/IRMOF-8-2 and Pt/IRMOF-8-3 samples are presented in Figure 12. As shown in Figure 12, IRMOF-8 had a hydrogen storage capacity of ~0.44 wt % at 298 K and 10 MPa. After doping Pt on IRMOF-8, the hydrogen uptakes on Pt/IRMOF-8-1, Pt/IRMOF-8-2 and Pt/IRMOF-8-3 at 10 MPa were enhanced to 0.85, 0.67 and 0.49 wt %, respectively (Table 3). It can be seen that all the Pt/IRMOF-8 samples exhibited higher hydrogen adsorption capacity than the plain IRMOF-8 sample up to 10 MPa. The enhanced hydrogen storage capacity could not be attributed to differences in surface area because the Pt/IRMOF-8 samples have lower surface area than that of the plain IRMOF-

8, as shown by nitrogen adsorption results. The enhancement of hydrogen storage was attributed to the spillover of atomic hydrogen from Pt particles to IRMOF-8. The Ru, Pt, Pd and Ni metals are known as hydrogen dissociation sources, and the enhanced hydrogen storage on various supports by doping these metals has been well observed.[12-48] Another feature observed in the isotherms of Pt/IRMOF-8 was the near linearity. As shown in our previous work as well as in the results by other groups, the spillover isotherms usually appear to be nearly linear. The near linearity in the isotherms has been explained by our phenomenological spillover isotherm model,[52] and indicates that the spillover amounts are far from reaching the limiting capacities.[12]

It is noted that, in our case, the hydrogen storage capacity followed the order of Pt/IRMOF-8-1 > Pt/IRMOF-8-2 > Pt/IRMOF-8-3. The maximum hydrogen uptake reached 0.85 wt % at 10 MPa on Pt/IRMOF-8-1. The reversibility on Pt/IRMOF-8-1 was also evaluated by measuring the desorption branch down to 1 atm. It can be seen that the desorption branch nearly followed the adsorption branch, although there appeared to be a slight hysteresis. After evacuation to a pressure of 1 Pa for 12 hrs at 298 K, total desorption occurred. The second adsorption isotherm was essentially the same as the first adsorption isotherm. The slight hysteresis between the adsorption and desorption branch is likely due to spiltover hydrogen atoms adsorbed on the defective sites on IRMOF-8. The hysteresis is not obvious on Pt/IRMOF-8-3, since less spiltover hydrogen adsorption occurred on it. In comparison with the pristine IRMOF-8, it is notable that the hydrogen adsorption amount of Pt/IRMOF-8-1 was enhanced by a factor of 1.9 (or a 90 % increase). However, the enhancement factors were only 1.5 for Pt/IRMOF-8-2 and 1.1 for Pt/IRMOF-8-3. It is noted that the Pt content difference in the present study (from 4.8

wt% to 7.7 wt%) should not affect the enhancement significantly. Previous studies have shown significant enhancements when the Pt content was ~5-7 wt%.[36,56,57]

The variation in the storage capacities of Pt/IRMOF-8 samples indicates that differences existed among the samples. The Pt/IRMOF-8 samples were characterized by TEM and chemisorption analyses. TEM images of Pt/IRMOF-8-1, Pt/IRMOF-8-2 and Pt/IRMOF-8-3 samples are shown in Figure 13. For each doped sample, the dark spots of Pt particles could be observed. These results further confirm Pt has been successfully doped on the MOF support. The Pt particle size increased with the order of Pt/IRMOF-8-1 < Pt/IRMOF-8-2 < Pt/IRMOF-8-3. The mean particle sizes with standard deviations were 2.2±1.0 nm for Pt/IRMOF-8-1, 3.9±1.9 nm for Pt/IRMOF-8-2, and 9.1±4.3 nm for Pt/IRMOF-8-3. As TEM yielded limited information of the Pt dispersion on the whole sample, hydrogen chemisorption was further used to estimate the metal dispersion. It is known that the Benson–Boudart method is a good assessment for the dispersion of metals on supports. From the adsorbed amount of hydrogen extrapolated to zero pressure, the dispersion of Pt metal on IRMOF-8 can be calculated. Figure 14 shows the H_2 adsorption isotherms on Pt/IRMOF-8-1, Pt/IRMOF-8-2, and Pt/IRMOF-8-3 at 298 K. It is obvious that the dispersion of Pt on MOF followed the order Pt/IRMOF-8-1 > Pt/IRMOF-8-2 > Pt/IRMOF-8-3. These results indicate high dispersion and small sizes of Pt particles facilitate spillover on MOFs and in turn the storage capacity. This is in agreement with the XRD and TEM results. The catalyst size effects on spillover storage on MOF also agreed with the previous studies on carbon receptors doped with various metals. Tsao et al. impregnated activated carbon with Pt particles of ~1-2 nm and achieved an enhancement factor of 3.[35] Chung et al. doped Pt particles (2 nm) on boron-substituted

carbon and obtained a storage capacity 5 times higher than the activated carbon with the same surface area.[36] A high storage capacity on multi-walled carbon nanotubes with a good Pt dispersion was reported by Park's group.[37] Arenillas et al. measured the hydrogen adsorption on carbon nanospheres doped with different loadings of Ni and found that the storage capacity of doped carbon was enhanced by a factor of 1.4 to 2.3.[53] The highest storage capacity was obtained on Ni-doped carbon nanopheres with the best Ni distribution and smaller Ni particles (5 nm). Tsai's group reported that uniformly distributed Ni nanoparticles (2.3 nm) tripled the hydrogen uptake on CNTs.[54] Sandi's group reported the hydrogen uptake on Pd-doped carbon nanofibers was 4 times larger than that on the undoped carbon and attributed the enhancement to small Pd particles.[55] Our recent study on templated carbon doped with various metals (Ru, Pt and Ni) also indicated nanosized catalysts favored high storage capacity.[56] By considering the carbon nature of the linker of MOFs, it is reasonable to observe the high dispersion and small size of Pt particles facilitated the storage capacity of MOF samples. Our previous studies showed that there is a limited area of influence for each particle due to diffusion resistance and lack of diffusion pathways.[57] Thus particles with lower and uneven dispersion cannot affect the entire MOF support, thus resulting in diminished spillover enhancement. The high dispersion and small size of Pt particles contribute to increased contacts with the MOF receptor.

The size of the doped metal is affected by many factors, including the type of metal, the doping/addition rate and loading amount of the metal precursor, and the treatment temperature and metal reduction method. In our case, for doping Pt via CVD method, slower doping led to smaller particles, and the rate of doping could be controlled by a

number of factors. Thus, a lower temperature provided a lower Pt precursor vapor concentration, aided by more evacuation/doping cycles, were favorable for the uniform interactions between precursor and MOFs and consequently, smaller particles with more even distribution. The highest doping temperature and only one evacuation/doping cycle resulted in the largest Pt size. This is similar to the effects of addition rate and concentration of H_2PtCl_6 on Pt dispersion on AX-21.[34] However, further optimizing the doping conditions is still needed for more significant storage enhancements.

This particle size effect on hydrogen spillover was also observed on another system, Ru doped on zeolite Na-Y. The routine method for doping Ru onto sample was described in our previous work.[56] Here, the synthesis conditions were modified to get three samples with Ru of different sizes. Typically, 200 mg of well-dried zeolite Na-Y was dispersed in 20 mL of ethanol and was stirred for 0.5 h in a flask at room temperature. Next 5 mL of ethanol solution was mixed with 800 mg of $Ru(NO)(NO_3)_x(OH)_y$ aqua (1.5 wt % Ru content), then the mixture was slowly added to the above solution under vigorous agitation. The mixture was subjected to ultrasonication (100 W, 42 kHz) for 1 h and then magnetically agitated at room temperature for 24 h. After being dried in an oven at 333 K overnight, the impregnated Na-Y sample was transferred to a horizontal quartz tube and further dried in a He flow at 393 K for 2 h to remove the residual ethanol in the sample. Then the He flow was switched to H_2 and the temperature was increased to 623 K and held for 3 h. After being cooled to room temperature in H_2, the sample was purged with flowing He and stored under He atmosphere before further measurement. This sample is denoted as Ru-NaY-1. The second sample denoted as Ru-NaY-3 was obtained by further calcination of reduced Ru-NaY in Helium at 923K for 1 hour. The third sample Ru-NaY-

2 was obtained in this way: the impregnated Na-Y was first reduced in H_2 at 723K for 1 hour followed by calcination in air at 523K for 1 hour and then reduced again in H_2 at 723K for 1 hour. The particle sizes of Ru on these three samples were examined by using TEM and the corresponding results are shown in Figure 15. Based on Figure 15, the average size with standard deviations for Ru on these three samples were 1.4±0.5 nm for Ru-NaY-1, 6.4±1.8 nm for Ru-NaY-2 and 10.6±4.2 nm for Ru-NaY-3.

Similarly, the hydrogen isotherms on these three samples and pristine Na-Y were also measured by using the same instruments mentioned above and the results are shown in Figure 16. From Figure 16, we can find pristine NaY possessed a hydrogen uptake about 0.28 wt% at 100 atm, which is consistent with literature value.[58] This also demonstrates the accuracy of our measurement instruments. After doping Ru onto pristine NaY, the hydrogen uptakes were significantly enhanced on Ru-NaY-1 by a factor of 2. However, with the Ru size increasing, the hydrogen storage capacity of Ru-NaY decreased gradually. For the sample with very large Ru particles, i.e., Ru-NaY-3, the enhancement of hydrogen uptake due to hydrogen spillover is very small. These results are in good agreement with previous results about Pt doped on IRMOF-8 and demonstrate the high metal dispersion and good contacts between metals and supports are necessary to facilitate the uptake enhancement by utilizing hydrogen spillover.

Conclusions

In this work, a series of Pt-doped IRMOF-8 samples have been prepared via organometallic chemical vapor deposition. The catalyst (Pt) size was affected by the doping temperature and number of doping cycles. The hydrogen storage studies showed the storage capacities via hydrogen spillover on Pt-doped IRMOF-8 samples were

enhanced by a factor 1.1 – 1.9 when compared to undoped IRMOF-8. Catalyst size was a crucial factor that determined the enhancements of the storage capacity of Pt-doped MOFs.

Acknowledgements

This work was supported by the NSF grant CBET-0753008.

Note

The contents of this chapter hae been published in J. Phys. Chem. C 2011, 115, 4793.

References:

1. Department of Energy (DOE), A Multiyear Plan for the Hydrogen R&D Program, Office of Power Delivery, Office of Power Technologies, Energy Efficiency and Renewable Energy, USA, 1999.
2. Seayad, A. M.; Antonelli, D. M. Adv. Mater. 2004, 16, 765.
3. Frost, H.; Snurr, R. Q. J. Phys. Chem. C 2007, 111, 18794.
4. Roswell, J.; Yaghi, O. M. Angew. Chem., Int. Ed. 2005, 44, 4670.
5. Murray, L. J.; Dinca, M.; Long, J. R. Chem. Soc. Rev. 2009, 38, 1294.
6. Collins, D. J.; Zhou, H.-C. J. Mater. Chem. 2007, 30, 3154.
7. Zhao, D.; Yuan, D.; Zhou, H.-C. Energy Environ. Sci. 2008, 1, 222.
8. Chae, H.; Siberio-Perez, D. Y.; Kim, J.; Go, Y.; Eddaoudi, M.; Matzger, A.; O'Keeffe, M.; Yaghi, O. M. Nature 2004, 427, 523.
9. Furukawa, H.; Miller, M.; Yaghi, O. M. J. Mater. Chem. 2007, 17, 3197.
10. Ferey, G.; Mellot-Draznieks, C.; Serre, C.; Millange, F.; Dutour, J.; Surble, S.; Margiolaki, I. Science 2005, 309, 2040.
11. Latroche, M.; Surblé, S.; Serre, C.; Mellot-Draznieks, C.; Llewellyn, P.L.; Lee, J.-H.; Chang, J.-S.; Jhung, S. H.; Férey, G. Angew. Chem., Int. Ed. 2006, 45, 8227.
12. Wang, L.; Yang, R. T. Catal. Rev.– Sci. Eng. 2010, 54, 411.
13. Robell, A. J.; Ballou, E. V.; Boudart, M. J. Phys. Chem. 1964, 68, 2748.
14. Srinivas, S. T.; Rao, P. K. J. Catal. 1994, 148, 470.
15. Conner, W. C., Jr. and Falconer, J. L. Chem. Rev. 1995, 95, 759
16. Pajonk, G. M. Appl. Catal. A 2000, 202, 157.
17. Bond, G. C. in: Twigg M.V.; Spencer M. S. (Eds.), Metal-Catalyzed Reactions of Hydrocarbons, Springer. New York, 2005, p. 118.
18. Wang, L.; Yang, R. T. Energy Environ. Sci. 2008, 1, 268.
19. Sinfelt, J. H.; Lucchesi, P. J. J. Am. Chem. Soc. 1963, 85, 3365.
20. Khoobiar, S. J. Phys. Chem. 1964, 68, 411.
21. Boudart, M.; Aldag, A. W.; Vannice, M. A. J. Catal. 1970, 18, 46.
22. Mitchell, P. C. H.; Ramirez-Cuesta, A. J.; Parker, S. F.; Tomkinson, J.; Thompsett, D. J. Phys. Chem. B 2003, 107, 6838.
23. Mitchell, P. C. H.; Ramirez-Cuesta, A. J.; Parker, S. F.; Tomkinson, J. J. Mol. Struct. 2003, 651-653, 781.
24. Tsao, C.-S.; Liu, Y.; Li, M.; Zhang, Y.; Leao, J. B.; Chang; H.-W.; Yu, M.-S.; Chen, S.-H. J. Phys. Chem. Lett. 2010, 1, 1569.
25. Zhan, D.; Velmurugan, J.; Mirkin, M. V. J. Am. Chem. Soc. 2009, 131, 14756.
26. Panayotov D. A.; Yates Jr., J. T. J. Phys. Chem. C 2007, 111, 2959.
27. Chen, L.; Cooper, A. C.; Pez, G. P.; Cheng, H. S. J. Phys. Chem. C 2007, 111, 18995.
28. Sha, X.; Knippenberg, M. T.; Cooper, A. C.; Pez, G. P.; Cheng, H. S. J. Phys. Chem. C 2008, 112, 17465.
29. Singh, A. K.; Ribas, M. A.; Yakobson, B. I. ACS Nano 2009, 3, 1657.
30. Lin, Y.; Ding, F.; Yakobson, B. I. Phys. Rev. B: Condens. Matter. 2008, 78, 041402-1.
31. Psofogiannakis, G. M.; Froudakis, G. E. J. Phys. Chem. C 2009, 113, 14908.
32. Zhu, Z. H.; Lu, G. Q.; Hatori, H. J. Phys. Chem. B 2006, 110, 1249.
33. Suri, M.; Dornfeld, M.; Ganz, E. J. Chem. Phys. 2009, 131, 174703.
34. Stuckert, N. R.; Wang, L.; Yang, R. T. Langmuir 2010, 26, 11963.

35. Tsao, C. S.; Tzeng, Y. R.; Yu, M. S.; Wang, C. Y.; Tseng, H. H.; Chung, T. Y.; Wu, H. C.; Yamamoto, T.; Kaneko, K.; Chen, S. H. J. Phys. Chem. Lett. 2010, 1, 1060.
36. Jeong, Y.; Chung, T. C. M. Carbon 2011, 49, 140.
37. Park, S.-J.; Lee, S.-Y. Int. J. Hydrogen Energy 2010, 35, 13048.
38. Li, Y.; Yang, R. T. J. Am. Chem. Soc. 2006, 128, 8136.
39. Yang, R. T.; Li, Y. W.; Lachawiec. A. J. 2007 Annual Progress Report, DOE Hydrogen Program; U. S. Department of Energy: Washington, DC, 2007; IV. C.1b, 539.
40. Wang, C.-Y.; Tsao, C.-S.; Yu, M.-S.; Liao, P.-Y.; Chung, T.-Y.; Wu, H.-C.; Miller, M. A.; Tzeng, Y.-R. J. Alloys Comp. 2010, 492, 88.
41. Miller, M. A.; Wang, C.-Y.; Merrill, G. N. J. Phys. Chem. C 2009, 113(8), 3222–3231.
42. Tsao, C.-S.; Yu, M.-S.; Wang, C.-Y.; Liao, P.-Y.; Chen, H.-L.; Jeng, U-S.; Tzeng, Y.-R.; Chung, T.-Y.; Wu, H.-C. J. Am. Chem. Soc. 2009, 131, 1404.
43. Liu, Y.-Y.; Zeng, J.-L.; Zhang, J.; Xu, F.; Sun, L.-X. Inter. J. Hydrogen Energy 2007, 32, 4005.
44. S. J. Yang, J. H. Cho, K. S. Nahm, C. R. Park, Int. J. Hydrogen Energy 2010, 35, 13062.
45. Liu, Y. Y.; Zhang, J.; Zeng, J. L.; Chu, H. L.; Xu, F.; Sun, L. X. Chin. J. Catal. 2008, 29, 655.
46. Proch, S.; Herrmannsdofer, J.; Kempe, R.; Kern, C.; Jess, A.; Seyfarth, L.; Senker, J. Chem. Eur. J. 2008, 14, 8204.
47. Zlotea, C.; Campesi, R.; Cuevas, F.; Leroy, E.; Dibandjo, P.; Volkringer, C.; Loiseau, T.; Ferey, G.; Latroche, M. J. Am. Chem. Soc. 2010, 132, 2991.
48. Cheon, Y. E.; Suh, M. P. Angew. Chem., Int. Ed. 2009, 48, 2899.
49. Yaghi, O. M.; Eddaoudi, M.; Li, H.; Kim, J.; Rosi, N. U.S. Patent No. 6,930,193 B2, 2005.
50. Tsao, C. S.; Yu, M. S.; Chung, T. Y.; Wu, H. C.; Wang, C. Y.; Chang, K. S.; Chen, H. L. J. Am. Chem. Soc. 2007, 129, 15997.
51. Lachawiec, A. J.; DiRaimondo, T. R.; Yang, R. T. Rev. Sci. Instrum. 2008, 79, 063906.
52. Li, Y.; Yang, F. H.; Yang, R. T. J. Phys. Chem. C 2007, 111, 3405.
53. Zubizarreta, L.; Menndez, J. A.; Pis, J. J.; Arenillas, A. Int. J. Hydrogen Energy 2009, 34, 3070.
54. Lin, K.-Y.; Tsai, W.-T.; Yang, T.-J. J. Power Sources doi:10.1016/j.jpowsour.2010.04.026.
55. Back, C.-K.; Sandi, G.; Prakash, J.; Hranisavljevic, J. J. Phys. Chem. B 2009, 110, 16225.
56. Wang, L.; Yang, R. T. J. Phys. Chem. C 2008, 112, 12486.
57. Lachawiec, A. J.; Yang, R. T. Langmuir 2008, 24, 6159.
58. Ding, R.; Zhu, Z.; Yao, X.; Yan, Z.; Lu, M. Catal. Today 2010, 158, 317.

Sample	BET Surface Area (m^2/g)	Pore Volume (cm^3/g)	Pt Content (wt %)	Average Pt size (nm)	H_2 uptake at 10 MPa (wt %)
IRMOF-8	1430	0.69	–	–	0.44
Pt/IRMOF-8-1	1175	0.59	4.8	2.2	0.85
Pt/IRMOF-8-2	1071	0.53	6.2	3.9	0.67
Pt/IRMOF-8-3	1014	0.55	7.7	9.1	0.49

Table 3. Textural parameters, Pt content, Pt size and hydogen uptake on various samples.

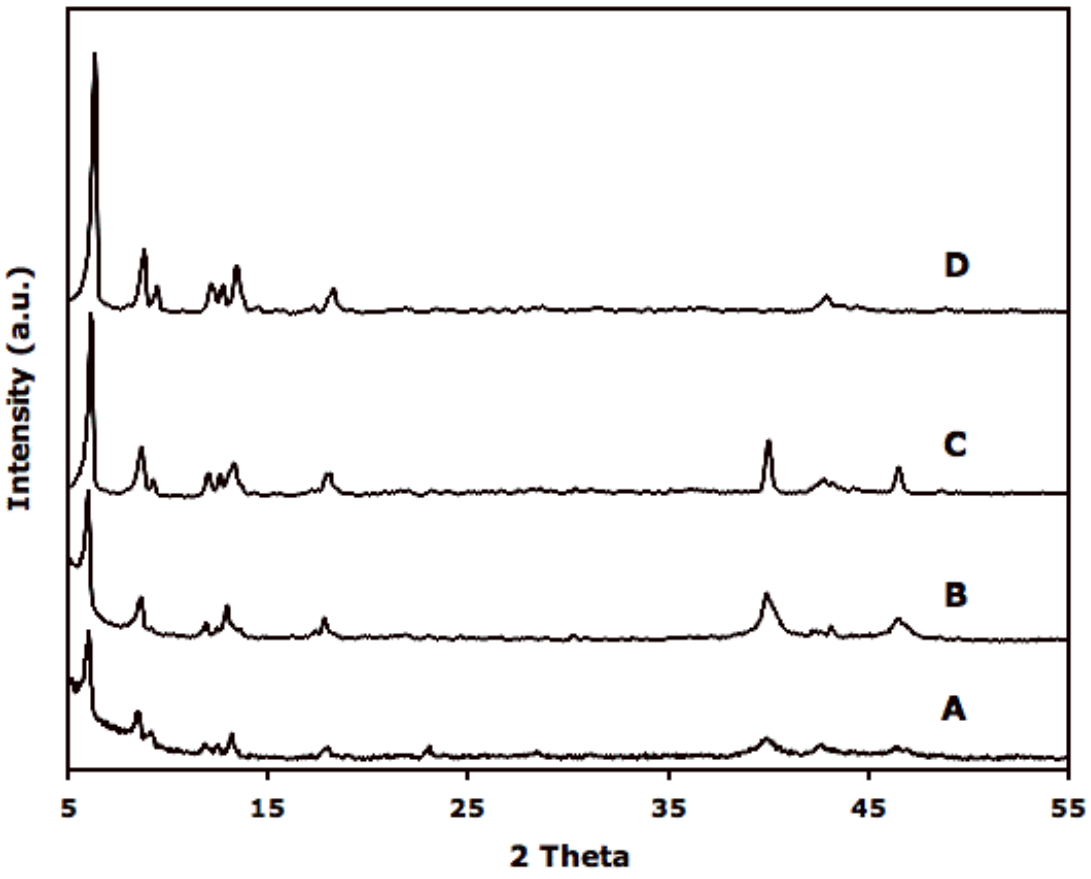

Figure 10. XRD patterns of Pt/IRMOF-8-1 (A), Pt/IRMOF-8-2 (B), Pt/IRMOF-8-3 (C) and pure IRMOF-8 (D).

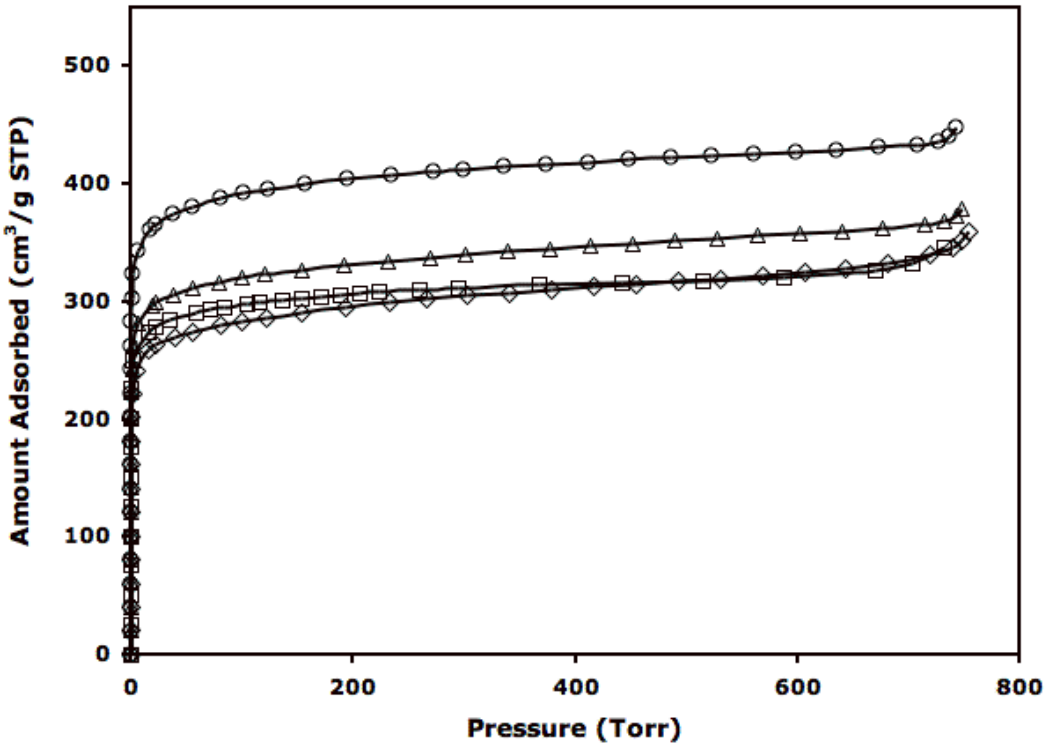

Figure 11. Nitrogen isotherms of Pt/IRMOF-8-1 (△), Pt/IRMOF-8-2 (□), Pt/IRMOF-8-3 (◇) and pure IRMOF-8 (○).

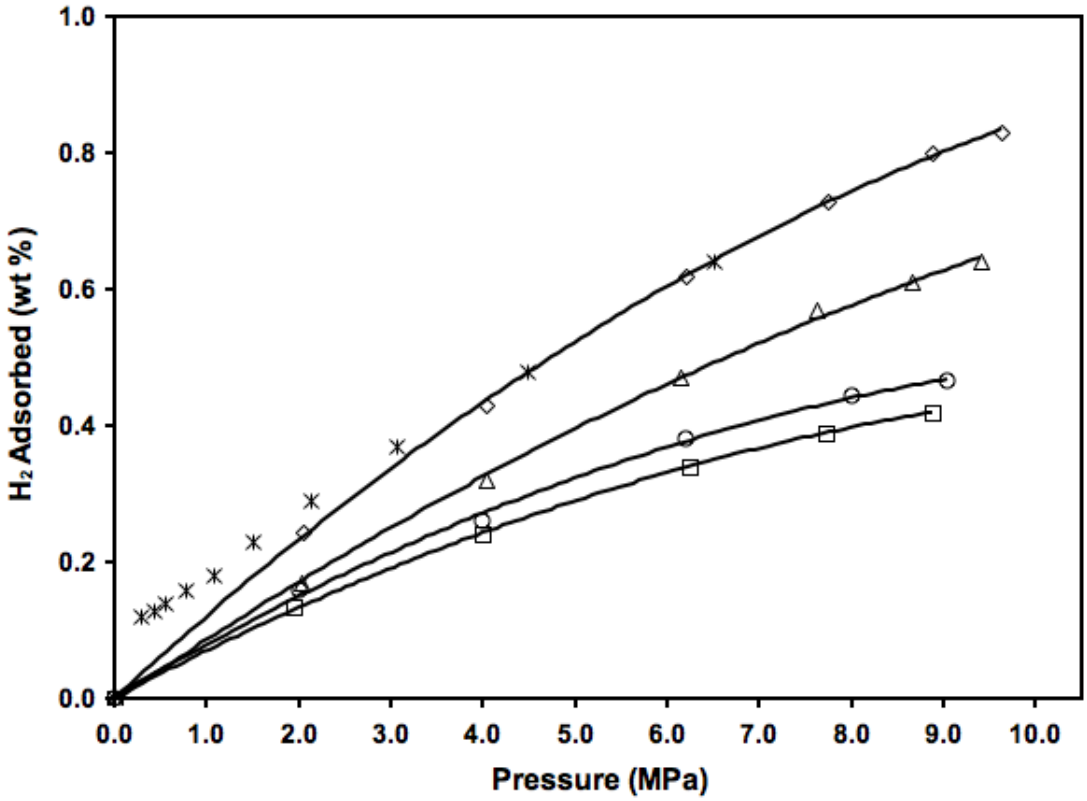

Figure 12. High-pressure hydrogen adsorption isotherms at 298 K for plain IRMOF-8 (□), Pt/IRMOF-8-1 (◇), Pt/IRMOF-8-2 (△) and Pt/IRMOF-8-3 (○) samples and desorption on Pt/IRMOF-8-1 (∗).

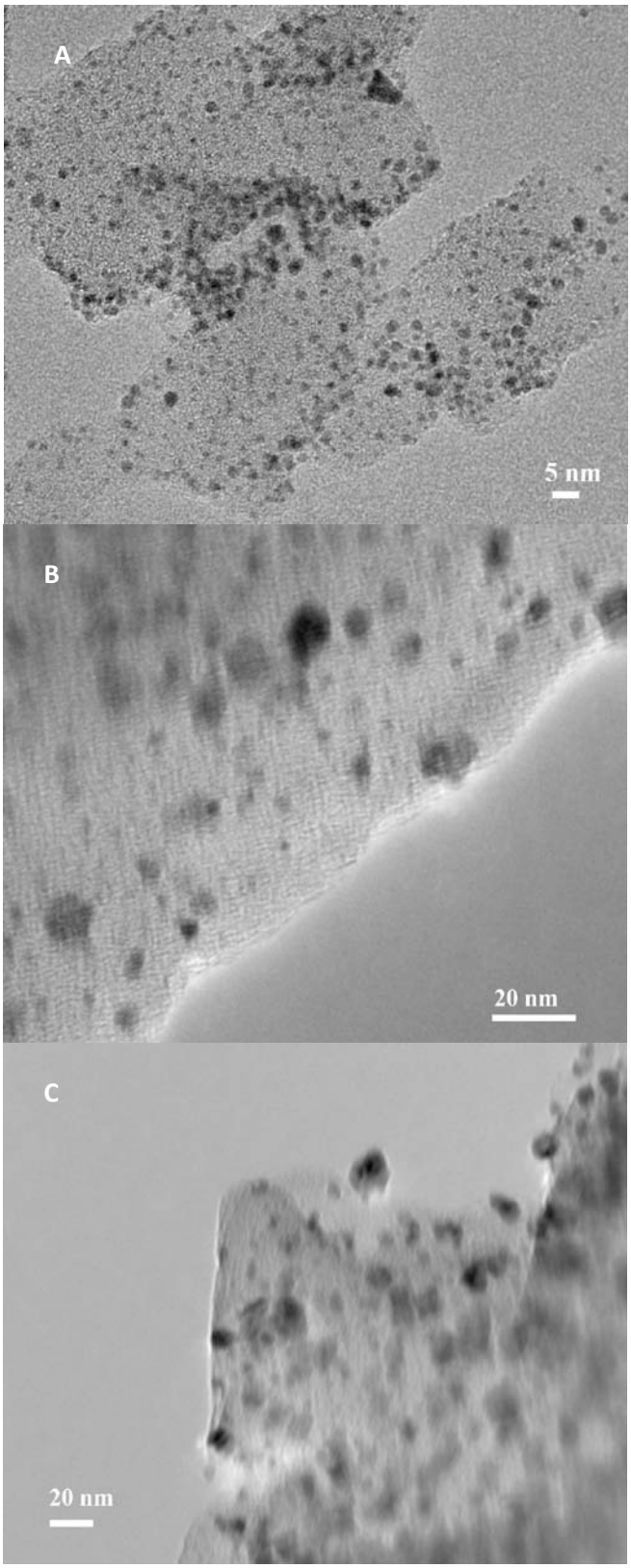

Figure 13. TEM images of Pt/IRMOF-8-1 (A), Pt/IRMOF-8-2 (B) and Pt/IRMOF-8-3 (C).

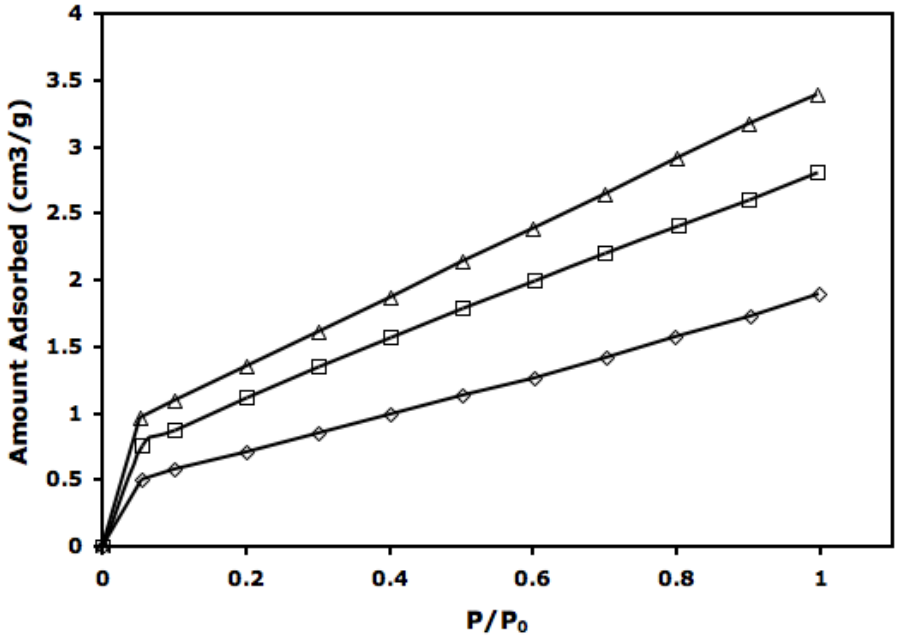

Figure 14. Hydrogen isotherms of Pt/IRMOF-8-1 (△), Pt/IRMOF-8-2 (□) and Pt/IRMOF-8-3 (◇).

(A)

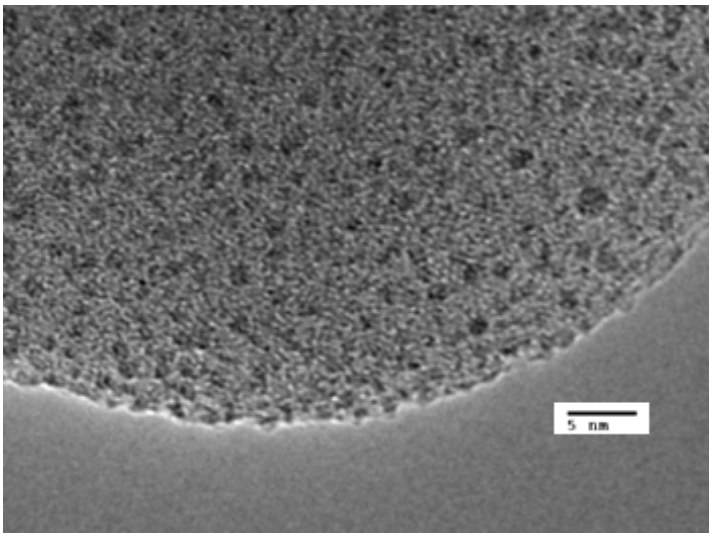

(B)

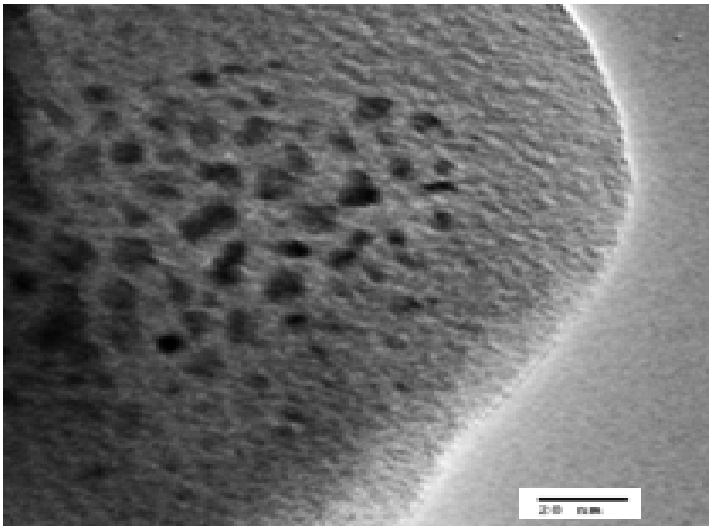

(C)

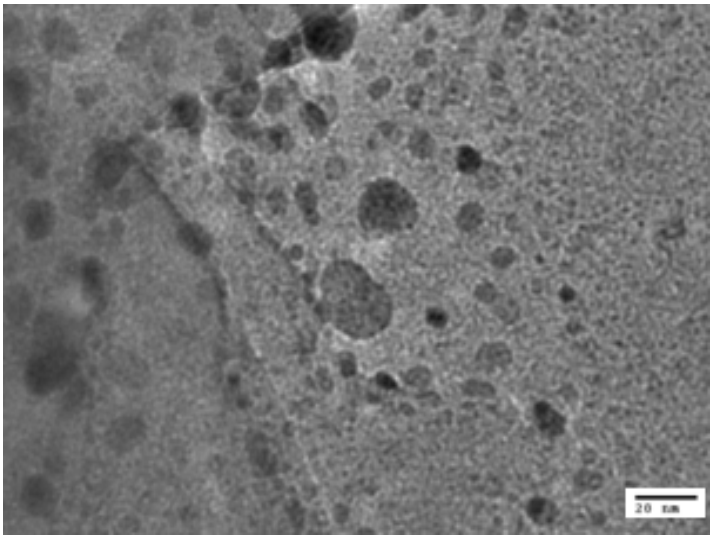

Figure 15. TEM images of (A) Ru-NaY-1 (B) Ru-NaY-2 (C) Ru-NaY-3

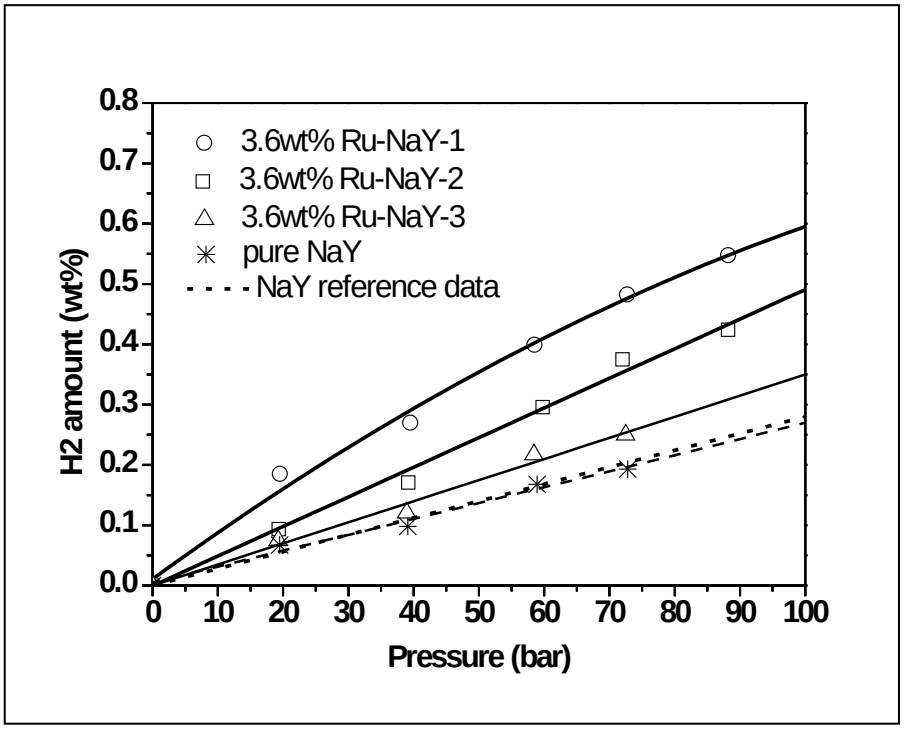

Figure 16. High pressure hydrogen isotherms on NaY, Ru-NaY-1, Ru-NaY-2 and Ru-NaY-3

Chapter 3: Investigation of Hydrogenation of Metal-Organic Frameworks HKUST-1, MIL-53 and ZIF-8 by Hydrogen Spillover

Introduction

Hydrogen is considered as one promising alternative energy carrier for environmental sustainability.[1] Among many factors hindering the wide deployment of hydrogen as hydrocarbon fuel substitution, hydrogen storage is one of the key issues for commercialization of fuel cell powered vehicles using hydrogen as energy carrier due to the low volumetric energy density of hydrogen, which is only 1/3000 of the volumetric energy density of gasoline.[2] Many adsorbent materials have been developed as possible candidates for hydrogen storage over the past few decades.[3-10] Among these candidates, metal organic frameworks (MOFs), a class of porous crystalline materials consisting of metal ions or metal containing clusters coordinated to rigid organic molecules to form one, two, or three dimensional structures, have attracted much attention because of their light weight, exceptional high surface area, high porosity, and chemically-tunable structures.[11-28]

There has been an intense search for MOFs with high hydrogen storage capacities. Significant progress has been achieved for hydrogen storages at 77 K. For example, MIL-101 with a Langmuir surface area of 5500 m^2/g possessed a storage capacity of 6.1 wt% at 8 MPa and 77 K.[29] The hydrogen adsorption capacity at 77 K by MOF-177 (BET surface area 4750 m^2/g) and UMCM-2 (BET surface area 5200 m^2/g) reached 7.5 wt% at 7 MPa and 7 wt% at 6 MPa, respectively.[30,31] Furukawa et al reported MOF-210 with a record BET surface area of 6240 m^2/g and a hydrogen capacity of 8.6 wt% at 77K and 8 MPa.[32] More recently, Farha et al. reported that NU-100, which has a slightly smaller

surface area (BET 6143 m^2/g) but much higher hydrogen storage capacity (9.95 wt% at 77 K and 6 MPa).[33] The MOF with highest surface area so far was NU-110, with a BET S.A. 7140 m^2/g but no hydrogen uptake capacity reported.[34] However, these significant storage capacities were achieved only at 77 K and they declined dramatically when the temperature was raised to ambient temperature. This is understandable since hydrogen adsorption on pristine MOFs was by weak physisorption and mainly dominated by weak van der Waals interactions.

In order to improve the performance of adsorbent materials for hydrogen storage at ambient temperature, an effective approach was proposed by utilizing hydrogen dissociation on metal surface followed by spillover. General concept of hydrogen spillover could be defined as dissociative chemisorptions of hydrogen on metal nanoparticles and subsequent migration of dissociated hydrogen atoms onto adjacent receptor surfaces via diffusion.[35-38] Up to date, over 140 papers published by more than 50 groups have demonstrated the effectiveness of utilizing hydrogen spillover for storage enhancement on adsorbents at room temperature.[39] First evidence of atomic hydrogen spillover was observed by Sinfelt and Lucchesi in studies of ethylene hydrogenation by H atoms spillover from Pt/SiO_2 to Al_2O_3.[40] Later, Khoobiar showed WO_3 in contact with a Pt catalyst could be reduced by H_2 to blue-colored WO_{3-x}.[41] In 1971, Pajonk and Teichner found that a pure support (Al_2O_3 or SiO_2) treated with H_2 for several hours at elevated temperature can hydrogenate ethylene and benzene even by indirect contact with a supported metal catalyst.[42] Reduction of transition metal oxide with Pt catalyst has been used as the proof of hydrogen spillover by Khoobiar, Bourdart and Bond et al.[41,43-45] Direct experimental evidences of atomic hydrogen spillover at room temperature have

been recently reported in many systems (Pt-carbon[46-50], Pt-glass[51] and Au-TiO_2[52,53]) by using inelastic neutron scattering, XPS, nanoelectrochemcial approaches and FT-IR. Meanwhile, atomistic simulations have also demonstrated the feasibility of hydrogen spillover from metal clusters to receptors. Cheng et al. found migration of H atoms from a Pt cluster catalyst to graphitic carbon substrates occurs via physisorbed of H atoms at room temperature by using DFT calculations.[54,55] The works from Yakobson's group illustrated thermodynamic and kinetic possibility of hydrogen spillover process at room temperature from unsupported or the receptor-supported clusters to graphene sheet through *ab initio* calculations.[56,57] Zhang and coworkers demonstrated the presence of zinc vacancies in IRMOFs could substantially lower the energies and barriers to enable hydrogen spillover at ambient conditions,[58] which is consistent with experiment results that defects in MOFs play an important role in hydrogen spillover at ambient temperature.[59] Moreover, hydrogen storage capacities via spillover for various MOFs and COFs have been calculated.[58,60-65]

Three major approaches have been reported to facilitate hydrogen spillover on MOFs, which is building carbon bridges between dissociation metals and MOFs,[59,60,66-70] encapsulating Pt/C sources into frameworks of MOFs during synthesis,[71,72] and direct doping dissociation metals (Pt, Pd, Ni) onto MOFs.[73-78] Many factors could affect the reproducibility of hydrogen spillover enhancement by bridge-building and it was suggested the ideal situation for hydrogen spillover on bridged MOFs was all individual catalyst connected with MOF particles via "bridges", which was highly empirical and difficult to achieve.[68] Unlike high uncertainty of MOF-bridging technique, direct doping metals onto MOFs attracted much attention because of more controllable and reliable

synthesis procedure, which led to higher reproducibility. Significant storage capacity enhancements via direct metal-doping have been reported by many groups. Suh and coworkers have developed novel methods for producing metal nanoparticles in MOFs by using redox reactions between the redox-active MOFs and metal ions such as Ag(I), Au(III), and Pd(II).[76,79,80] They demonstrated palladium nanoparticles could be embedded into a redox-active MOF simply by immersion of the MOF solid into $Pd(NO_3)_2$ solution at room temperature without further reduction and observed an enhancement factor of 2.3 at 298 K and 9.5 MPa.[76] Our group synthesized a series of Pt-doped IRMOF-8 via organometallic chemical-vapor deposition and observed enhancements from 10-100% depending on the particle size.[78] Hydrogen uptake enhancements were also observed on Ni doped MIL-101,[73] Pt doped MOF-177,[74]Pd doped MIL-100,[75]Pd doped MOF-5,[77] and Pd doped COF-102.[81]

The recent review from Suh's group summarized different designs and synthesis approaches of MOFs for hydrogen storage, discussed the strategies for improving hydrogen adsorption on MOFs and reviewed various techniques and methods for hydrogen sorption experiments.[82] They also pointed out that the discovery of a MOF with a large surface and high H_2 adsorption energy at room temperature does not guarantee it will be useful as a H_2 storage material, since industrial applications of MOFs require MOFs to remain stable against moisture, air and other gas impurities.[82] Thermal stabilities in inert gas and moisture/air/chemical resistance of MOFs have been studied by many researchers.[83-91] Walton and coworkers presented experimental investigations of water adsorption in MOFs at room temperature and up to 90% relative humidity, which demonstrated HKUST-1, MOF-74 and UiO-66 maintained good structural stability

against moisture while DMOF-1, DMOF-1-NH_2 and UMCM-1 underwent complete loss of crystallinity.[90] Meanwhile, they also suggested that the thermal stability of MOFs is determined by the coordination number and local coordination environment instead of framework topology by applying TGA-DSC measurements in helium.[91] However, the stabilities of MOFs in hydrogen atmosphere were seldom investigated. Lueking's group mixed HKUST-1 with commercial Pt/C catalyst and observed that hydrogenation of HKUST-1 happened to the carboxylate groups and not aromatic carbons, but the state of metal clusters after hydrogenation still remains unknown.[92] Since MOFs are promising candidate materials for hydrogen storage, it's important to understand MOFs' stabilities in hydrogen atmosphere. Dissociated hydrogen possesses stronger chemical reactivity than dihydrogen molecules, thus stability of MOFs in the presence of dissociated hydrogen remains an issue especially when spillover of hydrogen is applied to enhance hydrogen storage capacity of pristine MOFs. In this work, the stabilities of three types of moisture stable MOFs with different metal clusters, i.e. HKUST-1 (Cu), MIL-53 (Al) and ZIF-8 (Zn), were studied in dihydrogen and dissociated hydrogen environments. To induce dissociated hydrogen to these MOFs, colloidal Pt nanoparticles were doped on MOFs via incipient wetness for the first time. The influence of dissociated hydrogen and dihydrogen molecules on the stabilities of MOFs with different metal clusters was investigated and compared. The stabilities of Pt-doped HKUST-1 samples synthesized by chemical vapor deposition (CVD) and incipient wetness were also compared to see the effect of contact between doped Pt particles (dissociation source) and MOFs (receptor) on hydrogen spillover.

Experimental Section

Sample synthesis. Copper (II) nitrate hemipentahydrate $Cu(NO_3)_2 \cdot 2.5H_2O$, NaOH, benzene-1,3,5-tricarboxylic acid (H_3-BTC), hexachloroplatinic acid $H_2PtCl_6 \cdot 6H_2O$ (99.9%, metals basis), MIL-53(Al) (Basolite A100), ZIF-8 (Basolite Z1200), ethanol, N,N-dimethylformamide (DMF), ethylene glycol and chloroform were obtained from Sigma-Aldrich. Helium, nitrogen and ultra high purity grade hydrogen (99.995%) were obtained from Metro Welding Company.

Synthesis of HKUST-1. Typically, 1 gram of $Cu(NO_3)_2 \cdot 2.5H_2O$ and 0.5 gram of H_3-BTC were dissolved in 25 ml solvent consisting of equal parts of deionized water, ethanol and DMF. The mixture was stirred for 15 min at room temperature and then transferred into a Pyrex bottle. The bottle was tightly capped and placed in an 85 °C oven for 20 h to yield small octahedral crystals. After decanting the mother liquor and rinsing with DMF, the product was immersed in chloroform for 1 day, after which the activation solvent was decanted and new chloroform was replenished. This solvent exchange procedure was repeated for 3 times and HKUST-1 was filtered and calcined under vacuo at 160°C to remove excessive solvent, yielding the porous material.[18,93,94]

Synthesis of Platinum Nanoparticles. A routine method for Pt nanoparticle synthesis by using polyol reduction has been reported in previous literature.[95-97] A brief introduction is given here. Typically, 0.25 gram of NaOH and 0.25 gram of $H_2PtCl_6 \cdot 6H_2O$ was separately dissolved and stirred in two parts of 12.5 ml ethylene glycol at room temperature. After that, the solution of platinum precursor was slowly dropped into NaOH solution. The solution mixture was kept well-stirred for 30min at room temperature and then heated at 160°C for 3 hours being accompanied by N_2 bubbling. During this process, the solution turned from yellow color into dark brown. A

6-mL aliquot of the resulting solution was transferred to a vial. The particles were precipitated by adding 1 mL of 2 M HCl into the solution, followed by being washed in ethanol and finally obtained by high speed centrifuge.

Synthesis of Pt-HKUST-1, Pt-MIL-53 and Pt-ZIF-8 via incipient wetness. HKUST-1 was dried in vacuo at 160°C overnight before usage while MIL-53 and ZIF-8 were dried in vacuo at 300°C overnight before usage. All MOFs crystals were ground (for better doping or mixing) before CVD doping or mixing with Pt nanoparticles. Freshly made Pt nanoparticles were dispersed in about 1 ml of ethanol. The colloidal solution was then added into a small vial containing 0.2 gram of pre-dried HKUST-1. The mixture was ultrasonicated for 15min and dried in a 60°C oven. Before further experiments, the obtained Pt-HKUST-1 was subject to evacuation at 160°C to remove residual ethanol. Pt-MIL-53 and Pt-ZIF-8 were obtained by following the same procedure. The Pt contents in HKUST-1, MIL-53 and ZIF-8 were estimated to be about 5.2% in HKUST-1, 5.0% in MIL-53 and 5.3% in ZIF-8 by XPS analysis, respectively.

Hydrogenation experiments of Pt-HKUST-1, Pt-MIL-53 and Pt-ZIF-8. Pt-HKUST-1 obtained by incipient wetness method was transferred onto a quartz boat and then placed in a horizontal furnace tube. The furnace tube was sealed and purged with H_2 at a flow rate of 60 cc/min. The sample was heated from room temperature at a constant heating rate of 2°C/min to 150°C and held at 150°C for 16 hours. After that, the sample was cooled down to room temperature, purged with N_2 for 1 hour and then subject to evacuation at 160°C overnight before further measurements. The sample obtained by this way was denoted as Pt-HKU-150. For Pt-HKUST-1 samples subject to other H_2 treatment temperatures of 100°C, 75°C, 50°C and 25°C were denoted as Pt-HKU-100,

Pt-HKU-75, Pt-HKU-50 and Pt-HKU-25, respectively. Following the same approach, HKUST-1 processed at 150°C and 100°C were denoted as HKU-150 and HKU-100. MIL-53, ZIF-8, Pt-MIL-53 and Pt-ZIF-8 were also processed by the same procedure but only treated in H_2 at 150°C, which were denoted as MIL-53-150, ZIF-8-150, Pt-MIL-53-150 and Pt-ZIF-8-150, respectively. In our previous study, it was shown that the spillover equilibrium on MOFs was completed within 5 hours at room temperature, thus 16 hours was sufficient for reaching equilibrium of hydrogen spillover on these samples.[61]

All synthesized H_2 treated samples were stored in desiccators to minimize exposure to ambient air before being subjected to XPS and other measurements.

Synthesis of Pt-HKUST-1 via chemical vapor deposition (CVD). Pt was doped on HKUST-1 by chemical vapor deposition of a volatile platinum precursor (trimethyl)-methylcyclopentadienyl platinum (IV). The detailed procedure was reported in our previous work.[98] HKUST-1 was ground before CVD. The grounded HKUST-1 (0.6 g) and the organometallic precursor (0.09 g) were placed in a tube separated by a glass frit and degassed to a vacuo of <10 μmHg at 0°C. After that, the degassing was stopped and temperature was increased to 30°C and held at 30°C for 1 hour. The evauation of this system was renewed every hour for six cycles and then stayed for another 6 hours. The yielded composite was reduced in a hydrogen atmosphere at 150°C overnight and then purged with flowing helium. The obtained Pt-HKUST-1 by this way was designated as Pt-HKU-CVD.

Sample characterization and isotherm measurements. Powder X-ray diffraction (XRD) data were recorded on a Rigaku Rotating Anode X-ray diffractometer at 40KV, 100mA for Cu Kα (λ=0.1541nm) radiation, with a step size of 0.02° in 2θ. All

the XRD patterns were obtained on the ground MOFs and doped MOFs because a flat surface of sample is needed for XRD analysis. X-ray photoelectron spectroscopy (XPS) and X-ray-excited auger electron spectroscopy (XAES) data was recorded on a Kratos Axis ultra XPS spectrometer (mono Al source) at 14KV, 8mA, with a resolution of pass energy 10 eV. BET (Brunauer-Emmett-Teller) surface areas were measured with a standard static volumetric technique (Micromeritics ASAP2020).

Results and discussion

Conventional method for doping metal nanoparticles onto MOFs usually involves two steps: infiltration of metal precursors into frameworks followed by reduction of the metal precursor in H_2 atmosphere at one specific high temperature (e.g. 200 ^{o}C).[75,77,78] Since the obtained metal-doped MOFs have been treated in H_2 at high temperature, one cannot examine the stabilities of MOFs in H_2 at the temperature lower than the reduction temperature. In order to study the stabilities of MOFs at various temperatures, a new method is used in this study, i.e. colloidal Pt nanoparticles were synthesized by ethylene glycol reduction, then the reduced Pt nanoparticles was doped on MOFs via incipient wetness impregnation at room temperature. The operation at room temperature allowed us to study the stabilities of doped MOFs in H_2 at various temperatures.

Structural losses of porous materials including MOFs are commonly studied using powder XRD and surface area measurements. For example, Long's group used XRD and BET surface area to estimate the structural changes of MOF-5 by different preparation and handling methods,[11] and Walton el al. also used XRD and BET surface area to study the structural degradation of several MOFs exposed to water vapor.[90]

Powder X-ray diffraction patterns of as obtained HKUST-1, HKU-100 and HKU-150 are shown in Figure 17. The pristine HKUST-1 consists of a face-centered cubic crystal lattice of $Fm\bar{3}m$ space group and possesses typical peaks at 2θ=9.5° (220), 11.7° (222), 13.5° (400), 14.7° (331), 16.5°(422), 17.5° (511) and 19.1° (440), which is in good agreement with previous reports.[92,93,99] After being exposed in hydrogen environment at 100 and 150°C for 16 hours, HKU-100 and HKU-150 exhibited the same peaks with those of pristine HKUST-1, although the peak intensity decreased slightly. BET surface area measurements also showed that the surface area of HKUST-1 dropped slightly from 1150 m^2/g to 992 and 901 m^2/g after being treated in hydrogen atmosphere at 100 and 150°C for 16 hours, respectively. This means the major crystalline integrity of HKUST-1 remained intact after exposure to hydrogen molecules at elevated temperatures.

Lueking et al. showed that hydrogenation of HKUST-1 mixed with Pt/C catalyst happened to carboxylate groups and not aromatic carbons, but the valence state of copper in HKUST-1 remained unknown.[92] In order to investigate the state of copper cluster, X-ray photoelectron spectroscopy was conducted around the characteristic peak range of copper, 930 to 965 eV. The X-ray photoelectron spectra of HKUST-1, HKU-100 and HKU-150 are shown in Figure 18. Two characteristic peaks of divalent Cu^{2+} were observed at 934.6 and 954.4 eV, corresponding to Cu $2p_{3/2}$ and Cu $2p_{1/2}$, respectively.[100-102] Meanwhile, the presence of the well known "shake-up satellites" (which are the other peaks appeared in the range of 930-965 eV except the two characteristic peaks) found in Cu spectra is generally considered as an indication of the presence of Cu (II) species. [103-107] We note that there was also a very small, barely noticeable Cu^0 shoulder at 932 eV in Cu 2p XPS of HKU-100 and HKU-150. This was caused by partial Cu reduction (a very

small fraction). However, all these results indicated almost all copper element in HKUST-1 remained as divalent state after exposure to hydrogen at elevated temperatures for a prolonged time, which means pristine HKUST-1 is stable in H_2 up to 150°C.

Since dissociated hydrogen with unshared electrons possess higher chemical reactivity than stable dihydrogen molecules,[108] it's important to investigate the stability of HKUST-1 in the presence of dissociated hydrogen although the stabilities in dihydrogen environment at elevated temperatures have been verified above. In order to induce dissociated hydrogen to MOFs, Pt nanoparticles were doped onto HKUST-1 by incipient wetness method as described in the experimental section. Hydrogen molecules first chemisorbed and dissociated on the surface of Pt and then migrated from Pt surface to the surface of HKUST-1 followed by surface diffusion. The resulting HKUST-1 samples treated with dissociated hydrogen were examined by XRD and XPS. Powder XRD patterns of pristine HKUST-1, Pt-doped HKUST-1 before and after H_2 treatment at 150°C are shown in Figure 19.

As shown in Figure 19, the peak intensity of Pt-HKUST-1 was slightly lower than that of pristine HKUST-1. Nitrogen adsorption results also showed that the surface area of HKUST-1 decreased from 1150 to 960 m^2/g after Pt-doping procedure. The lower surface area of Pt-HKUST-1 than HKUST-1 was due to the increased weight and the pore blocking of HKUST-1 caused by Pt nanoparticles. TEM image of Pt-HKUST-1 showed that Pt nanoparticles of slightly below 1 to approximately 10 nm were doped on the crystal of HKUST-1 (Figure 29). It is worth noting that the decrease in BET surface area of MOFs after metal-doping procedure is a normal phenomenon reported in many

previous studies.[74-76,78,109,110] The surface areas of MOFs before and after metal doping observed in previous literature and our work are compared in Table 4 below.

Although the peak intensity and BET surface area of HKUST-1 decreased after Pt-doping, the structure of HKUST-1 was retained and no extra peak appeared in XRD pattern. However, after being subjected to H_2 treatment at 150°C for 16 h, the peak intensities of Pt-HKUST-1 declined substantially. This was also confirmed by BET surface area measurement: BET surface area of Pt-HKUST-1 dropped severely from 960 to 151 m^2/g upon H_2 treatment at 150°C. Moreover, a new strong peak around $2\theta = 43.2°$ emerged (shown in inset figure), which is characteristic peak of Cu^0 species at (111) plane.[109-112] Compared with the inset figure in Figure 17, we could find that pristine HKUST-1 without Pt nanoparticles retained its microstructure and copper element in HKUST-1 remained as divalent state after being subjected to H_2 treatment at 150°C, while a large part of Pt-HKUST-1 structure collapsed and part of divalent copper Cu^{2+} in HKUST-1 was reduced to metallic copper Cu^0. This indicates that HKUST-1 is not stable in the presence of dissociated hydrogen generated by hydrogen spillover, although HKUST-1 showed good resistance to dihydrogen atmosphere. This is because dissociated hydrogen with an unshared electron are much more reactive and thus a much more effective reducing agent than dihydrogen molecules. Dissociated hydrogen can easily attack and break the coordinated bonding between Cu and O, which led to the reduction of divalent copper element.

To confirm that the severe structural loss of Pt-HKUST-1 was caused by the dissociated hydrogen rather than the heating in inert gas (i.e. that Pt-HKUST-1 is thermally stable at 150°C) , Pt-HKUST-1 was heated at 150°C for 16 hrs in N_2 instead of

H_2. As shown in Figures 31 and 32, no new peak appeared in the XRD pattern of Pt-HKUST-1 and the valence state of Cu in Pt-HKUST-1 remained unchanged after the treatment in N_2 at 150°C. The surface area of Pt-HKUST-1 remained at 960 m^2/g.

To further investigate the temperature effects on hydrogen spillover and the stabilities of MOFs, Pt-doped HKUST-1 samples were treated at various temperatures and the XRD patterns of the treated samples in the range of 41-50° in 2θ were displayed in Figure 20 (XRD patterns of samples in full range of 5-60° in 2θ were shown in Figure 30).

Compared with XRD pattern of Pt-HKU-150, the peak at 43.2° shrunk into a small hump in the XRD pattern of Pt-HKU-100. When H_2 treatment temperatures were lowered to 75, 50 and 25°C, the peak at 43.2° became more unclear in the XRD patterns of Pt-HKU-75, Pt-HKU-50 and Pt-HKU-25. This is reasonable and could be explained by the decreased chemical activities of dissociated hydrogen with temperature decreased. In order to examine the states of Cu elements in these samples, X-ray photoelectron spectroscopy was conducted around the characteristic peak range of copper, 930 to 965 eV, and the corresponding X-ray photoelectron spectra were shown in Figure 21.

As illustrated in Figure 18, pristine HKUST-1 processed in H_2 at 150 and 100°C showed two major characteristic peaks of divalent Cu (Cu^{2+}) at 934.6 and 954.4 eV with a very small, barely noticeable Cu shoulder at 932 eV (Figure 18). This small, barely noticeable Cu shoulder was caused by partial Cu reduction (a very small fraction). However, when Pt-HKUST-1 treated in H_2 at different temperatures for 16 h, two intense, obvious peaks appeared at 932.4 and 952.2 eV, which can be assigned to Cu (0/1+).[113,114] Moreover, the intensity of “shake-up satellites” decreased much as an evidence of the

reduction of divalent copper. One reasonable explanation is that hydrogen molecules chemisorbed and dissociated on the surface of Pt and then spilt over to surface of HKUST-1 and followed by surface diffusion on HKUST-1. The spiltover atomic hydrogen moved to the location of Cu-O coordination bonding and interacted with Cu-O, which led to the formation of lower-valence copper. Meanwhile, the ratio of Cu^{2+} peak area vs. $Cu^{0/+}$ peak area decreased with the treatment temperature being increased, which demonstrates more divalent copper was reduced at higher temperatures, in consistent with the XRD results. Since it is difficult to distinguish between metallic Cu^0 and Cu^+ due to overlap of XPS spectra,[113,114] X-ray-excited Auger Electron Spectroscopy (XAES) of Cu LMM was carried out to distinguish Cu^0 and Cu^+, and Cu LMM XAES spectrum of Pt-HKU-100 as an example is shown in Figure 22. In Figure 22, the peak around kinetic energy 918.6 eV was assigned to be Cu^0, while the peak around 917.5 eV was attributed to Cu^{2+}.[103] As for the peak at 915.0 eV, it is also related with Cu^0, although it is not always useful for chemical state determination.[113]

For clarity, we also compared of XRD, BET Surface area, and XPS of HKUST-1, Pt-HKUST-1, treated HKUST-1 and treated Pt-HKUST-1 (After being subjected to H_2 treatment at 150°C for 16 h) in Table 5, which one can clearly see the huge differences among these untreated and treated MOFs.

This evidence also demonstrated that HKUST-1 tends to be hydrogenated by dissociated hydrogen more than by relatively-stable dihydrogen molecules, since divalent copper in HKUST-1 remained intact in H_2 at 150 and 100°C for 16 hours while part of Cu^{2+} in Pt-HKUST-1 was reduced to Cu^0 in the presence of dissociated hydrogen at 100°C.

Stabilities of MIL-53 were also examined by the same approaches. XRD patterns of MIL-53 samples before and after H_2 treatment at 150°C (MIL-53 and MIL-53-150), Pt-doped MIL-53 samples before and after H_2 treatment (Pt-MIL-53 and Pt-MIL-53-150) are shown in Figure 23.

The XRD pattern of pristine MIL-53 in Figure 23 is in good agreement with previous reports.[115,116] After being treated in H_2 at 150°C for 16 h, no change was observed in XRD pattern of MIL-53-150, which demonstrated MIL-53 has good resistance towards H_2 under such a condition. After Pt-doping process, the peak intensity of MIL-53 decreased slightly, probably due to the pore blocking of MIL-53 by Pt nanoparticles. However, unlike Pt-HKUST-1, Pt-MIL-53 showed good stability and maintained crystalline integrity with dissociated hydrogen after being exposed in H_2 environment at 150°C for 16 hours, which was verified from the unaltered XRD pattern of Pt-MIL-53-150. Further tests of the states of aluminum elements in MIL-53, MIL-53-150 and Pt-MIL-53-150 conducted by XPS around Al 2s peak are shown in Figure 24.

In Figure 24, typical Al 2s peaks at 191.2 eV were observed for pristine MIL-53, which is the characteristic peak of Al^{3+}.[117,118] Although small changes of FWHM (full width at half maximum) appeared, no peak shift for Al 2s was observed on MIL-53-150 and Pt-MIL-53-150, which demonstrates the state of aluminum elements in MIL-53 remain intact and reconfirmed our conclusion from XRD patterns that MIL-53 exhibited good stability in both dihydrogen and dissociated hydrogen environments at elevated temperatures. This is reasonable because Al possesses a much lower reduction potential than hydrogen.

Stabilities of ZIF-8 samples were also studied in dihydrogen and dissociated hydrogen environments. XRD patterns of ZIF-8 samples before and after H_2 treatment at 150°C (ZIF-8 and ZIF-8-150) and Pt-doped ZIF-8 samples before and after H_2 treatment (Pt- ZIF-8 and Pt- ZIF-8-150) are shown in Figure 25.

In Figure 25, pristine ZIF-8 consists of a body-centered cubic (BCC) crystal lattice with reflections of (011), (002), (112), (022), (013), (222), (233) and (134) planes at 2θ=7.4°, 10.4°, 12.8°, 14.7°, 16.5°, 18.1°, 24.6° and 26.7°, respectively.[83,119] After being exposed in H_2 at 150°C for 16 hours, there was no peak change observed for ZIF-8-150, which demonstrated ZIF-8 also has a good stability in dihydrogen environment. XRD results also illustrated further doping Pt nanoparticles on ZIF-8 did not cause any structure alternation. Moreover, Pt-doped ZIF-8 still remained crystalline integrity after being treated in H_2 at 150°C for 16 hours, which manifests ZIF-8 is stable in both dihydrogen and dissociated hydrogen at elevated temperatures. XPS measurements were also performed to verify the states of Zn elements in ZIF-8, ZIF-8-150, Pt-ZIF-8-150, which were shown in Figure 26.

As shown in Figure 26, two characteristic peaks of Zn were observed in the XPS spectra of pristine ZIF-8, where are at 1021.4 and 1044.5 eV corresponding to Zn $2p_{3/2}$ and Zn $2p_{1/2}$ respectively.[120-122] Since it's difficult to distinguish the oxidation states of Zn by only using Zn 2p spectra due to the overlap of binding energy range of Zn^0 and Zn^{2+},[122] Zn LMM Auger spectra were carried out to determine the chemical states of Zn and the results were shown in Figure 27.

After being treated in H_2 at 150°C for 16 hours, no peak shifts were observed on both ZIF-8-150 and Pt-ZIF-8-150 in Figure 26 and Figure 27, which confirms the valence

states of Zn elements in ZIF-8 samples remained intact in the presence of H_2 and dissociated hydrogen. This is in good agreement with XRD results. This phenomenon could also be explained by the lower reduction potential of Zn than hydrogen, which means hydrogen cannot reduce the divalent Zn.

It is noted that Zn in ZIF-8 has no open coordination sites. The open metal sites are known to interact more strongly with adsorbate molecules than saturated metal sites. To see if the open sites affect the stability, Zn-MOF-74 with the open Zn sites was treated under the same conditions of ZIF-8. As shown in Figure 33 and 34, the open Zn sites in Zn-MOF-74 could not be reduced by hydrogen.

The synthesis procedure of Zn-MOF-74 is summarized here, which is similar to previous reports.[18,123,124] 2,5-Dihydroxybenzene-1,4-dicarboxylic acid (0.2g, Sigma-Aldrich) and zinc nitrate hexahydrate (0.91g, Sigma-Aldrich) were dissolved in 40 mL of N,N-dimethylformamide (Sigma-Aldrich) with stirring in a 80 ml wide mouth glass jar. After dissolution of the reagents, 2 mL of deionized water was added. The jar was tightly capped and placed in an 100 °C oven for 20 h to yield trigonal block crystals. After decanting the hot mother liquor and rinsing with DMF, the product was immersed in methanol (Sigma-Aldrich) for 6 d, during which the activation solvent was decanted and freshly replenished three times. The solvent was removed under vacuum at 270 °C, yielding the porous material. Pt doped Zn-MOF-74 was synthesized by the similar procedure with other Pt doped MOFs described above.

Based on the XRD and XPS results, it could be concluded that the stabilities of MOFs in the presence of H_2 or dissociated hydrogen are related with the reduction potentials of metal elements in MOFs. For metal elements like Zn or Al possessing much

lower reduction potentials (-0.76 and -1.66 V, respectively) compared with hydrogen[125,126], they could retain original valence states after contact with H_2 or dissociated hydrogen even at elevated temperatures. But for the MOFs with metal elements like Cu, which has a slightly higher reduction potential (+0.34 V) compared with hydrogen[127], they can basically remain intact in dihydrogen molecules environment but they would lose structure when exposed to the more reactive dissociated hydrogen. The degree of hydrogenation is also related with temperature. More structural loss was observed at higher temperatures in the presence of dissociated hydrogen, as shown in the XRD patterns of Pt-HKUST-1 processed at different temperatures.

One important factor affecting the hydrogen spillover is the contact between dissociation metals and receptors.[128,129] More intimate contacts between the metal and carbon lead to a lower energy barrier for the spillover of dissociated hydrogen from Pt to carbon.[129] As shown above, Pt-HKUST-1 would lose part of crystalline integrity after contact with hydrogen atoms at elevated temperatures. Thus, the effect of contact on hydrogen spillover could be evaluated by the degree of collapse in the crystal structure of Pt-HKUST-1 via two different synthesis method, incipient wetness doping and organometallic chemical vapor deposition.

Powder X-ray diffraction patterns of pristine HKUST-1 and Pt-HKU-CVD are shown in Figure 28. As shown in Figure 28, the crystal structure of pristine HKUST-1 severely collapsed after doping and reducing Pt-precursor by CVD method. Most characteristic peaks of pristine HKUST-1 disappeared during the CVD doping process. Moreover, a pronounced peak at $2\theta = 43.2°$ emerged, which is the characteristic peak of Cu^0 species at (111) plane.[109-112] This demonstrates that the majority part of divalent Cu

in HKUST-1 was reduced to metallic Cu^0 by spiltover dissociated hydrogen generated on the surface of Pt in the CVD reduction process. The severe collapse was confirmed by BET measurements, which showed the surface area of treated Pt-HKU-CVD dropped dramatically from 1150 to 15 m^2/g.

In Figure 19, part of Pt-HKUST-1 structure exhibited peak variance, since the positions of most peaks remained intact in XRD patterns while the XRD intensity and BET surface area decreased less substantially compared with Pt-HKU-CVD. This is a distinct proof that contact between metals and receptors plays an important role in hydrogen spillover. To synthesize Pt-HKU-CVD, Pt was first doped on HKUST-1 by vapor deposition of a volatile platinum precursor (trimethyl)-methylcyclopentadienyl platinum (IV), then Pt organo-precursor decomposed and was reduced by H_2 into metallic Pt on the surface of HKUST-1. Because of the in-situ reduction and growth of metallic Pt on the surface of HKUST-1 framework, the contact between Pt nanoparticles and HKUST-1 receptor is much more intimate than the doping of colloidal Pt nanoparticles on HKUST-1 via incipient wetness. Thus, it facilitated the migration of dissociated hydrogen from Pt surface to HKUST-1 framework surface and subsequently caused more severe hydrogenation of HKUST-1 framework due to more Cu-O bonding breaking in the presence of more migrated dissociated hydrogen. Meanwhile, the XRD pattern of Pt-HKU-CVD also supports our conclusion that HKUST-1 is not stable in contact with dissociated hydrogen at elevated temperatures. It is worth noting that our previous results showed the crystal structures of Pt-doped IRMOF-8 (Zn cluster) prepared via the same CVD method remained intact.[78] The stability difference between Pt-HKU-CVD and Pt-IRMOF-8-CVD also confirms that the metal cluster in MOFs is a key factor influencing

the stability of MOFs in the presence of dissociated hydrogen due to different reduction potentials of different metal elements.

We also measured the hydrogen uptakes on HKUST-1, untreated/fresh Pt-HKUST-1 (never seen hydrogen before the measurement), treated Pt-HKUST-1 (treated in H_2 at 150°C for 16h). As shown in Figure 35, hydrogen uptake on fresh Pt-HKUST-1 was 1.5 times that on HKUST-1. The 50% enhancement on fresh Pt-HKUST-1 was contributed by hydrogen adsorption on Pt and spiltover hydrogen adsorption on HKUST-1. Note that hydrogen uptake on treated Pt-HKUST-1 was much less than that on fresh Pt-HKUST-1. This is because Pt-HKUST-1 degraded after being treated in H_2 at 150°C for 16h and the surface area was reduced from 960 m^2/g (untreated Pt-HKUST-1) to 151 m^2/g (treated Pt-HKUST-1). It is interesting to note that hydrogen uptake on treated Pt-HKUST-1 was almost the same as that on HKUST-1, although the huge differences in their surface area, 151 m^2/g for treated Pt-HKUST-1 and 1150 m^2/g for HKUST-1. Obviously, the spillover enhancement on treated Pt-HKUST-1 offset the loss of hydrogen uptake by its low surface area. These results also indicated the hydrogen spillover occurred on Pt-HKUST-1.

Note that, as shown in Table 5, the huge differences between treated HKUST-1 and treated Pt-HKUST-1 were caused by the much higher activity of dissociated H than H_2 molecules. We conclude that reduction potential determines whether a metal can be reduced by hydrogen, and the forms of hydrogen, dissociated H atom or hydrogen molecules affected how much/fast the Cu in HKUST-1 was reduced. That is why a very small, barely noticeable Cu^0 shoulder at 932 eV was observed in Cu 2p XPS of HKU-100 and HKU-150 (meaning a very small fraction of Cu was reduced), and two intense, major

peaks at 932.4 and 952.2 eV, assigned to Cu (0/1+), were observed on Pt-HKUST-1 (meaning Cu in Pt-HKUST-1 was most/fast reduced). We emphasize that it is not "Pt speeding up kinetics of degradation" but the H atom dissociated by Pt caused the strong degradation of Pt-HKUST-1. If the degradation of Pt-HKUST-1 was caused by Pt not H, the other three MOFs doped with Pt should have shown degradation, but they did not. Also the XPS results have confirmed the severe reduction of Cu (intense, obvious Cu^0 peak at 932 eV) in Pt-HKUST-1 (Cu can be reduced by H not by Pt), which consequently led to the reduced surface area of Pt-HKUST-1.

Conclusions

In this work, a series of Pt-doped HKUST-1, MIL-53 and ZIF-8 samples were synthesized via colloidal nanoparticles incipient wetness impregnation and CVD method. Their stabilities in the presence of dihyrogen molecules and dissociated hydrogen were examined by XRD and XPS measurements. Al-based and Zn-based frameworks exhibited good stabilities in both dihydrogen molecules and dissociated hydrogen environments at elevated temperatures (up to 150°C). The structure of Cu-based framework HKUST-1 remained intact in dihydrogen environment but the structure of the Pt-doped HKUST-1 began to collapse upon exposure to H_2, as a result of spillover of the dissociated hydrogen. The degree of collapse increased with temperature. The stabilities of MOFs with different metal clusters in H_2 and dissociated hydrogen environments are related to the different reduction potentials of the metal elements. A further comparison of the stabilities of MOF-74 (with open coordination sites) and ZIF-8 (without open coordination sites) confirmed that the stability of MOF was related to reduction potential of metal in MOF not the presence/absence of open sites. This work provides useful

information for future optimization of MOFs as hydrogen storage candidate materials, which should have good stabilities in the presence of H_2 or dissociated hydrogen at ambient as well as elevated temperatures. Moreover, significant difference in stabilities between Pt-HKU-CVD and Pt-HKU (via. incipient wetness) showed that the contacts between Pt metal and the framework played an important role in hydrogen spillover.

Acknowledgement

This work was supported by Ford University Research Program from Ford Motor Company and NSF grant CBET-0753008.

Note

The contents of this chapter have been published in J. Phys. Chem. C 2013, 117, 7565.

References:

(1) Schlapbach, L.; Zuttel, A. *Nature* **2001**, *414*, 353.
(2) Office of Power Delivery;Office of Power Technologies;Energy Efficiency and Renewable Energy;Department of Energy;Washington, D. *A Multiyear Plan for the Hydrogen R&D Program* **1999**.
(3) Dillon, A. C.; Jones, K. M.; Bekkedahl, T. A.; Kiang, C. H.; Bethune, D. S.; Heben, M. J. *Nature* **1997**, *386*, 377.
(4) Choi, M.; Ryoo, R. *Journal of Materials Chemistry* **2007**, *17*, 4204.
(5) Chen, H.; Yang, R. T. *Langmuir* **2010**, *26*, 15394.
(6) Nishihara, H.; Hou, P. X.; Li, L. X.; Ito, M.; Uchiyama, M.; Kaburagi, T.; Ikura, A.; Katamura, J.; Kawarada, T.; Mizuuchi, K.; Kyotani, T. *Journal of Physical Chemistry C* **2009**, *113*, 3189.
(7) Langmi, H. W.; Book, D.; Walton, A.; Johnson, S. R.; Al-Mamouri, M. M.; Speight, J. D.; Edwards, P. P.; Harris, I. R.; Anderson, P. A. *Journal of Alloys and Compounds* **2005**, *404–406*, 637.
(8) Zecchina, A.; Bordiga, S.; Vitillo, J. G.; Ricchiardi, G.; Lamberti, C.; Spoto, G.; Bjørgen, M.; Lillerud, K. P. *Journal of the American Chemical Society* **2005**, *127*, 6361.
(9) Saha, D.; Deng, S. *Langmuir* **2009**, *25*, 12550.
(10) Parambhath, V. B.; Nagar, R.; Ramaprabhu, S. *Langmuir* **2012**, *28*, 7826.
(11) Kaye, S. S.; Dailly, A.; Yaghi, O. M.; Long, J. R. *Journal of the American Chemical Society* **2007**, *129*, 14176.
(12) Murray, L. J.; Dinca, M.; Long, J. R. *Chem. Soc. Rev.* **2009**, *38*, 1294.
(13) Dincă, M.; Dailly, A.; Liu, Y.; Brown, C. M.; Neumann, D. A.; Long, J. R. *Journal of the American Chemical Society* **2006**, *128*, 16876.
(14) Ma, S.; Zhou, H. C. *Journal of the American Chemical Society* **2006**, *128*, 11734.
(15) Ma, S. Q.; Sun, D. F.; Ambrogio, M.; Fillinger, J. A.; Parkin, S.; Zhou, H. C. *Journal of the American Chemical Society* **2007**, *129*, 1858.
(16) Collins, D. J.; Zhou, H. C. *J. Mater. Chem.* **2007**, *30*, 3154.
(17) Chae, H.; Siberio-Perez, D. Y.; Kim, J.; Go, Y.; Eddaoudi, M.; Matzger, A.; O'Keeffe, M.; Yaghi, O. M. *Nature* **2004**, *427*, 523.
(18) Rowsell, J. L. C.; Yaghi, O. M. *Journal of the American Chemical Society* **2006**, *128*, 1304.
(19) Frost, H.; Snurr, R. Q. *The Journal of Physical Chemistry C* **2007**, *111*, 18794.
(20) Keskin, S.; Liu, J.; Rankin, R. B.; Johnson, J. K.; Sholl, D. S. *Industrial & Engineering Chemistry Research* **2008**, *48*, 2355.
(21) Watanabe, T.; Sholl, D. S. *Journal of Chemical Physics* **2010**, *133*.
(22) Walton, K. S.; Snurr, R. Q. *Journal of the American Chemical Society* **2007**, *129*, 8552.
(23) Cai, Y.; Zhang, Y.; Huang, Y.; Marder, S. R.; Walton, K. S. *Crystal Growth & Design* **2012**, *12*, 3709.
(24) Mu, B.; Schoenecker, P. M.; Walton, K. S. *The Journal of Physical Chemistry C* **2010**, *114*, 6464.
(25) Park, H. J.; Suh, M. P. *Chemical Communications* **2012**, *48*, 3400.
(26) Prasad, T. K.; Suh, M. P. *Chemistry-a European Journal* **2012**, *18*, 8673.
(27) Park, H. J.; Suh, M. P. *Chemical Communications* **2010**, *46*, 610.

(28) Prasad, T. K.; Hong, D. H.; Suh, M. P. *Chemistry-a European Journal* **2010**, *16*, 14043.
(29) Latroche, M.; Surblé, S.; Serre, C.; Mellot-Draznieks, C.; Llewellyn, P. L.; Lee, J. H.; Chang, J. S.; Jhung, S. H.; Férey, G. *Angew. Chem., Int. Ed.* **2006**, *45*, 8227.
(30) Furukawa, H.; Miller, M.; Yaghi, O. M. *J. Mater. Chem.* **2007**, *17*, 3197.
(31) Koh, K.; Wong-Foy, A. G.; Matzger, A. J. *Journal of the American Chemical Society* **2009**, *131*, 4184.
(32) Furukawa, H.; Ko, N.; Go, Y. B.; Aratani, N.; Choi, S. B.; Choi, E.; Yazaydin, A. Ö.; Snurr, R. Q.; O'Keeffe, M.; Kim, J.; Yaghi, O. M. *Science* **2010**, *329*, 424.
(33) Farha, O. K.; Özgür Yazaydın, A.; Eryazici, I.; Malliakas, C. D.; Hauser, B. G.; Kanatzidis, M. G.; Nguyen, S. T.; Snurr, R. Q.; Hupp, J. T. *Nat Chem* **2010**, *2*, 944.
(34) Farha, O. K.; Eryazici, I.; Jeong, N. C.; Hauser, B. G.; Wilmer, C. E.; Sarjeant, A. A.; Snurr, R. Q.; Nguyen, S. T.; Yazaydin, A. O.; Hupp, J. T. *Journal of the American Chemical Society* **2012**, *134*, 15016.
(35) Robell, A. J.; Ballou, E. V.; Boudart, M. *J. Phys. Chem.* **1964**, *68*, 2748.
(36) Srinivas, S. T.; Rao, P. K. *Journal of Catalysis* **1994**, *148*, 470.
(37) Conner, W. C.; Falconer, J. L. *Chemical Reviews* **1995**, *95*, 759.
(38) Pajonk, G. M. *Appl. Catal., A* **2000**, *202*, 157.
(39) Wang, L.; Yang, R. T. *Catalysis Reviews* **2010**, *52*, 411.
(40) Sinfelt, J. H.; Lucchesi, P. J. *J. Am. Chem. Soc.* **1963**, *85*, 3365.
(41) Khoobiar, S. *J. Phys. Chem.* **1964**, *68*, 411.
(42) Pajonk, G. M.; Teichner, S. *J. Bull. Soc. Chim.* **1971**, 3847.
(43) Benson, J. E.; Kohn, H. W.; Boudart, M. *Journal of Catalysis* **1966**, *5*, 307.
(44) Boudart, M.; Vannice, M. A.; Benson, J. E. *Zeitschrift für Physikalische Chemie* **1969**, *64*, 171.
(45) Sermon, P. A.; Bond, G. C. *Catalysis Reviews* **1974**, *8*, 211.
(46) Mitchell, P. C. H.; Ramirez-Cuesta, A. J.; Parker, S. F.; Tomkinson, J.; Thompsett, D. *J. Phys. Chem. B* **2003**, *107*, 6838.
(47) Mitchell, P. C. H.; Ramirez-Cuesta, A. J.; Parker, S. F.; Tomkinson, J. *J. Mol. Struct.* **2003**, *651−653*, 781.
(48) Tsao, C.-S.; Liu, Y.; Li, M.; Zhang, Y.; Leao, J. B.; Chang, H.-W.; Yu, M.-S.; Chen, S.-H. *The Journal of Physical Chemistry Letters* **2010**, *1*, 1569.
(49) Tsao, C.-S.; Liu, Y.; Chuang, H.-Y.; Tseng, H.-H.; Chen, T.-Y.; Chen, C.-H.; Yu, M.-S.; Li, Q.; Lueking, A.; Chen, S.-H. *The Journal of Physical Chemistry Letters* **2011**, *2*, 2322.
(50) Bhowmick, R.; Rajasekaran, S.; Friebel, D.; Beasley, C.; Jiao, L.; Ogasawara, H.; Dai, H.; Clemens, B.; Nilsson, A. *Journal of the American Chemical Society* **2011**, *133*, 5580.
(51) Zhan, D. P.; Velmurugan, J.; Mirkin, M. V. *Journal of the American Chemical Society* **2009**, *131*, 14756.
(52) Panayotov, D. A.; Yates, J. T. *Journal of Physical Chemistry C* **2007**, *111*, 2959.
(53) Panayotov, D. A.; Burrows, S. P.; Yates, J. T.; Morris, J. R. *The Journal of Physical Chemistry C* **2011**, *115*, 22400.
(54) Chen, L.; Cooper, A. C.; Pez, G. P.; Cheng, H. *Journal of Physical Chemistry C* **2007**, *111*, 18995.

(55) Sha, X. W.; Knippenberg, M. T.; Cooper, A. C.; Pez, G. P.; Cheng, H. S. *Journal of Physical Chemistry C* **2008**, *112*, 17465.
(56) Singh, A. K.; Ribas, M. A.; Yakobson, B. I. *Acs Nano* **2009**, *3*, 1657.
(57) Lin, Y.; Ding, F.; Yakobson, B. I. *Phys. Rev. B: Condens. Matter.* **2008**, *78*, 041402.
(58) Lee, K.; Kim, Y.-H.; Sun, Y. Y.; West, D.; Zhao, Y.; Chen, Z.; Zhang, S. B. *Physical Review Letters* **2010**, *104*, 236101.
(59) Tsao, C. S.; Yu, M. S.; Wang, C. Y.; Liao, P. Y.; Chen, H. L.; Jeng, U. S.; Tzeng, Y. R.; Chung, T. Y.; Wut, H. C. *Journal of the American Chemical Society* **2009**, *131*, 1404.
(60) Miller, M. A.; Wang, C. Y.; Merrill, G. N. *Journal of Physical Chemistry C* **2009**, *113*, 3222.
(61) Li, Y.; Yang, F. H.; Yang, R. T. *The Journal of Physical Chemistry C* **2007**, *111*, 3405.
(62) Cao, W.; Li, Y.; Wang, L.; Liao, S. *The Journal of Physical Chemistry C* **2011**, *115*, 13829.
(63) Suri, M.; Dornfeld, M.; Ganz, E. *J. Chem. Phys.* **2009**, *131*, 174703.
(64) Ganz, E.; Dornfeld, M. *The Journal of Physical Chemistry C* **2012**, *116*, 3661.
(65) Psofogiannakis, G. M.; Froudakis, G. E. *The Journal of Physical Chemistry C* **2011**, *115*, 4047.
(66) Li, Y.; Yang, R. T. *Journal of the American Chemical Society* **2006**, *128*, 8136.
(67) Wang, C.-Y.; Tsao, C.-S.; Yu, M.-S.; Liao, P.-Y.; Chung, T.-Y.; Wu, H.-C.; Miller, M. A.; Tzeng, Y.-R. *Journal of Alloys and Compounds* **2010**, *492*, 88.
(68) Stuckert, N. R.; Wang, L.; Yang, R. T. *Langmuir* **2010**, *26*, 11963.
(69) Anbia, M.; Mandegarzad, S. *Journal of Alloys and Compounds* **2012**, *532*, 61.
(70) Lin, K.-S.; Adhikari, A. K.; Chang, K.-C.; Tu, M.-T.; Lu, W. *Catalysis Today* **2011**, *164*, 23.
(71) Yang, S. J.; Choi, J. Y.; Chae, H. K.; Cho, J. H.; Nahm, K. S.; Park, C. R. *Chemistry of Materials* **2009**, *21*, 1893.
(72) Lee, S.-Y.; Park, S.-J. *International Journal of Hydrogen Energy* **2011**, *36*, 8381.
(73) Liu, Y. Y.; Zhang, J.; Zeng, J. L.; Chu, H. L.; Xu, F.; Sun, L. X. *Chin. J. Catal.* **2008**, *29*, 655.
(74) Proch, S.; Herrmannsdorfer, J.; Kempe, R.; Kern, C.; Jess, A.; Seyfarth, L.; Senker, J. *Chemistry* **2008**, *14*, 8204.
(75) Zlotea, C.; Campesi, R.; Cuevas, F.; Leroy, E.; Dibandjo, P.; Volkringer, C.; Loiseau, T.; Ferey, G.; Latroche, M. *Journal of the American Chemical Society* **2010**, *132*, 2991.
(76) Cheon, Y. E.; Suh, M. P. *Angew Chem Int Ed Engl* **2009**, *48*, 2899.
(77) Sabo, M.; Henschel, A.; Frode, H.; Klemm, E.; Kaskel, S. *Journal of Materials Chemistry* **2007**, *17*, 3827.
(78) Wang, L. F.; Stuckert, N. R.; Chen, H.; Yang, R. T. *Journal of Physical Chemistry C* **2011**, *115*, 4793.
(79) Moon, H. R.; Kim, J. H.; Suh, M. P. *Angewandte Chemie-International Edition* **2005**, *44*, 1261.
(80) Suh, M. P.; Moon, H. R.; Lee, E. Y.; Jang, S. Y. *Journal of the American Chemical Society* **2006**, *128*, 4710.

(81) Kalidindi, S. B.; Oh, H.; Hirscher, M.; Esken, D.; Wiktor, C.; Turner, S.; Van Tendeloo, G.; Fischer, R. A. *Chemistry (Weinheim an der Bergstrasse, Germany)* **2012**, *18*, 10848.
(82) Suh, M. P.; Park, H. J.; Prasad, T. K.; Lim, D.-W. *Chemical Reviews* **2011**, *112*, 782.
(83) Park, K. S.; Ni, Z.; Côté, A. P.; Choi, J. Y.; Huang, R.; Uribe-Romo, F. J.; Chae, H. K.; O'Keeffe, M.; Yaghi, O. M. *Proceedings of the National Academy of Sciences* **2006**, *103*, 10186.
(84) Choi, H. J.; Dinca, M.; Dailly, A.; Long, J. R. *Energy & Environmental Science* **2010**, *3*, 117.
(85) Wu, T.; Shen, L.; Luebbers, M.; Hu, C.; Chen, Q.; Ni, Z.; Masel, R. I. *Chemical Communications* **2010**, *46*, 6120.
(86) Han, S. S.; Choi, S.-H.; van Duin, A. C. T. *Chemical Communications* **2010**, *46*, 5713.
(87) Saha, D.; Deng, S. *The Journal of Physical Chemistry Letters* **2009**, *1*, 73.
(88) Saha, D.; Deng, S. *J Colloid Interface Sci* **2010**, *348*, 615.
(89) Kang, I. J.; Khan, N. A.; Haque, E.; Jhung, S. H. *Chemistry – A European Journal* **2011**, *17*, 6437.
(90) Schoenecker, P. M.; Carson, C. G.; Jasuja, H.; Flemming, C. J. J.; Walton, K. S. *Industrial & Engineering Chemistry Research* **2012**, *51*, 6513.
(91) Mu, B.; Walton, K. S. *The Journal of Physical Chemistry C* **2011**, *115*, 22748.
(92) Liu, X. M.; Rather, S.-u.; Li, Q.; Lueking, A.; Zhao, Y.; Li, J. *The Journal of Physical Chemistry C* **2011**, *116*, 3477.
(93) Li, Y.; Yang, R. T. *AIChE Journal* **2008**, *54*, 269.
(94) Chui, S. S. *Science* **1999**, *283*, 1148.
(95) Rioux, R. M.; Song, H.; Hoefelmeyer, J. D.; Yang, P.; Somorjai, G. A. *Journal of Physical Chemistry B* **2005**, *109*, 2192.
(96) Navin, J. K.; Grass, M. E.; Somorjai, G. A.; Marsh, A. L. *Analytical Chemistry* **2009**, *81*, 6295.
(97) Wang, Y.; Ren, J. W.; Deng, K.; Gui, L. L.; Tang, Y. Q. *Chemistry of Materials* **2000**, *12*, 1622.
(98) Wang, L.; Stuckert, N. R.; Chen, H.; Yang, R. T. *The Journal of Physical Chemistry C* **2011**, *115*, 4793.
(99) Carbonell, C.; Imaz, I.; Maspoch, D. *Journal of the American Chemical Society* **2011**, *133*, 2144.
(100) Peng, L.; Zhang, J.; Li, J.; Han, B.; Xue, Z.; Yang, G. *Chemical Communications* **2012**, *48*, 8688.
(101) Hanke, M.; Arslan, H. K.; Bauer, S.; Zybaylo, O.; Christophis, C.; Gliemann, H.; Rosenhahn, A.; Wöll, C. *Langmuir* **2012**, *28*, 6877.
(102) Biesinger, M. C.; Lau, L. W. M.; Gerson, A. R.; Smart, R. S. C. *Applied Surface Science* **2010**, *257*, 887.
(103) Poulston, S.; Parlett, P. M.; Stone, P.; Bowker, M. *Surface and Interface Analysis* **1996**, *24*, 811.
(104) Velásquez, P.; Leinen, D.; Pascual, J.; Ramos-Barrado, J. R.; Grez, P.; Gómez, H.; Schrebler, R.; Del Río, R.; Córdova, R. *The Journal of Physical Chemistry B* **2005**, *109*, 4977.

(105) Kundakovic, L.; Flytzani-Stephanopoulos, M. *Applied Catalysis A: General* **1998**, *171*, 13.
(106) Otamiri, J. C.; Andersson, S. L. T.; Andersson, A. *Applied Catalysis* **1990**, *65*, 159.
(107) Meda, L.; Cerofolini, G. F. *Surface and Interface Analysis* **2004**, *36*, 756.
(108) Laborda, F.; Bolea, E.; Baranguan, M. T.; Castillo, J. R. *Spectrochimica Acta Part B: Atomic Spectroscopy* **2002**, *57*, 797.
(109) Zhang, J. Y.; Liu, Y.; Chen, J.; Chen, Y.; Liu, G.; Zhang, X.; Sun, J. *Materials Science and Engineering: A* **2012**, *552*, 392.
(110) Reddy, K. M.; Gledhill, A. D.; Chen, C.-H.; Drexler, J. M.; Padture, N. P. *Applied Physics Letters* **2011**, *98*, 113117.
(111) Hayes, J. R.; Nyce, G. W.; Kuntz, J. D.; Satcher, J. H.; Hamza, A. V. *Nanotechnology* **2007**, *18*, 275602.
(112) Hansen, B. J.; Lu, G.; Chen, J. *Journal of Nanomaterials* **2008**, *2008*, 1.
(113) Zhang, G.; Long, J.; Wang, X.; Dai, W.; Li, Z.; Wu, L.; Fu, X. *New Journal of Chemistry* **2009**, *33*, 2044.
(114) Chusuei, C. C.; Brookshier, M. A.; Goodman, D. W. *Langmuir* **1999**, *15*, 2806.
(115) Loiseau, T.; Serre, C.; Huguenard, C.; Fink, G.; Taulelle, F.; Henry, M.; Bataille, T.; Férey, G. *Chemistry – A European Journal* **2004**, *10*, 1373.
(116) Kubo, M.; Shimojima, A.; Okubo, T. *The Journal of Physical Chemistry C* **2012**, *116*, 10260.
(117) Rastomjee, C. S.; Keil, M.; Sotobayashi, H.; Bradshaw, A. M.; Lamont, C. L. A.; Gador, D.; Umbach, E. *Applied Surface Science* **1998**, *136*, 280.
(118) Sygellou, L.; Gianneta, V.; Xanthopoulos, N.; Skarlatos, D.; Georga, S.; Krontiras, C.; Ladas, S.; Kennou, S. *Surface Science Spectra* **2011**, *18*, 58.
(119) Xie, Z.; Yang, J.; Wang, J.; Bai, J.; Yin, H.; Yuan, B.; Lu, J.; Zhang, Y.; Zhou, L.; Duan, C. *Chemical Communications* **2012**, *48*, 5977.
(120) Lupan, O.; Emelchenko, G. A.; Ursaki, V. V.; Chai, G.; Redkin, A. N.; Gruzintsev, A. N.; Tiginyanu, I. M.; Chow, L.; Ono, L. K.; Roldan Cuenya, B.; Heinrich, H.; Yakimov, E. E. *Materials Research Bulletin* **2010**, *45*, 1026.
(121) Ali, Z.; Cha, S. N.; Sohn, J. I.; Shakir, I.; Yan, C.; Kim, J. M.; Kang, D. J. *Journal of Materials Chemistry* **2012**, *22*, 17625.
(122) Min, Y. S.; An, C. J.; Kim, S. K.; Song, J.; Hwang, C. S. *Bulletin of the Korean Chemical Society* **2010**, *31*, 2503.
(123) Grant Glover, T.; Peterson, G. W.; Schindler, B. J.; Britt, D.; Yaghi, O. *Chemical Engineering Science* **2011**, *66*, 163.
(124) Tranchemontagne, D. J.; Hunt, J. R.; Yaghi, O. M. *Tetrahedron* **2008**, *64*, 8553.
(125) Haynes, W. M.; Lide, D. R.; Bruno, T. J. *CRC Handbook of Chemistry and Physics*; CRC Press, 2012.
(126) Lide, D. R. *CRC Handbook of Chemistry and Physics: A Ready-reference Book of Chemical and Physical Data*; CRC Press, 2006.
(127) Bard, A. J.; Parsons, R.; Jordan, J.; Pure, I. U. o.; Chemistry, A. *Standard Potentials in Aqueous Solution*; M. Dekker, 1985.
(128) Wang, L. F.; Yang, R. T. *Journal of Physical Chemistry C* **2008**, *112*, 12486.
(129) Wang, Z.; Yang, R. T. *The Journal of Physical Chemistry C* **2010**, *114*, 5956.

(130) Dang, T. T.; Zhu, Y.; Ghosh, S. C.; Chen, A.; Chai, C. L. L.; Seayad, A. M. *Chemical Communications* **2012**, *48*, 1805.
(131) Schröder, F.; Esken, D.; Cokoja, M.; van den Berg, M. W. E.; Lebedev, O. I.; Van Tendeloo, G.; Walaszek, B.; Buntkowsky, G.; Limbach, H.-H.; Chaudret, B.; Fischer, R. A. *Journal of the American Chemical Society* **2008**, *130*, 6119.
(132) Sanz, R.; Martinez, F.; Orcajo, G.; Wojtas, L.; Briones, D. *Dalton Transactions* **2013**, *42*, 2392.

Sample	Doped Metal	Doped amount (wt%)	Surface area of pristine MOF (m^2/g)	Surface area of doped MOF (m^2/g)	Reference
MOF-5	Pd	3	718	452[a]	[130]
SNU-3	Pd	3	559	242[b]	76
MIL-100	Pd	10	1200	380[b]	75
IRMOF-8	Pt	4.8	1430	1175[a]	78
MOF-5	Ru	30	3300	860[a]	[131]
MOF-177	Pt	43	5600	867[b]	74
HKUST-1	Pt	5	1150	960[b]	This work

Table 4. Surface area of MOFs before and after metal doping (a) Langmuir surface area (b) BET surface area.

Sample	XRD Intensity	Presence of Cu^0 at 2θ =43.2° in XRD	BET Surface area (m^2/g)	Cu^0 at 932 eV in Cu 2p XPS
HKUST-1	High	No	1150	No
Pt-HKUST-1	High	No	960	No
Treated HKUST-1	Slightly reduced	No	901	Small, barely noticeable shoulder
Treated Pt-HKUST-1	Substantially reduced	Yes	151	Intense and major peak

Table 5. Comparison of XRD, BET Surface area, and XPS of HKUST-1, Pt-HKUST-1, treated HKUST-1 and treated Pt-HKUST-1 (After being subjected to H_2 treatment at 150°C for 16 h)

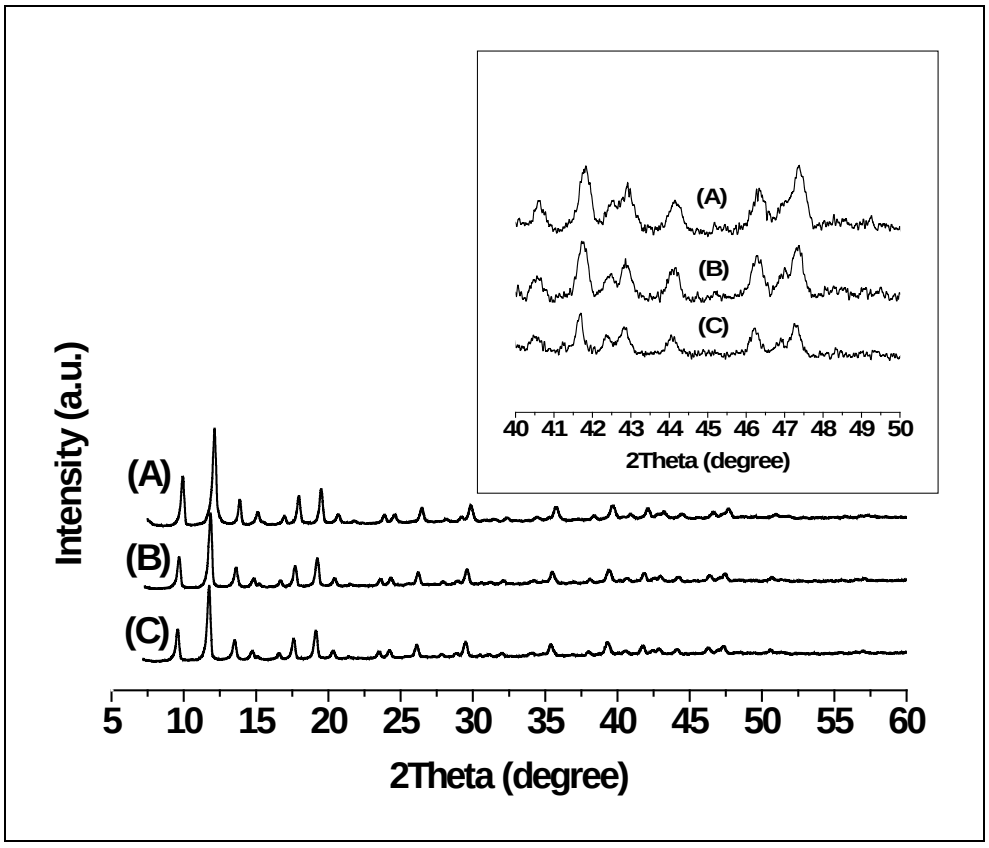

Figure 17. XRD patterns of (A) HKUST-1, (B) HKU-100, (C) HKU-150; inset figure magnifies XRD patterns ranged from 40-50° in 2θ.

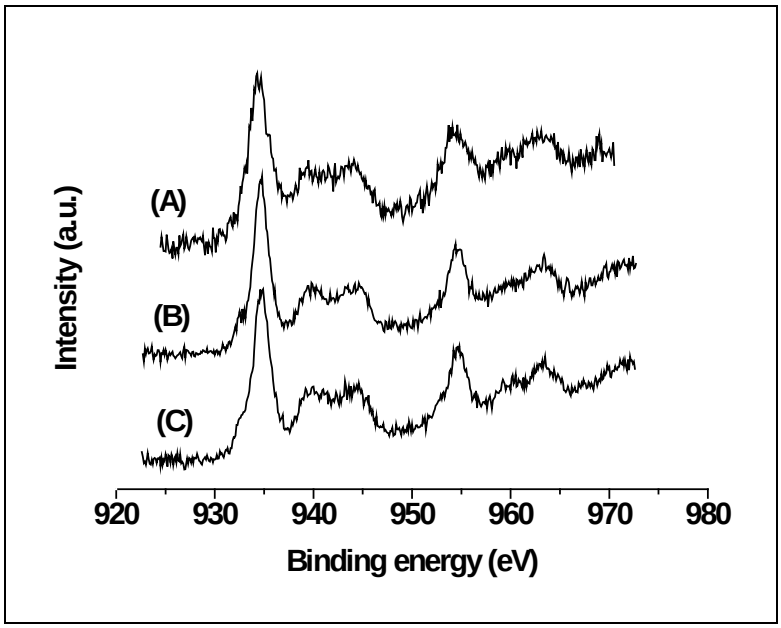

Figure 18. Cu 2p XPS spectra of pristine HKUST-1 and HKUST-1 processed in H_2 at 100°C and 150°C for 16 hours: (A) HKUST-1, (B) HKU-100, (C) HKU-150.

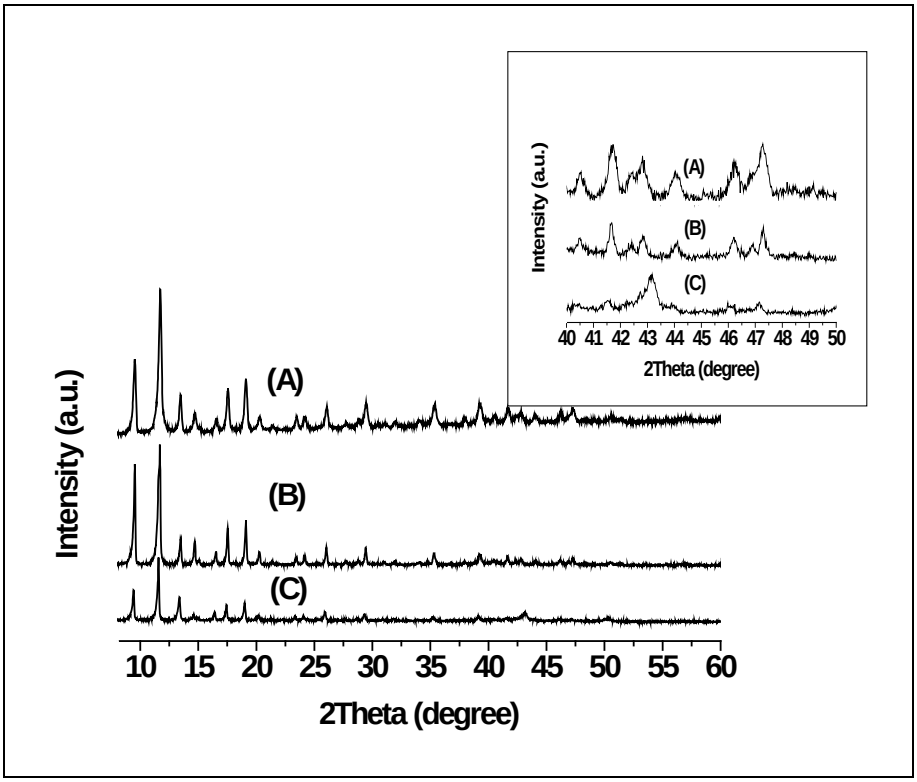

Figure 19. XRD patterns of (A) HKUST-1, (B) Pt-HKUST-1 before H_2 treatment, (C) Pt-HKU-150; inset figure magnifies XRD patterns ranged from 40-50° in 2θ.

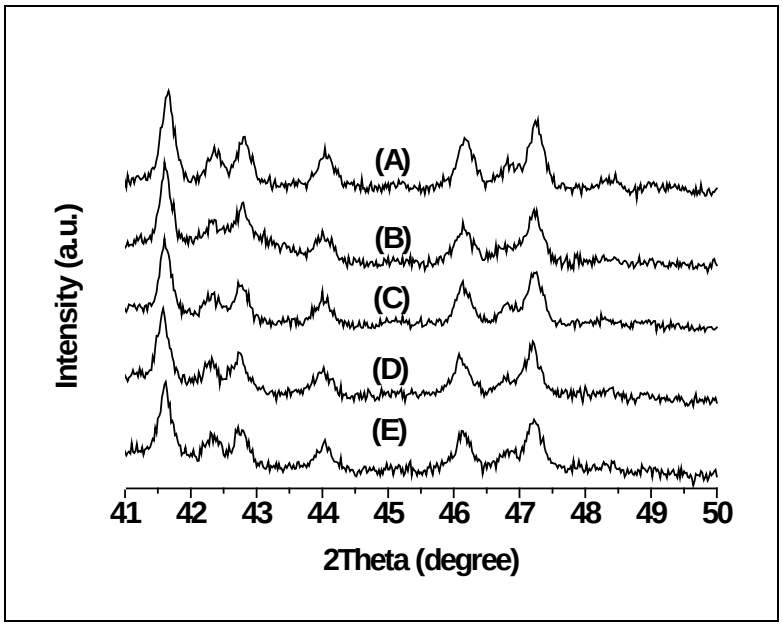

Figure 20. XRD patterns ranged from 41-50° in 2θ for (A) Pt-HKUST-1 before H_2 treatment, (B) Pt-HKU-100, (C) Pt-HKU-75, (D) Pt-HKU-50 and (E) Pt-HKU-25.

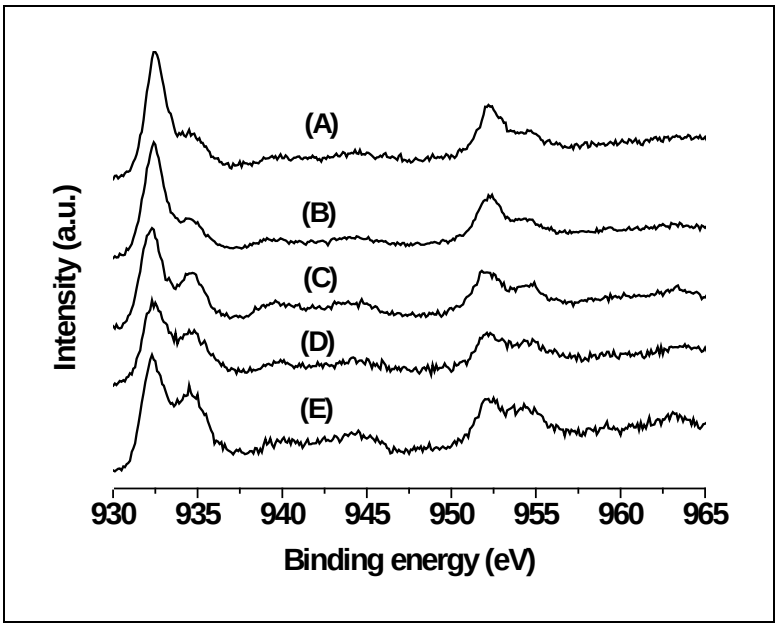

Figure 21. Cu 2p XPS spectra of Pt-HKUST-1 processed in H_2 at 150°C, 100°C, 75°C, 50°C and 25°C for 16 hours: (A) Pt-HKU-150, (B) Pt-HKU-100, (C) Pt-HKU-75, (D) Pt-HKU-50, (E) Pt-HKU-25.

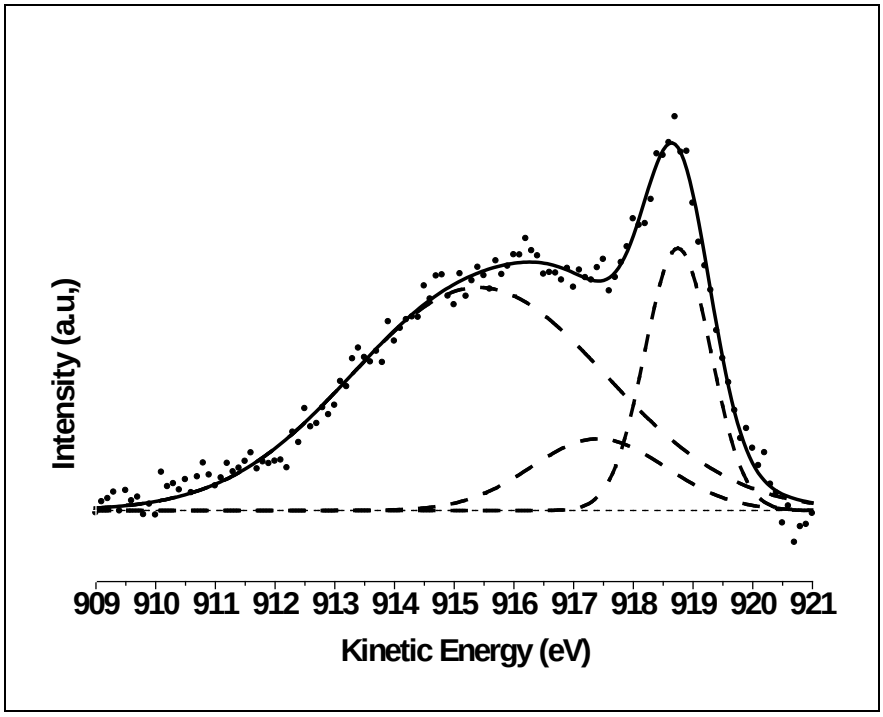

Figure 22. Cu LMM XAES spectrum of Pt-HKU-100

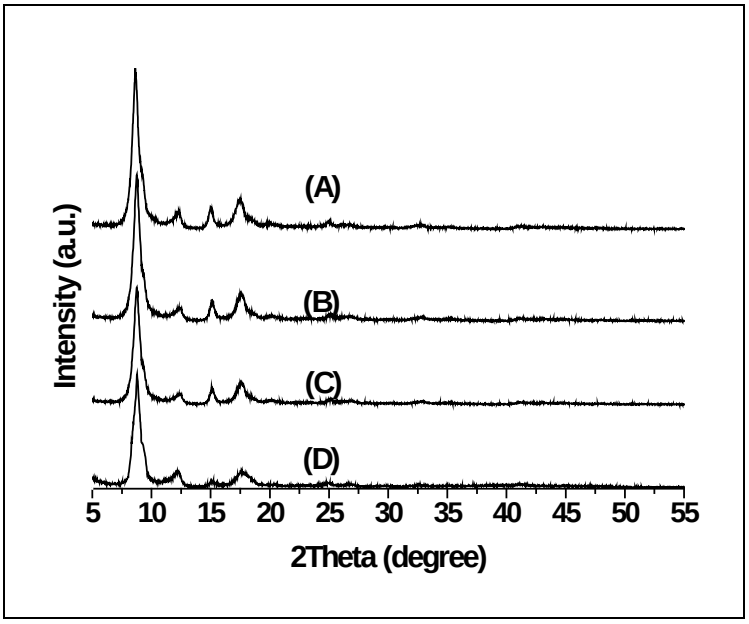

Figure 23. XRD patterns of (A) MIL-53, (B) MIL-53-150, (C) Pt-MIL-53 and (D) Pt-MIL-53-150.

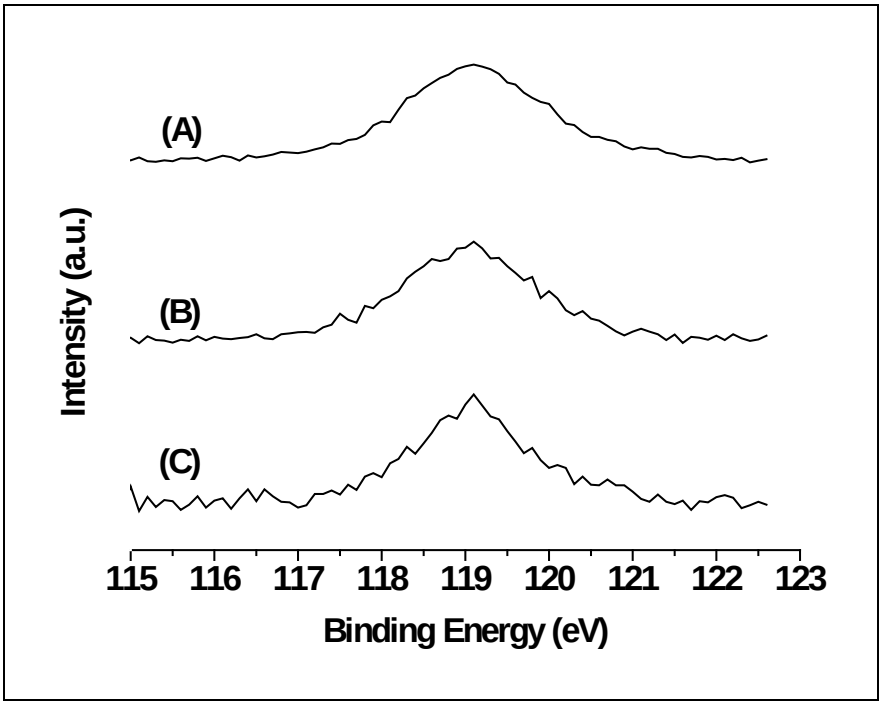

Figure 24. Al 2s XPS spectra of (A) MIL-53, (B) MIL-53-150, (C) Pt-MIL-53-150

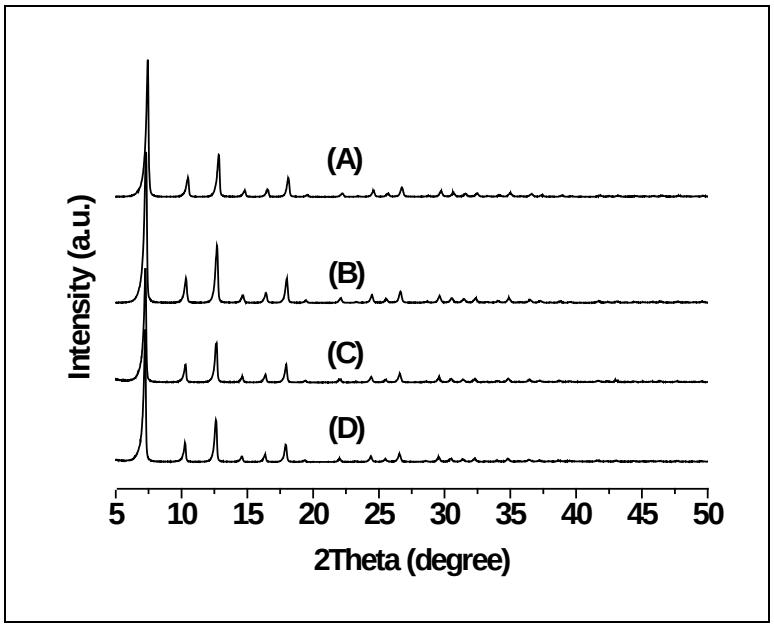

Figure 25. XRD patterns of ZIF-8 samples: (A) ZIF-8, (B) ZIF-8-150, (C) Pt-ZIF-8 and (D) Pt-ZIF-8-150.

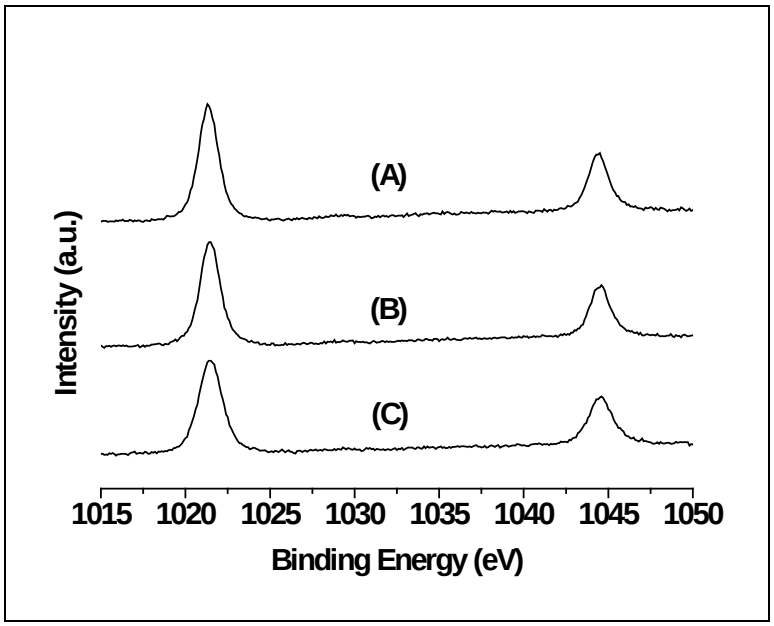

Figure 26. Zn 2p XPS spectra of (A) ZIF-8, (B) ZIF-8-150, (C) Pt-ZIF-8-150

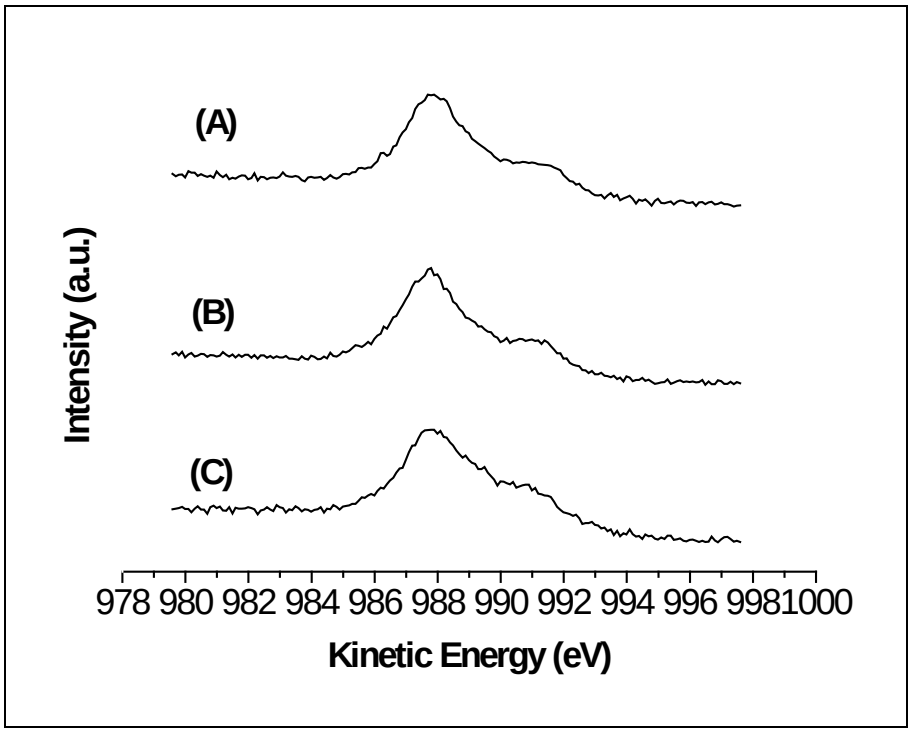

Figure 27. Zn LMM spectra of (A) ZIF-8, (B) ZIF-8-150, (C) Pt-ZIF-8-150

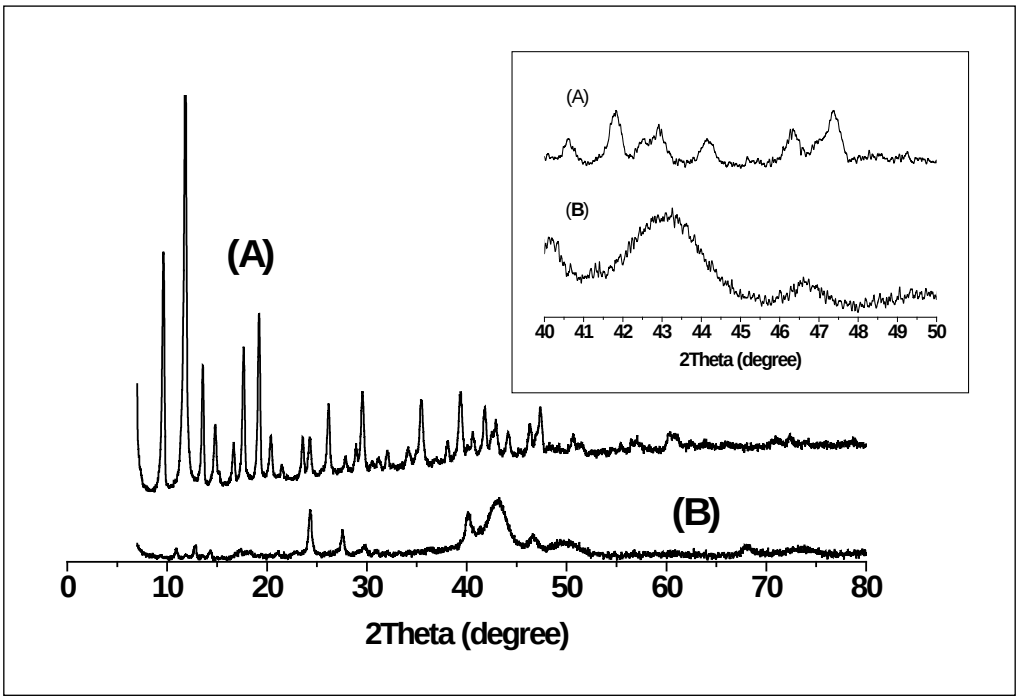

Figure 28. XRD patterns of (A) HKUST-1, (B) Pt-HKU-CVD; inset figure shows XRD patterns of these two samples from 40-50° in 2θ

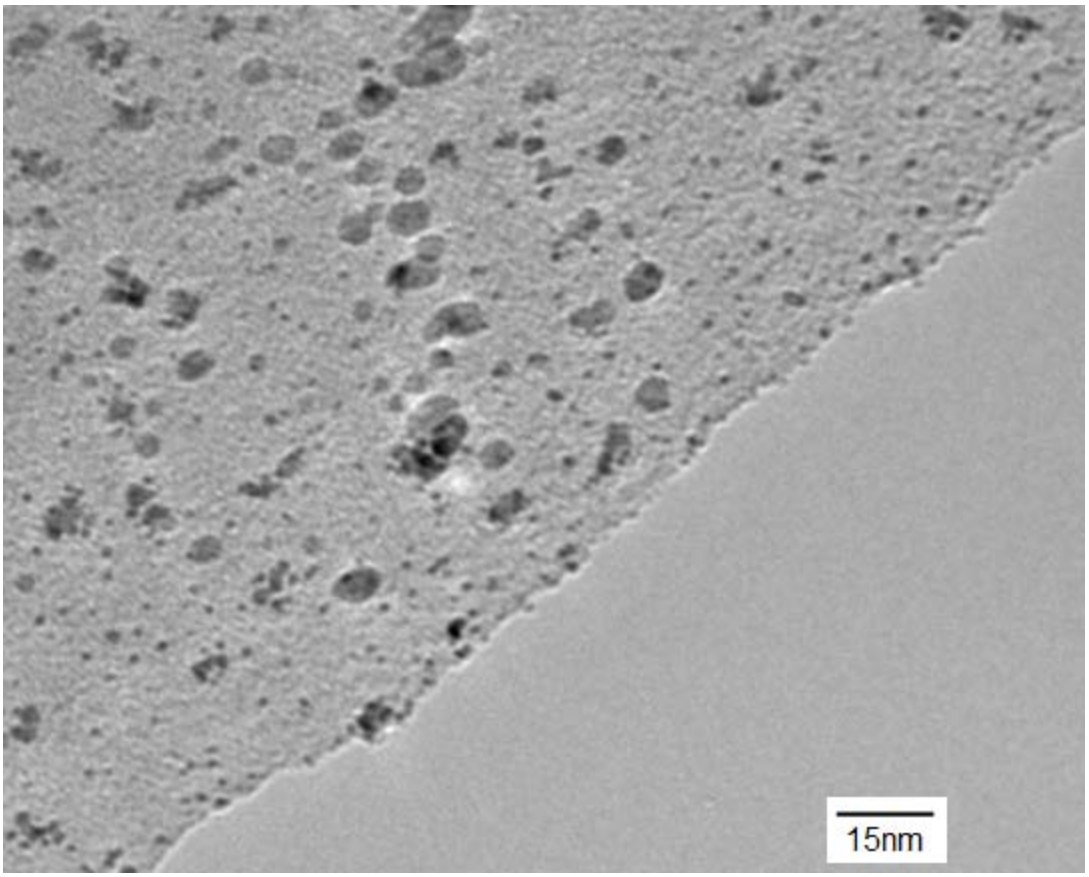

Figure 29. TEM image of Pt doped HKUST-1. The Pt particle sizes are estimated to range from slightly below 1 nm to approximately 10 nm.

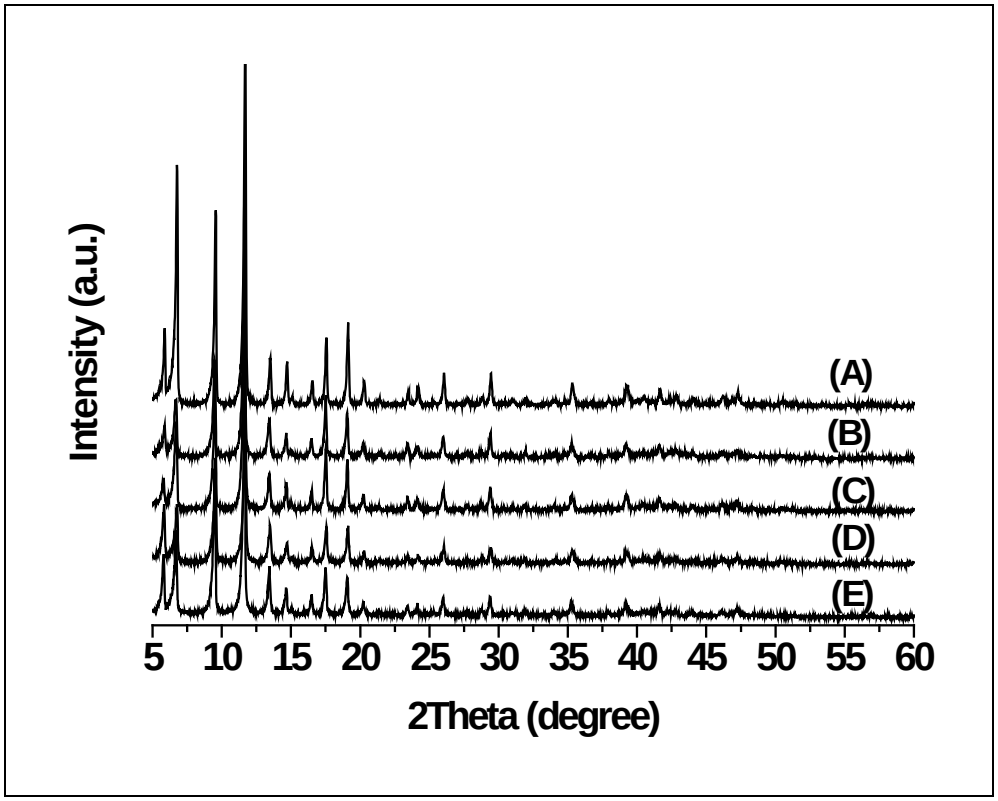

Figure 30. XRD patterns ranged from 5-60° in 2θ for (A) Pt-HKUST-1, (B) Pt-HKUST-100, (C) Pt-HKU-75, (D) Pt-HKU-50 and (E) Pt-HKU-25.

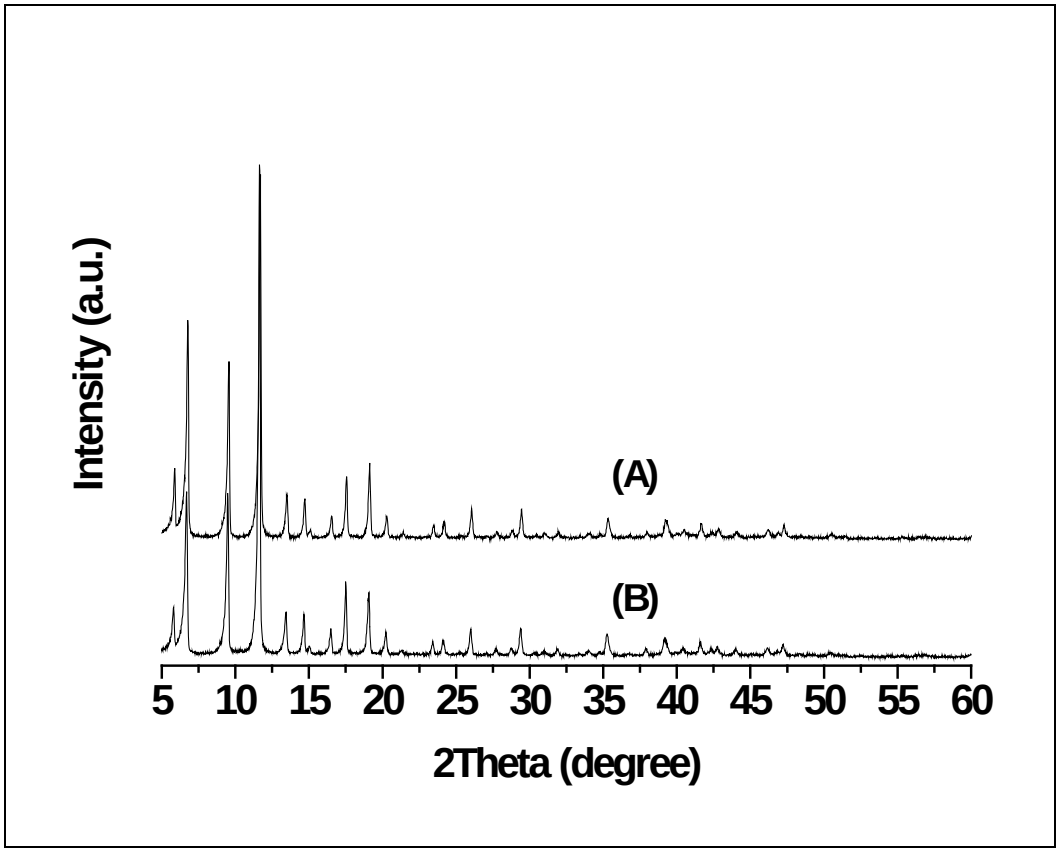

Figure 31. XRD patterns ranged from 5-60° in 2θ for (A) Pt-HKUST-1, (B) Pt-HKUST-1 after N_2 treatment at 150°C for 16 hours.

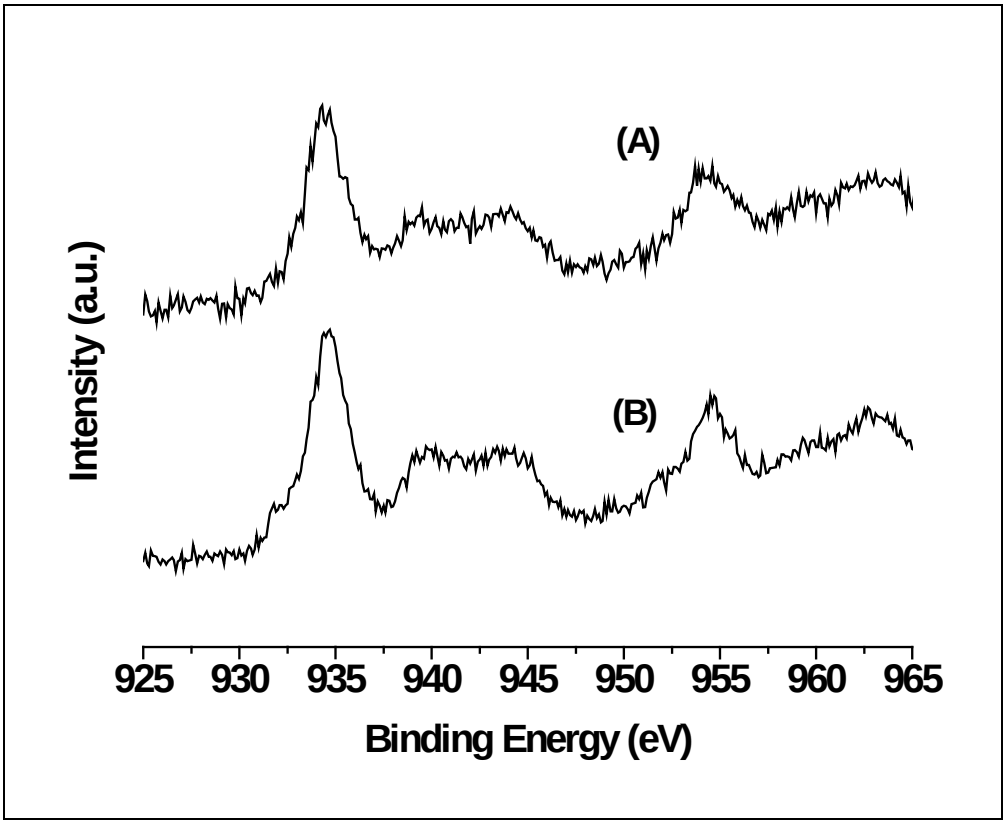

Figure 32. Cu 2p XPS spectra of (A) pristine HKUST-1 and (B) Pt-HKUST-1 after N_2 treatment at 150°C for 16 hours.

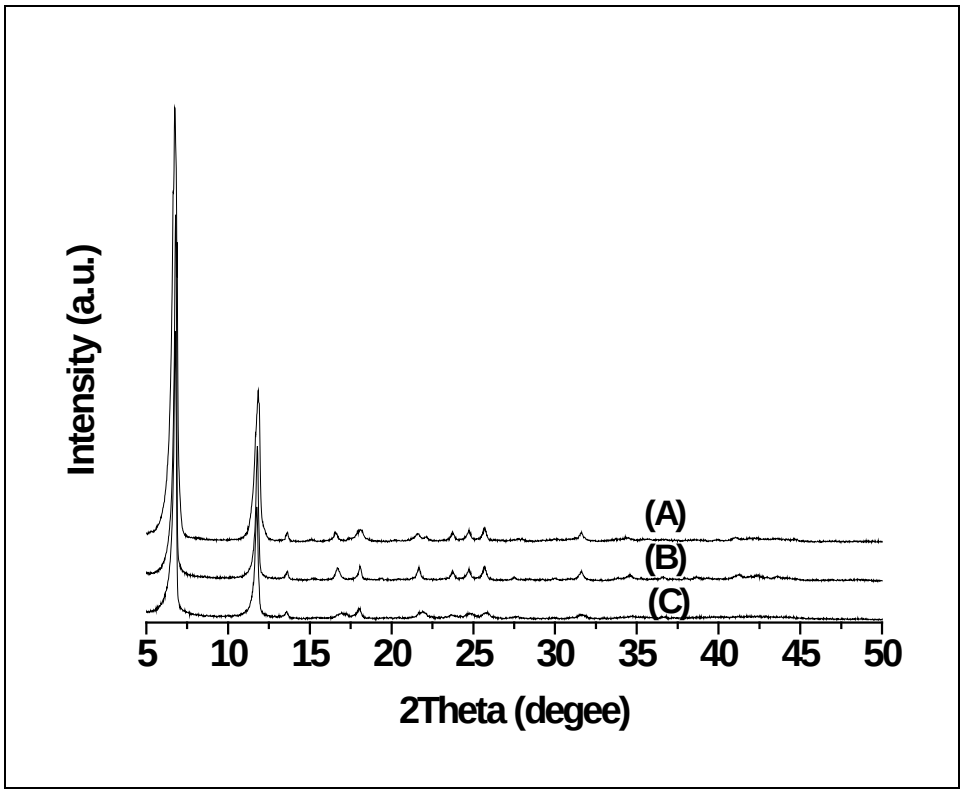

Figure 33. XRD patterns ranged from 5-60° in 2θ for (A) pristine Zn-MOF-74, in good agreement with literature [123,124,132] ; (B) Pt doped Zn-MOF-74 before H_2 treatment at 150°C for 16 hours; (C) Pt doped Zn-MOF-74 after H_2 treatment at 150°C for 16 hours. No peak change was observed on Zn-MOF-74 after Pt-doping procedure and H_2 treatment.

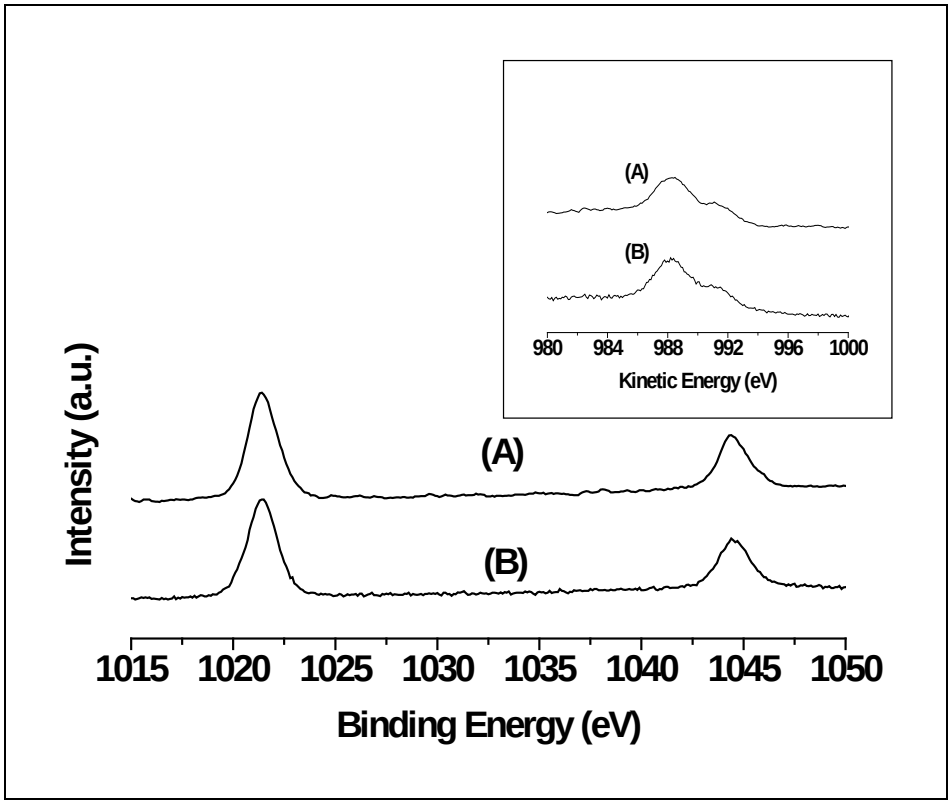

Figure 34. Zn 2p XPS spectra of (A) pristine Zn-MOF-74, (B) Pt doped Zn-MOF-74 after H_2 treatment at 150°C for 16 hours; inset figure shows Zn LMM spectra of (A) pristine Zn-MOF-74, (B) Pt doped Zn-MOF-74 after H_2 treatment at 150°C for 16 hours.
No peak shift was observed in Zn 2p XPS spectra and Zn LMM spectra for Pt doped Zn-MOF-74 after H_2 treatment at 150°C for 16 hours compared with pristine Zn-MOF-74, which indicates that Zn^{2+} in Zn-MOF-74 was not reduced by H_2 at 150°C for 16 hours.

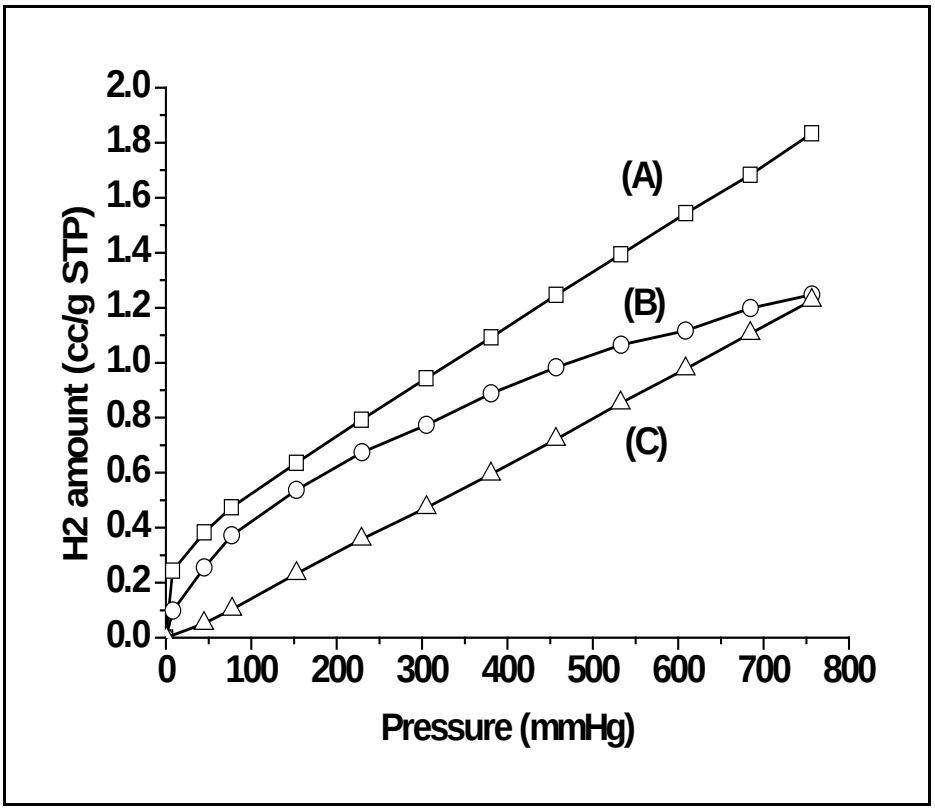

Figure 35: H_2 isotherms at 298K for (A) untreated Pt-HKUST-1 (never contacted with hydrogen before the measurement), (B) treated Pt-HKUST-1 (treated in H_2 at 150°C for 16 h), (C) Pristine HKUST-1.

Chapter 4: Investigation on the Effect of Zinc Ion on the Interaction between Hydrogen and Zeolites H-ZSM-5 and H-Y by TPD Study

Introduction

Recently, zeolite ZSM-5 modified with transition metal cations attracted much attention due to the unusual catalytic properties of ion exchanged ZSM-5 in many fields. Hammond et al. applied copper and iron modified ZSM-5 for selective oxidation of methane to methanol and found iron is involved in the activation of carbon-hydrogen bond while copper allows ethanol to form as the major product.[1] Gruenert and coworkers studied the performance of Cu-ZSM-5 synthesized via different approaches for selective reduction of NO_x by hydrocarbons in the presence of oxygen and concluded the variation of catalytic activities is related with the dispersion of Cu in zeolites.[2] Ion exchanged ZSM-5 zeolites were also found to be efficient catalysts for dehydrogenation and aromatization of alkanes by many groups. Su's work showed that Mo-ZSM-5 has high catalytic performance in the conversion of methane to aromatics.[3] Ga-ZSM-5, Fe-ZSM-5 and Mn-ZSM-5 were also studied by Hagen et al in the conversion of cyclohexane and the nonoxidative conversion of ethane and their catalytic behavior was related to acid properties through temperature programmed desorption of ammonia.[4] Besides these ion exchanged ZSM-5, Zn-ZSM-5 also attracted much attention in this field, e.g., Heemsoth applied Zn-ZSM-5 for aromatization of ethane, [5] while Lee et al. utilized Zn-ZSM-5 as a catalyst for aromatization of branched olefins.[6] During the aromatization process, one important step is dehydrogenation, which was facilitated by Zn cations in ZSM-5.[7,8] Kanzasky et al. utilized DRIFTS technology and observed special Zn-H stretching mode, which was assigned to the dissociative adsorption of H_2 on Zn exchanged zeolites.[9-11]

Temperature programmed desorption (TPD) is a powerful tool to study the interaction between hydrogen and adsorbent.[12-14] This work applied H_2-TPD to investigate the interactions between hydrogen and several zeolites and found Zn cations indeed play an important role in the chemisorption of hydrogen on zeolites, which is also influenced by the type of zeolites framework.

Experimental Section

Sample synthesis. Zinc nitrate hexahydrate $Zn(NO_3)_2 \cdot 6H_2O$ was obtained from Sigma-aldrich Company; zeolite NH_4-ZSM-5 and H-Y were obtained from Zeolyst International. NH_4-ZSM-5 was calcined at 773K for 5h in order to form H-ZSM-5 by decomposing NH_4^+ to H^+. 0.5 gram H-ZSM-5 was ion exchanged with 50ml of 0.02M $Zn(NO_3)_2$ at 353K overnight and the ion exchange procedure was repeated three times. Then the sample was filtered, washed with deionized water, dried in air at 383K overnight and calcined in vacuo at 623K for 20h. The obtained sample was denoted as Zn-ZSM-5-1. 0.5 gram H-ZSM-5 was ion exchanged with 50ml of 0.01M $Zn(NO_3)_2$ at 353K overnight and the ion exchange procedure was repeated only once. The following treatments to this sample are the same with Zn-ZSM-5-1. The obtained sample was denoted as Zn-ZSM-5-2. Similar with Zn-ZSM5-5-1, Zn-Y was obtained by three times ion exchange of 0.5 gram H-Y with 50ml of 0.02M $Zn(NO_3)_2$ at 353K overnight and the same following treatments. All these samples were subject to calcinations at 623K for 20 hours in vacuo before further measurements.

Characterization. The powder X-ray diffraction (XRD) measurements were carried out with a Rigaku Rotaflex D/Max-C system with Cu Kα (λ = 0.1543 nm) radiation. N_2 adsorption isotherms were measured by Micromeritics ASAP 2020. N2 adsorption

isotherms were measured at 77K. The concentrations of Zn in Zn-ZSM-5 and Zn-Y were measured by using EDX affiliated Phillips XL30 FEG SEM.

Temperature Programmed Desorption (TPD). TPD curves for all samples were measured with an AeroVac 1200 Magnetic Sector mass spectrometer (VTI, Inc.), operated at an accelerating voltage of 70 eV. The detailed description of the TPD apparatus was given in our previous work.[12] And the TPD experiments were conducted by taking similar procedure with previous works.[12-14] Initially, 120mg of sample was put into a stainless steel holder and degassed in a high vacuo at 623K overnight until the pressure in the system was lower than $5*10^{-8}$ Torr. Then the sample was cooled down to 273K or 298K or 323K, dosed with pure hydrogen at the pressure of 750 Torr and allowed to reach equilibrium after a period of time at corresponding temperature. After reaching equilibrium, the sample holder was immersed and quenched in liquid nitrogen. The system was then slowly degassed until the pressure dropped down lower than 10^{-6} Torr to remove excess gas and hydrogen level were at the background. After that, the sample was heated at a constant rate of 10K/min or 15K/min or 20K/min from 77K to 623K, while the effluent gas was monitored with a mass spectrometer.

Results and discussions

The XRD pattern of Zn-ZSM-5 is shown in Figure 36. The obtained Zn-ZSM-5 exhibited the characteristic of peaks associated with MFI structure, indicating the zeolite structure was retained after the ion exchange process. EDX (Energy dispersive X-ray spectroscopy) was applied to measure the concentration of Zn in Zn-ZSM-5-1, Zn-ZSM-5-2 and Zn-Y and the corresponding EDX spectra are shown in Figure 37 (A), (B) and (C). And the concentration of Zn in these three samples is 1.65wt%, 1.17wt% and 2.29

wt%, respectively. Higher zinc concentration in Zn-Y compared with Zn-ZSM-5-1 is probably because the Si/Al ratio in Zn-Y (Si/Al=15) is lower than that in Zn-ZSM-5-1 (Si/Al=25) thus more cations can be exchanged. Through the comparison between Zn-ZSM-5-1 and Zn-ZSM-5-2, it is also found that repeating exchange procedure multiple times and using higher concentration solution for exchange will lead more zinc ions introduced into zeolites. N_2 isotherms at 77K were also measured to check the effect of ion exchange procedure on the zeolites and the corresponding results are shown in Figure 38. BET surface area analysis showed that Zn-ZSM-5-1 has a surface area of 404 m^2/g and Zn-ZSM-5-2 has a surface area of 420 m^2/g, both of which are lower than the surface area of original form H-ZSM-5. This indicates that the ion exchange procedure with vigorous stirring at 353K caused slight collapse of structure. And multiple times exchange further decreased the surface area. Similar phenomenon was also observed on Zn-Y. After ion exchange procedure, the surface area of H-Y dropped from 780 m^2/g to about 740 m^2/g, which is similar with literature results.[15]

The interaction between hydrogen and ZSM-5 was investigated by H_2-TPD measurements by using mass spectrometer. Figure 39 shows the H_2-TPD curves with a heating rate of 10K/min for sample Zn-ZSM-5-1, which was dosed with hydrogen at different temperature.

Two split peaks were found in Figure 39. The first one around 120K was assigned to physisorption of H_2 molecules on the surface of Zn-ZSM-5. Besides the weak Van der Waals interaction, the appearance of peaks in the range of 370K-450K indicates that there is another stronger interaction between hydrogen and Zn-ZSM-5, i.e., the chemisorption of hydrogen on Zn-ZSM-5. Moreover, it is found that the peak intensity of hydrogen

chemisorption on Zn-ZSM-5 is higher after reaching equilibrium with dosed hydrogen at higher temperature (the peak intensity of curve C > B > A in Figure 39), which means more hydrogen chemisorbed on Zn-ZSM-5 at higher dosing temperature. One possible explanation is that the chemisorption of hydrogen on Zn-ZSM-5 requires some energy to overcome the energy barrier, thus higher temperature environment provides extra external energy facilitating more hydrogen to overcome the energy barrier to chemisorb on Zn-ZSM-5. Meanwhile, higher dosing temperature also caused the TPD peak shifted to higher temperature position, which indicates the activation energy for desorption increases with increased dosing temperature. Similar phenomena were also observed when the heating rate of TPD changed to 15K/min and 20K/min and the results are shown in Figure 40 and 41.

Figure 40 and 41 exhibit the same trend with Figure 39, which is that the peak intensity of hydrogen chemisorption increased and the peaks shifted to higher temperature position with elevated dosing temperature. Through the comparison of Figure 39, 40 and 41, it is also found that higher heating rates led higher peak intensity (higher desorption rate) and the shifts of TPD peaks to higher temperature positions, which is consistent with previous TPD studies.[16-18] For example, when Zn-ZSM-5-1 was dosed with hydrogen at 298K and processed with TPD at the heating rate of 10K/min, the peak maximum temperature (T_m) for hydrogen chemisorption is about 408K. And this temperature increased to 428K at the heating rate of 15K/min and 450K at the heating rate of 20K/min, respectively. And the peak intensity (desorption rate) was increased from $5.3*10^{-9}$ at heating rate of 10K/min to $6.6*10^{-9}$ at 15K/min and $9.8*10^{-9}$ at 20K/min. This is because at higher heating rate, more energy was provided in unit time to break the

strong interaction between chemisorbed hydrogen and Zn-ZSM-5, thus more hydrogen was released in unit time, which eventually led to higher desorption rate (higher peak intensity). Similar procedures were also taken on Zn-ZSM-5-2 and the corresponding TPD curves are shown in Figure 42, 43 and 44.

The TPD peak changes of Zn-ZSM-5-2 with dosing temperatures and heating rates show the same trend with Zn-ZSM-5-1, which was mentioned above. However, compared with Zn-ZSM-5-1, the peak intensity for hydrogen chemisorptions is lower under the same condition and peak maximum temperatures (T_m) shift to lower temperature position. For example, T_m for Zn-ZSM-5-2 dosed with hydrogen at 298K at the heating rate of 10K/min is 400K, which is lower than T_m (410K) for Zn-ZSM-5-1 under the same condition. Meanwhile, the peak intensity for hydrogen chemisorptions on Zn-ZSM-5-2 dosed with hydrogen at 298K at the heating rate of 10K/min is $3.3*10^{-9}$, which is lower than the peak intensity ($5.3*10^{-9}$) on Zn-ZSM-5-1 under the same condition. This is assumed to be related with lower Zn concentration in Zn-ZSM-5-2 compared with Zn-ZSM-5-1 (as to be discussed). The complete comparison between Zn-ZSM-5-1 (denoted as A) and Zn-ZSM-5-2 (denoted as B) is shown in Table 6.

With assuming the pre-exponential factor and activation energy for desorption is independent of surface coverage and heating rates, modified Redhead equation can be used to estimate the activation energy for desorption by monitoring T_m changes with heating rates.[16,19] The activation energy for desorption was determined by evaluating the slope of a plot of $\ln(T_m^2/\beta)$ against $1/T_m$. The plots are shown in Figure 45 and 46.

The activation energy for hydrogen desorption from Zn-ZSM-5-1 was calculated to be 14.8 kJ/mol with dosing temperature at 273K, 19.3 kJ/mol at 298K and 33.6 kJ/mol at

323K, while the activation energy for hydrogen desorption from Zn-ZSM-5-2 was calculated to be 14.1 kJ/mol at 273K, 15.7 kJ/mol at 298K and 30.0 kJ/mol at 323K. These results confirm our previous conclusion that higher dosing temperature leads to higher activation energy for desorption. The comparison between the Zn-ZSM-5-1 and Zn-ZSM-5-2 also reveals that higher zinc concentration in ZSM-5 leads to higher activation energy for desorption from Zn-ZSM-5, which is consistent with the previous discovery that the TPD peaks of ZSM-5 with higher zinc concentration shifted to higher temperature positions. In order to verify this conclusion, H-ZSM-5 without zinc ion was also tested after reaching equilibrium with hydrogen at 298K and TPD experiments were taken at the heating rate of 10K/min and 20K/min. The corresponding TPD curves are shown in Figure 47.

The only peak of the two TPD curves shown in Figure 47 was assigned to weak physisorption of hydrogen on H-ZSM-5. No peak at higher temperature position (chemisorption peak) was observed, which is totally contrary to previous results for Zn-ZSM-5. This demonstrates that zinc ions in ZSM-5 indeed play an important role in the chemisorption of hydrogen on ZSM-5. This discovery is in good agreement with previous works. For example, Kazansky et al. observed the appearance of a new H-H stretching frequency at 3940 cm^{-1} and Zn-H stretching frequency at 1930cm^{-1} on Zn-ZSM-5 by using DRIFTS technique, which were assigned to dissociative adsorption of H_2 on Zn-ZSM-5.[9-11] And they also observed increased intensity of Zn-H with elevated adsorption temperature, which indicates more hydrogen formed bonding with Zn in Zn-ZSM-5 with increased temperature. This also consolidates our above TPD works that chemisorption peak intensity increased with dosing temperature increasing. Iglesia et al found Zn has an

effect of facilitating dissociative adsorption of dihydrogen on ZSM-5 during their investigations of propane aromatization and alkane dehydrogenation mechanism by taking isotopic equilibration measurements.[7,8] In order to further verify the effect of Zn cations on hydrogen chemisorption on zeolites, another pair of zeolites—Zn-Y and H-Y were also measured. The corresponding TPD curves of Zn-Y and H-Y dosed with hydrogen at 298K at the heating rate of 20K/min is shown in Figure 48.

As shown in Figure 48, there is no chemisorption peak of hydrogen on H-Y while there is a chemisorptions peak on Zn-Y. These results confirm our previous conclusion that Zn has a significant influence on hydrogen chemisorption on zeolites, which is also consistent with other studies.[7-11] However, the peak maximum temperature and the peak intensity of TPD on Zn-Y is lower than that on Zn-ZSM-5. This phenomenon means the interaction between hydrogen and Zn-Y is less strong than the interaction between hydrogen and Zn-ZSM-5, and more hydrogen chemisorbed on Zn-ZSM-5 than Zn-Y, although Zn concentration in Zn-Y is higher than in Zn-ZSM-5. This demonstrates that not only Zn cations but also the framework of zeolites affects hydrogen chemisorption on zeolites. This conclusion is in good agreement with many simulation works. For example, Barbosa et al. utilized periodical density functional theory to study the adsorption and dissociation of dihydrogen on several Zn exchanged zeolites and predicted that hydrogen adsorbs either molecularly or in a dissociative way on chabazite and mordenite but always adsorbs molecularly on ferrierite by evaluating the adsorption and dissociation energies for different structures.[20] Shubin and his coworkers performed cluster model quantum chemical calculations to investigate in the interaction energies of hydrogen with Zn cations in different structures and demonstrated that even for Zn cations in the same

zeolites, different locations have different strength of the interaction between hydrogen and Zn ions.[21]

Conclusions

In this work, a series of TPD experiments were conducted on two Zn-ZSM-5 samples with different zinc concentration. It is found higher dosing temperature leads to higher activation energy for desorption, i.e., the interaction between hydrogen and Zn-ZSM-5 is stronger at higher dosing temperature. Meanwhile, more hydrogen chemisorbed on Zn-ZSM-5 at higher dosing temperature due to more external energy provided to overcome the energy barrier. TPD studies also demonstrate that Zn cations play a significant role in hydrogen chemisorption on zeolites. Higher concentration of zinc ions in zeolites will strengthen the interaction between hydrogen and zeolites, thus leads to more hydrogen chemisorbed on ZSM-5 but it requires higher temperature to release hydrogen due to higher activation energy for hydrogen desorption. This effect of Zn on hydrogen chemisorptions on zeolites is also influenced by the framework of zeolites. Different types of frameworks exhibited different behaviors for hydrogen chemisorptions (the amount of chemisorbed hydrogen, the strength of the interaction between chemisorbed hydrogen and zeolites).

Acknowledgments

This work was supported by Air Products and Chemicals Inc. The discussions with Dr. Sandrine Rivillon and Dr. Eric H. Klingenberg were very helpful.

References:

(1) Hammond, C.; Forde, M. M.; Ab Rahim, M. H.; Thetford, A.; He, Q.; Jenkins, R. L.; Dimitratos, N.; Lopez-Sanchez, J. A.; Dummer, N. F.; Murphy, D. M.; Carley, A. F.; Taylor, S. H.; Willock, D. J.; Stangland, E. E.; Kang, J.; Hagen, H.; Kiely, C. J.; Hutchings, G. J. *Angewandte Chemie International Edition* **2012**, *51*, 5129.

(2) Gruenert, W.; Hayes, N. W.; Joyner, R. W.; Shpiro, E. S.; Siddiqui, M. R. H.; Baeva, G. N. *The Journal of Physical Chemistry* **1994**, *98*, 10832.

(3) Su, L.; Liu, L.; Zhuang, J.; Wang, H.; Li, Y.; Shen, W.; Xu, Y.; Bao, X. *Catalysis Letters* **2003**, *91*, 155.

(4) Hagen, A.; Schneider, E.; Benter, M.; Krogh, A.; Kleinert, A.; Roessner, F. *Journal of Catalysis* **2004**, *226*, 171.

(5) Heemsoth, J.; Tegeler, E.; Roessner, F.; Hagen, A. *Microporous and Mesoporous Materials* **2001**, *46*, 185.

(6) Kim, Y. H.; Lee, K. H.; Nam, C.-M.; Lee, J. S. *ChemCatChem* **2012**, *4*, 1143.

(7) Biscardi, J. A.; Iglesia, E. *Journal of Catalysis* **1999**, *182*, 117.

(8) Biscardi, J. A.; Meitzner, G. D.; Iglesia, E. *Journal of Catalysis* **1998**, *179*, 192.

(9) Kazansky, V. B. *Journal of Catalysis* **2003**, *216*, 192.

(10) Kazansky, V. B.; Serykh, A. I.; Anderson, B. G.; van Santen, R. A. *Catalysis Letters* **2003**, *88*, 211.

(11) Kazansky, V. B.; Serykh, A. I. *Physical Chemistry Chemical Physics* **2004**, *6*, 3760.

(12) Lachawiec, A. J.; Yang, R. T. *The Journal of Physical Chemistry C* **2009**, *113*, 13933.

(13) Wang, L. F.; Stuckert, N. R.; Chen, H.; Yang, R. T. *Journal of Physical Chemistry C* **2011**, *115*, 4793.

(14) Wang, L. F.; Stuckert, N. R.; Yang, R. T. *AIChE Journal* **2011**, *57*, 2902.

(15) Langmi, H. W.; Book, D.; Walton, A.; Johnson, S. R.; Al-Mamouri, M. M.; Speight, J. D.; Edwards, P. P.; Harris, I. R.; Anderson, P. A. *Journal of Alloys and Compounds* **2005**, *404–406*, 637.

(16) Busser, G. W.; Hinrichsen, O.; Muhler, M. *Catalysis Letters* **2002**, *79*, 49.

(17) Wei, F. G.; Hara, T.; Tsuzaki, K. *Metallurgical and Materials Transactions B-Process Metallurgy and Materials Processing Science* **2004**, *35*, 587.

(18) Choudhary, V. R.; Mantri, K. *Microporous and Mesoporous Materials* **2000**, *40*, 127.

(19) Masel, R. I. *Principles of Adsorption and Reaction on Solid Surfaces*; Wiley, 1996.

(20) Barbosa, L. A. M. M.; van Santen, R. A. *The Journal of Physical Chemistry C* **2007**, *111*, 8337.

(21) Shubin, A. A.; Zhidomirov, G. M.; Yakovlev, A. L.; van Santen, R. A. *The Journal of Physical Chemistry B* **2001**, *105*, 4928.

Heating rate	10K/min		15K/min		20K/min	
Sample	A	B	A	B	A	B
	T_m (K)	T_m (K)	T_m (K)	T_m (K)	T_m (K)	T_m (K)
dosed at 273K	429	425	405	398	429	425
dosed at 298K	450	447	428	420	450	447
dosed at 323K	470	468	455	448	470	468

Table 6. Summary of peak maximum temperatures for hydrogen chemisorptions on (A) Zn-ZSM-5-1 and (B) Zn-ZSM-5-2 at different dosing temperatures and heating rates

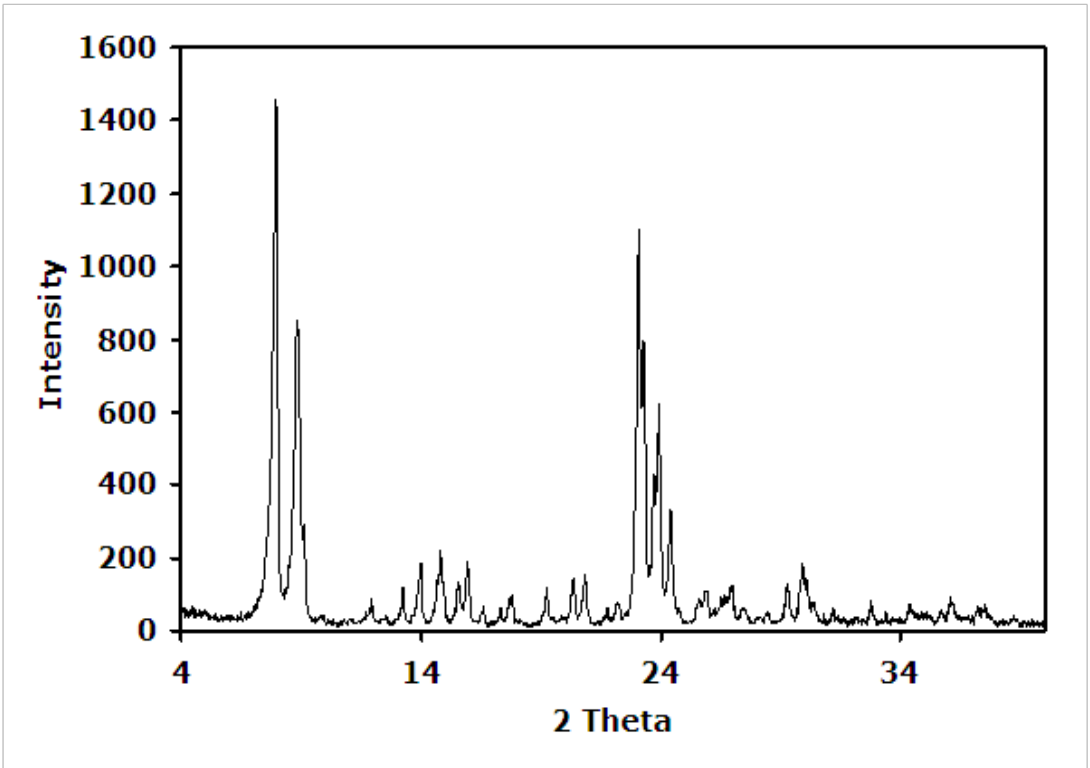

Figure 36. XRD pattern of Zn-ZSM-5.

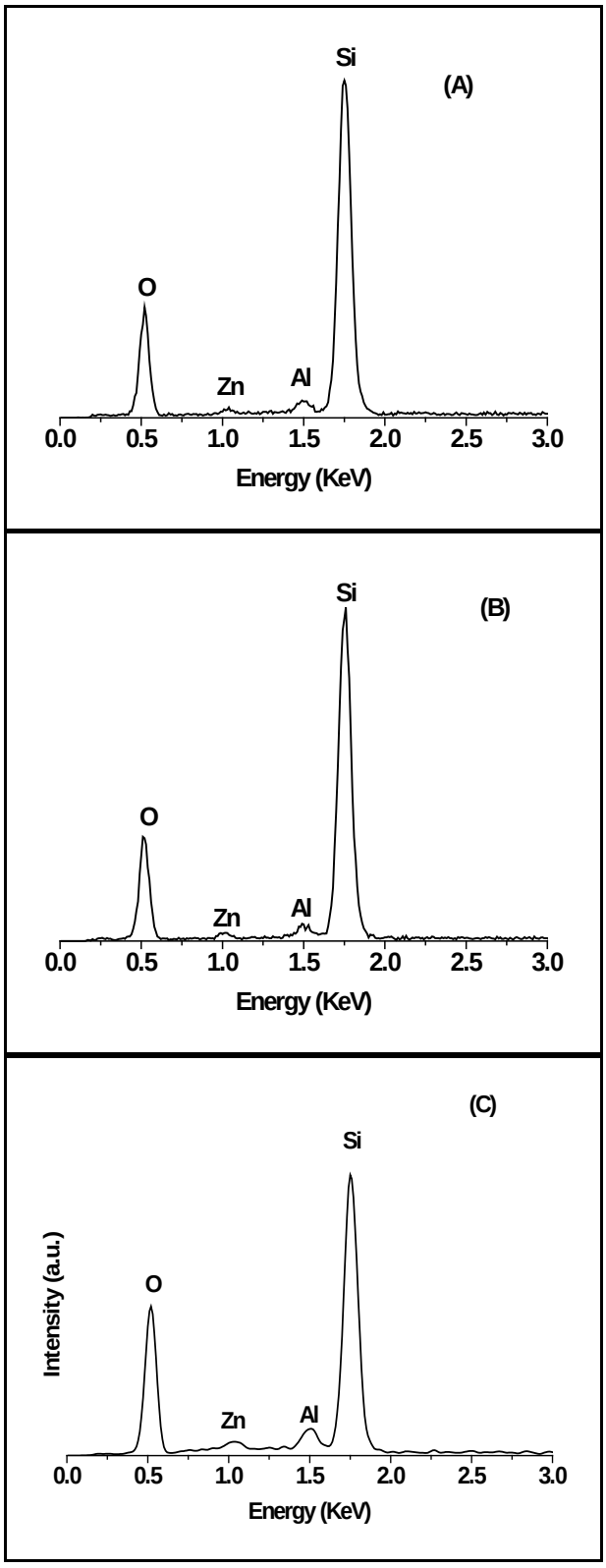

Figure 37. EDX spectra of (A) Zn-ZSM-5-1, (B) Zn-ZSM-5-2, (C) Zn-Y

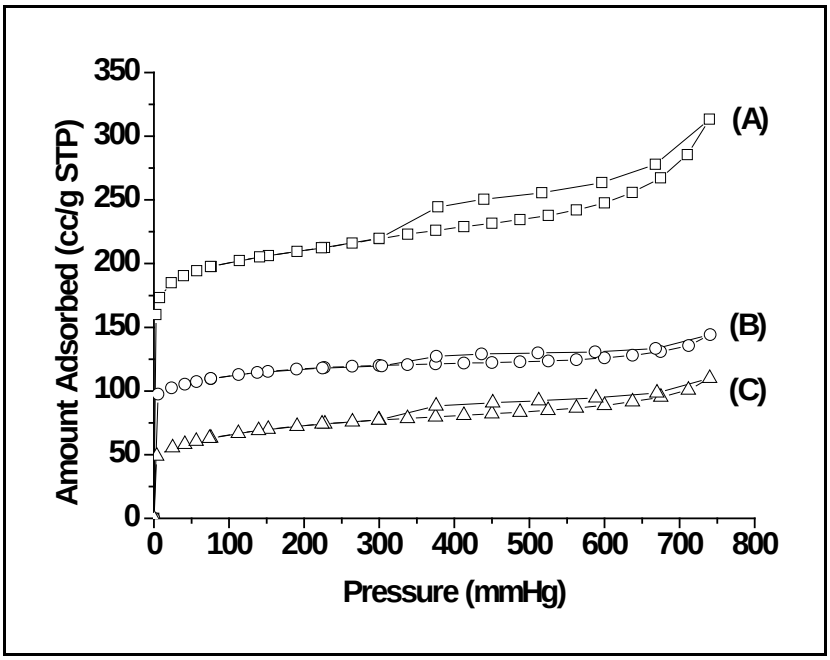

Figure 38. N_2 isotherms at 77K on (A) Zn-Y, (B) Zn-ZSM-5-1, (C) Zn- ZSM-5-2; the isotherm of Zn-ZSM-5-2 was offset by 50 cc/g STP for clarity.

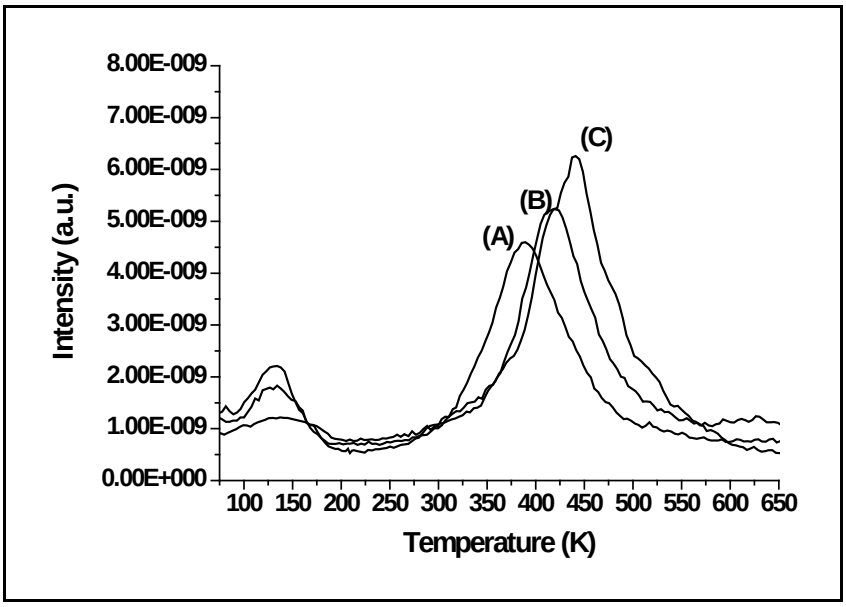

Figure 39. H_2-TPD curves (10K/min) for Zn-ZSM-5-1, dosed with H_2 at (A) 273K (B) 298K (C) 323K.

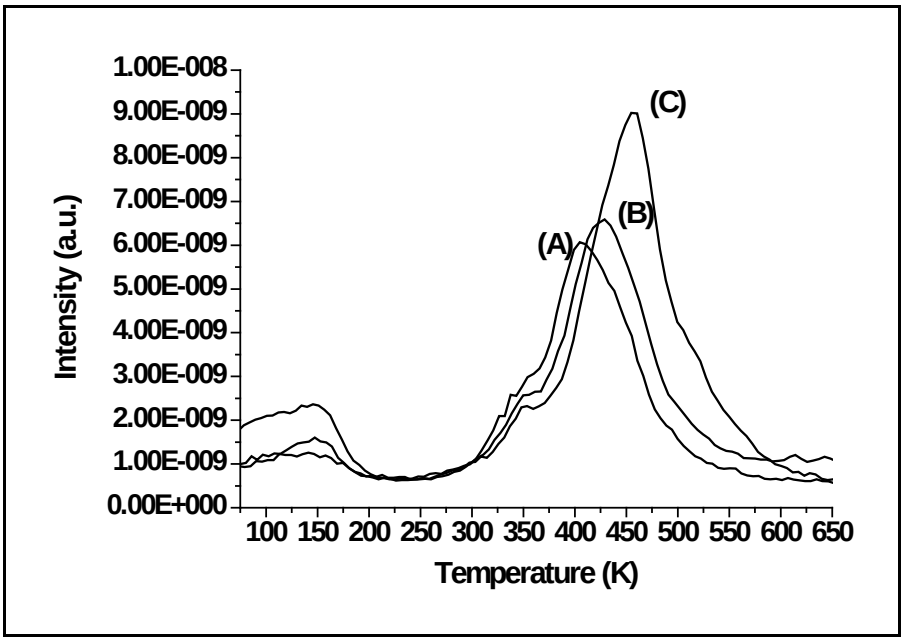

Figure 40. H_2-TPD curves (15K/min) for Zn-ZSM-5-1, dosed with H_2 at (A) 273K (B) 298K (C) 323K.

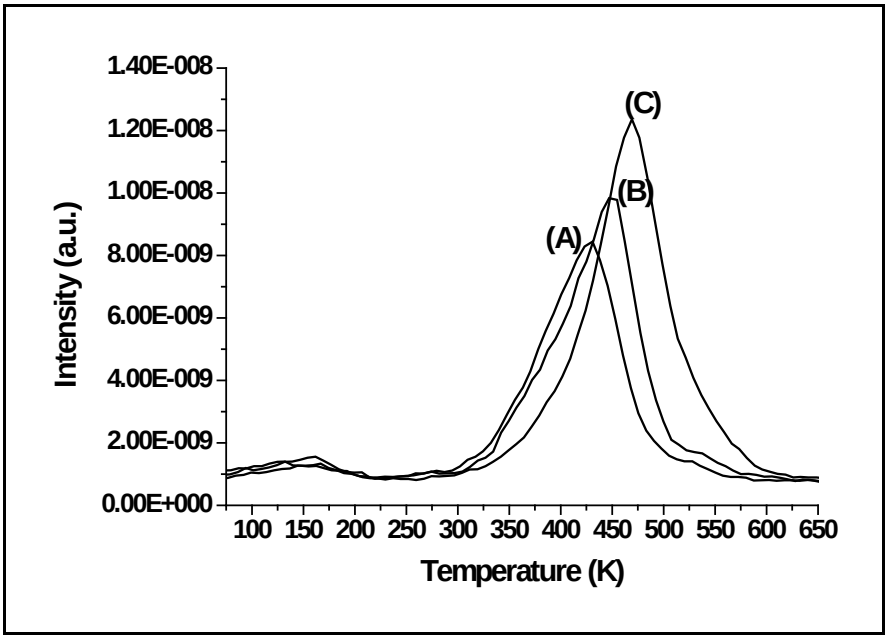

Figure 41. H_2-TPD curves (20K/min) for Zn-ZSM-5-1, dosed with H_2 at (A) 273K (B) 298K (C) 323K.

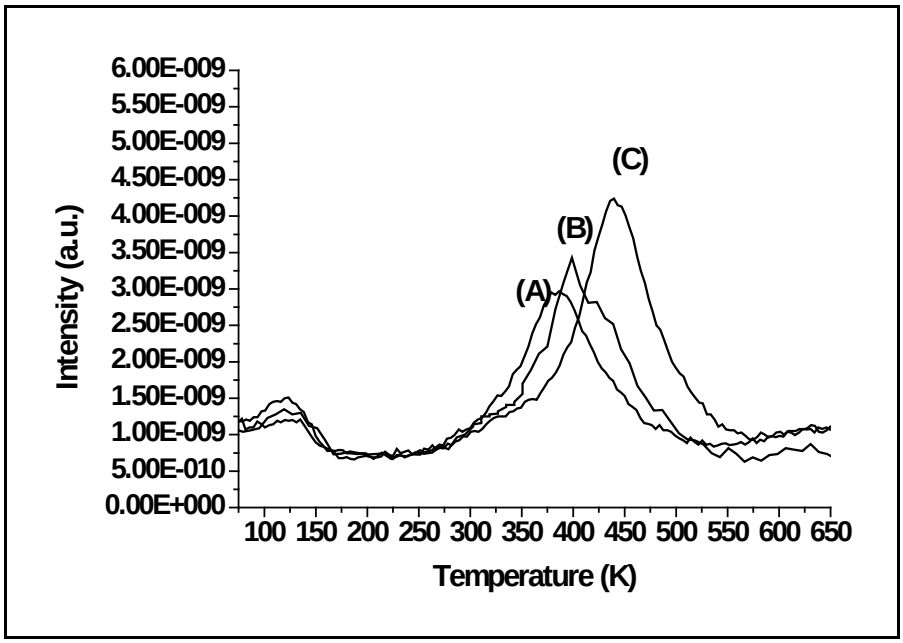

Figure 42. H_2-TPD curves (10K/min) for Zn-ZSM-5-2, dosed with H_2 at (A) 273K (B) 298K (C) 323K.

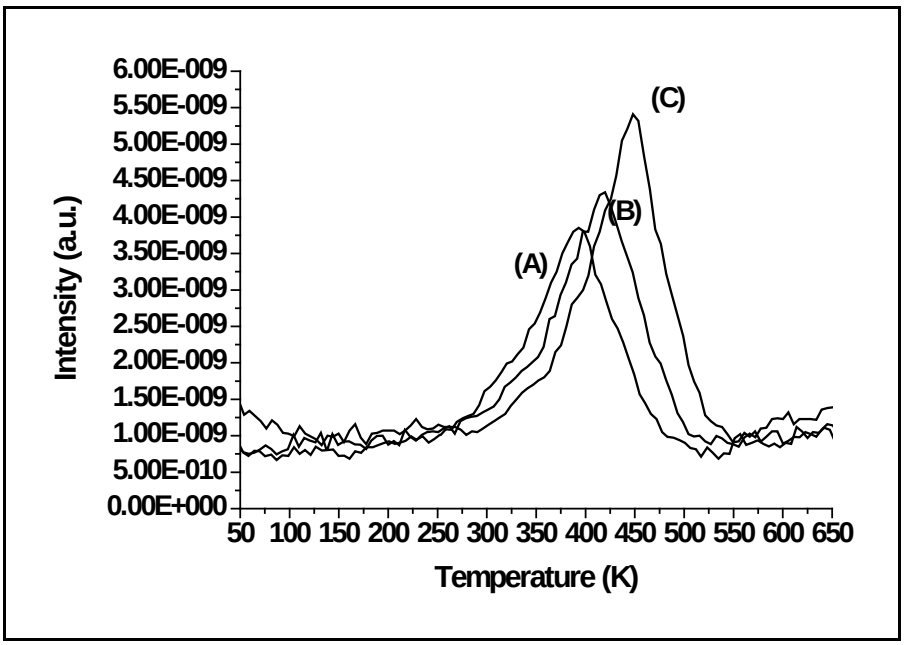

Figure 43. H_2-TPD curves (15K/min) for Zn-ZSM-5-2, dosed with H_2 at (A) 273K (B) 298K (C) 323K.

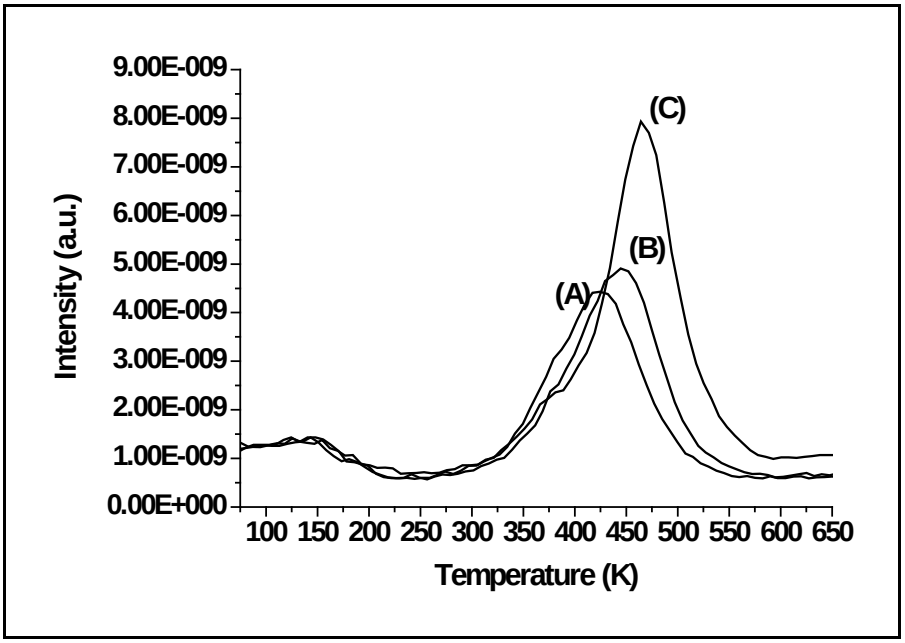

Figure 44. H_2-TPD curves (20K/min) for Zn-ZSM-5-2, dosed with H_2 at (A) 273K (B) 298K (C) 323K.

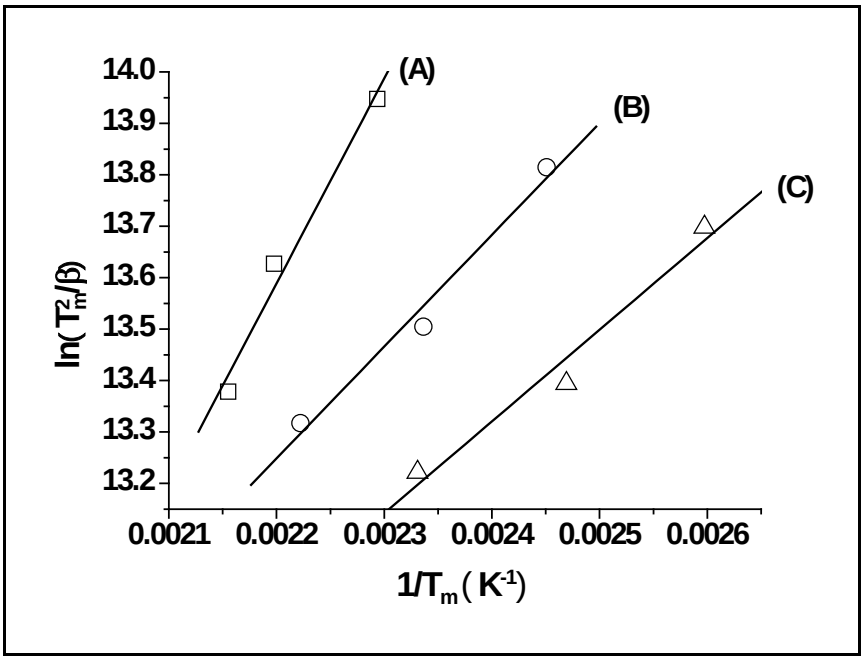

Figure 45. Plots of $\ln(T_m^2/\beta)$ against $1/T_m$ for Zn-ZSM-5-1 at different dosing temperature: (A) 323K (B) 298K (C) 273K

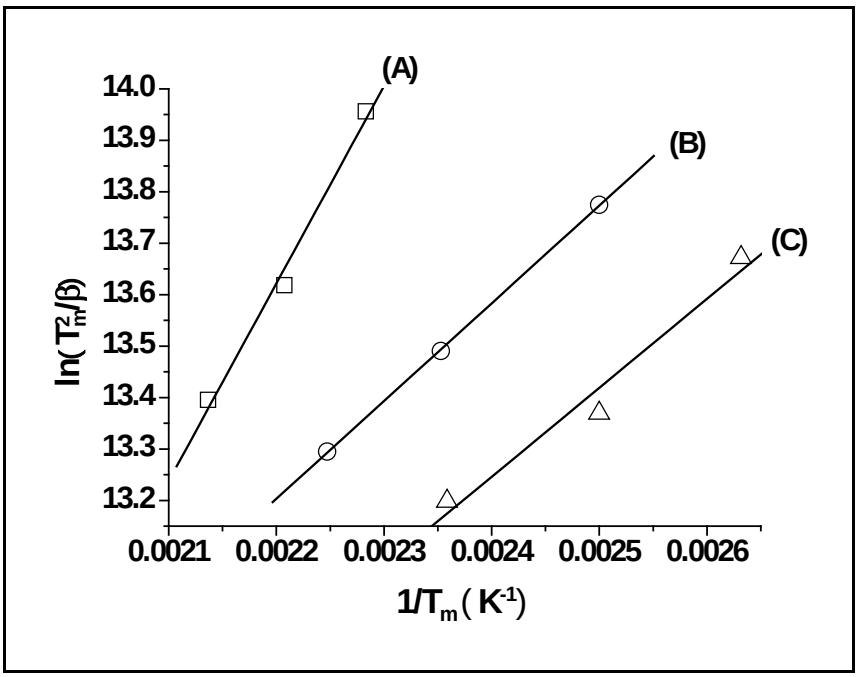

Figure 46. Plots of $\ln(T_m^2/\beta)$ against $1/T_m$ for Zn-ZSM-5-2 at different dosing temperature: (A) 323K (B) 298K (C) 273K

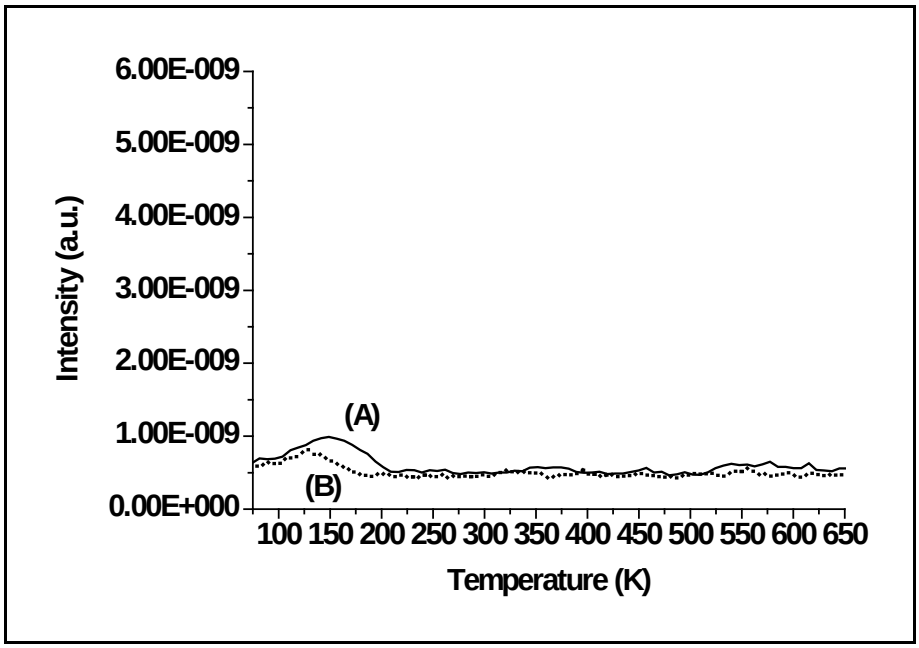

Figure 47. H_2-TPD curves for H-ZSM-5 dosed with hydrogen at 298K at the heating rate of (A) 20K/min (B) 10K/min

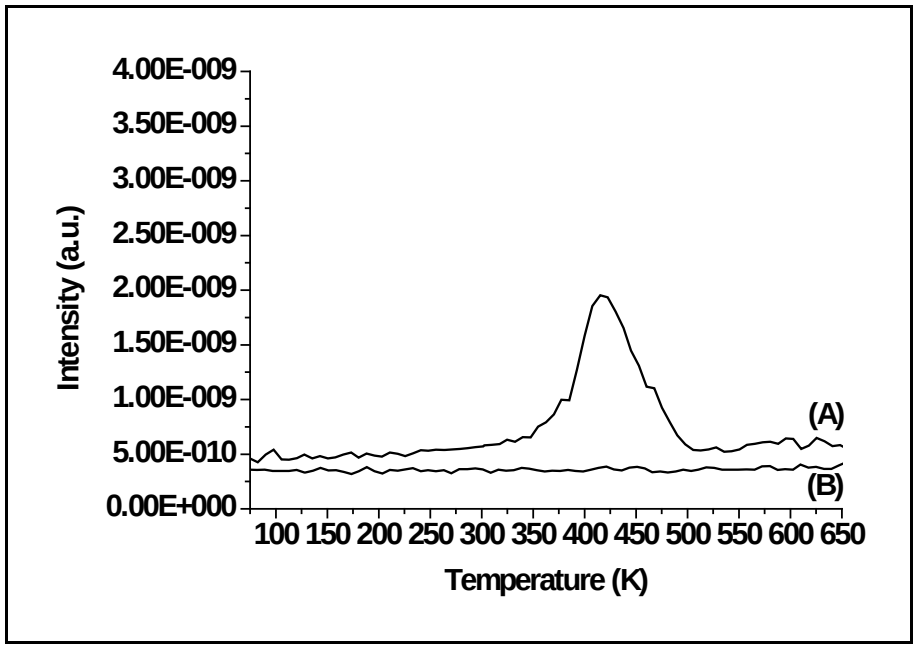

Figure 48. TPD curves of samples dosed with hydrogen at 298K at the heating rate of 20K/min. (A) Zn-Y (B) H-Y. (TPD curve of H-Y was offset by 1.5E-10 for clarity).

Chapter 5: Desulfurization of high-sulfur jet fuel by mesoporous π-complexation adsorbents

Introduction

Because of the high energy density, ready availability, safety and convenient storage, gasoline, diesel and jet fuel are the best sources for hydrogen for fuel cell applications.[1] In particular, military jet fuels are considered by many as an excellent fuel source for hydrogen for on-board fuel cell generator systems, and are desired for use in various military applications. For certain applications, such as distributed shipboard power generation, high flashpoint liquid fuels are absolutely mandatory for realization of such systems, as a result of safety considerations.[2] However, jet fuels generally contain very high concentrations of sulfur. For example, JP-5 high flashpoint jet fuel typically contains 1000–1500 ppm of sulfur (e.g., the JP-5 jet fuel contains around 1270 ppmw sulfur, with a maximum specification of 3000 ppm)[3]. Similarly, JP-8 jet fuel also has a maximum specification of 3000 ppm of sulfur. F-76 marine distillate fuel currently can contain up to 10000 ppm of sulfur, although a specification change will reduce this to 5000 ppm.[4] When the hydrogen feeding the fuel cell is produced via catalytic autothermal reforming of jet fuels, sulfur compounds that can poison the follow-on processing operations and ultimately the electrode catalyst of the fuel cell will also be generated simultaneously. Therefore, reducing the sulfur concentration of jet fuels is a key issue for the utilization of jet fuels as a hydrogen source for on-board fuel cells. Removal of sulfur containing compounds from transportation fuels is an important operation in petroleum refining, and is achieved by catalytic processes operated at high pressures and elevated temperatures. Today, refineries rely on hydrodesulfurization (HDS) processes to reduce sulfur levels,

but achieving deep-desulfurization levels would require increasing existing reactor sizes and increasing hydrogen consumption.[5] There has been much recent interest in using adsorbents for selective desulfurization of fuels.[6-23] Additionally, for military fuel cell generators, HDS is not a viable option due to the requirement of high purity, high pressure hydrogen, large reactors, valving, actuators and associated equipment. In systems that are sensitive to power density, weight and volume, these systems lose applicability.[24]

Our group has recently developed a class of adsorbents that rely on π-complexation bonding to selectively remove organosulfur molecules from commercial fuels.[1,3,25-27] It was found that Cu(I)-Y zeolite exhibited highly selective removal for sulfur compounds from transportation fuels. It was concluded that Cu^+ in Cu(I)-Y zeolite can remove sulfur compounds by π-complexation adsorption with thiophenic compounds.[1] Our results also indicted that metal halides supported on active carbon, such as CuCl/AC or $PdCl_2$/AC, are effective in the desulfurization of JP-5.[3,25] More recently, we have found that $PdCl_2$/SBA-15 and $PdCl_2$/MCM-41 were excellent adsorbents for desulfurizing very-high-sulfur commercial jet fuels such as an JP-5 that contained 847 ppmw S.[26] For this JP-5, significant breakthrough (<10 ppmw S) occurred at about 15.0 and 50.0 mL/g with $PdCl_2$/MC-41 or $PdCl_2$/SBA-15, respectively. Although the regeneration result of the spent $PdCl_2$/SBA-15 was unsatisfactory as only around 48% capacity of $PdCl_2$/SBA-15 could be recovered, these findings demonstrated that the support has an important effect on the performance of adsorbents in the desulfurization of jet fuels.[26] Regeneration is an important aspect that should be considered, especially for on-board applications. Safety, high efficiency and availability of reactants need to be considered for the regeneration of

saturated adsorbents. Heating the spent adsorbents using air is an effective choice for the regeneration of saturated adsorbent.[1] Therefore, a convenient regeneration sorbent, Cu_2O/MCM-41 was developed for the deep desulfurization of a JP-5 light fraction (841 ppmw S). Although the spent Cu_2O/MCM-41 can be completely regeneration by heating in air, the product fuel of 10 mL per gram sorbent still contained ~50 ppmw S.[27]

In our previous study for the bulk separation of C_4 olefins from paraffins, a π-complexation capable sorbents, $AgNO_3/SiO_2$, was found to have excellent capacities and selectivities for this application.[28] $AgNO_3$/SBA-15 and $AgNO_3$/MCM-41 adsorbents were prepared and studied in this work. The results show that the supported $AgNO_3$ is an excellent adsorbent for selective desulfurization from the jet fuel; ~15.0 mL of the JP-5 can be desulfurized per gram adsorbent from 1172 ppmw S to < 1 ppmw S with $AgNO_3$/MCM-41 adsorbent, and ~50% capacity of the spent $AgNO_3$/MCM-41 can be recovered upon air regeneration after the 1st regeneration cycle.

Materials and methods

Adsorbents preparation. Monolayer $AgNO_3$/SBA-15 or $AgNO_3$/MCM-41 was prepared by impregnating SBA-15 or MCM-41 with an appropriate amount of aqueous solution of silver nitrate ($AgNO_3$). The weight ratios of silver nitrate to the support for $AgNO_3$/SBA-15 and $AgNO_3$/MCM-41 were, respectively, 0.43 and 0.60, based on estimate for monolayer spreading of $AgNO_3$. First, a 1.2 M solution of $AgNO_3$ was prepared. A volume of solution equal to the total pore volume of sample was introduced and mixed with the support so that a weight ratio of 0.43 or 0.60 was achieved. The sample was then heated for 12 h at 105 ^oC in air to remove the water.[28-30] Before its use, the sample was heated *in situ* at 105 ^oC in flowing nitrogen. In the earlier work of Padin

and Yang,[29] the dispersion of $AgNO_3$ on various supports (including mesoporous silica MCM-41), by various methods (including spontaneous thermal spreading and wet impregnation, as used here), and detail characterization have been discussed. The appropriate temperatures of sample treatment (as used in this work) have also been discussed.

Cu(I)Y (VPIE, i.e., vapor-phase ion exchange) adsorbent was synthesized following the previous recipe developed in our laboratory.[5] The particle or crystal sizes of the CuY zeolite were around 0.5 micron. SBA-15 consisted of rope-like domains with sizes of around 1 micron, which were aggregated, whereas MCM-41 consisted of irregular spheres with sizes of 1-3 microns.

Adsorbent characterization. The BET surface areas of the samples were measured by physical adsorption of N_2 at −196 ^oC using Micromeritics ASAP 2010. Pore size distribution was also analyzed by N_2 adsorption at −196 ^oC. The BJH method was used for calculating the mean pore size and pore volume.[37]

Reagents. A JP-5 jet fuel sample obtained from the Naval Business Center, NAVSEA, Philadelphia, was used in the desulfurization experiments. The sulfur concentration of the JP-5 was analyzed with a flame photometric detector - gas chromatograph (FPD-GC). For the JP-5 samples, the as-received JP-5 with 1172 ppmw total sulfur concentration and a light fraction of the JP-5 with 841ppmw sulfur concentration were used. The analysis result of 1172 ppmw-S concentration can be found in our previous work,[3] and the analysis result for the JP-5 light fraction is shown in Figure 49.

A model fuel with 150 ppmw total sulfur concentration was also prepared in this work as follows: 10 ml benzene and 90 ml n-octane were well mixed first, and then 0.0226g benzothiophene and 0.0251g methyl-benzothiophene were dissolved in the above solution and well stirred. After well mixed, the model jet fuel was kept in the flask. The corresponding analysis result is also shown in Figure 49. The sulfur concentrations were 75 ppmw-S for both benzothiophene and methyl-benzothiophene, or total 150 ppmw-S.

Fixed-bed adsorption/breakthrough experiments. All dynamic adsorption or breakthrough experiments were performed in a vertical custom-made quartz adsorber equipped with a supporting glass frit as described elsewhere.[31] The setup consisted of a low-flow liquid pump, feed tanks, and a heating element. Initially, the adsorbent was loaded inside the adsorber, and pretreated *in situ* using dry gases to avoid exposure to atmospheric moisture. The gases used for activation were pretreated (dried) inline before contacting the adsorbent using a column of 3A-type zeolite. After activation treatment, the adsorbent bed was washed with a sulfur free hydrocarbon (e.g., *n*-octane) to remove any entrapped gas. After allowing the liquid hydrocarbon head to disappear, the fuel was allowed to contact the bed in a down-flow direction. The effluent was sampled periodically until saturation was achieved, which depended on the adsorption dynamics and the amount of adsorbent.

Breakthrough adsorption curves were generated by plotting the transient total sulfur concentration normalized by the feed total sulfur concentration versus cumulative fuel volume normalized by total adsorbent weight. The adsorption amounts (normalized per adsorbent weight) were obtained by integration.[31]

Gas chromatographic analysis. All the fuels from the desulfurization of JP-5 collected during the breakthrough experiments were analyzed using a Shimadzu GC-17A v3 unit equipped with an EC-5 capillary column and a flame photometric detector (FPD). The sulfur detection limit was approximately 50 ppb. More details on the GC analysis could be found elsewhere.[31]

Adsorbent regeneration. In this work, the feasibility for regeneration of the $AgNO_3$/MCM-41 was investigated by heating the spent $AgNO_3$/MCM-41 adsorbent in flowing air. The saturated sample (1.0 g) by JP-5 was heated at 200 ^oC for 24 h in flowing air of 50 mL/min. Afterward, the regenerated sorbent was further tested for desulfurization of JP-5.

***Ab initio* molecular orbital computation.** The nature and bond energy for π-complexation bonding between the sorbate molecule and sorbent metal site can be calculated and understood by molecular orbital (MO) theory. Molecular orbital studies on the π-complexation bonding for thiophene, benzene, benzothiophene and 4,6-dimethyldibenzothiophene on sorbent surfaces and zeolites have been reported in our earlier work.[32] In this work, similar MO studies were extended to a new sorbent, silver nitrate, and with an additional adsorbate, 2-methybenzothiophene. The Gaussian 03 package[33] and Cerius2 molecular modeling software (Cerius2, version 4.6, Accelrys, San Diego, CA) were used for all MO calculations. Geometry optimizations were performed at density functional theory (DFT) level using effective core potentials (ECPs).[34]

Geometry optimization and bond energy calculations. Frequency analysis was used to verify that all geometry optimized structures were true minima on the potential

energy surface. The optimized structures were then used for bond energy calculations according to the following expression:

$$E_{ads} = E_{adsorbate} + E_{adsorbent} - E_{adsorbent\text{-}adsorbate} \quad (1)$$

where $E_{adsorbate}$ is energy of free adsorbate, $E_{adsorbent}$ is energy of free adsorbent and $E_{adsorbent\text{-}adsorbate}$ is energy of the adsorbate/adsorbent system. A higher value of E_{ads} corresponds to a stronger adsorption.

Results and discussion

Adsorbent characterization. Figure 50 shows the adsorption-desorption isotherms of N_2 at –196 ^oC for the SBA-15 and MCM-41 based adsorbents. Figure 51 shows the pore size distributions of SBA-15 and MCM-41 based adsorbents. The corresponding BET surface areas, pore sizes and pore volumes are listed in Table 7.

Molecular orbital calculation results. For the Cu-Y zeolite, a cluster model was chosen for the zeolite framework structure which represents well the chemistry of the zeolite.[32] The zeolite anion is denoted as Z^-. The adsorption bond energies for all relevant adsorbate molecules and three sorbents (CuZ, CuCl and $AgNO_3$) were calculated and are shown in Table 8.

First, it is seen that the π-complexation bonding is stronger for thiophene than benzene for both Cu^+ and Ag^+. This result assures selectivity for thiophene over benzene by sorbents containing these cations, i.e., selective desulfurization. Also, from Table 8, it is seen that the π-complexation bonding for all aromatic adsorbate molecules is considerable stronger for Cu^+ than Ag^+, i.e., $Cu^+ > Ag^+$. These results are consistent with that reported earlier, and are also consistent with experimental heats of adsorption data.[35] Comparing different anions, it is seen that the zeolite anion (Z^-) is more electronegative than Cl^-, resulting in stronger π-complexation bonding with CuZ than CuCl. These results

indicate that CuY zeolite would be the best sorbent for desulfurization (without considering the pore diffusion/limitation effects).

Fixed-bed adsorption experiment. From Figure 52 and Table 9, it can be seen that the $AgNO_3$/SBA-15 adsorbent was capable of removing 0.32 and 0.91 mmol of sulfur per gram at breakthrough and saturation, respectively. A significant or detectable breakthrough (~10 ppmw S) occurred at about 10.0 mL/g for 1.0 g of $AgNO_3$/SBA-15. In comparison, the pure SBA-15 adsorbent could only remove 0.01 and 0.17 mmol of sulfur per gram at breakthrough and saturation, respectively. It was concluded that $AgNO_3$ was an effective selective metal salt for removing sulfur compounds from jet fuel.

Figure 52 also shows the desulfurization performance for JP-5 on MCM-41 and $AgNO_3$/MCM-41 adsorbents. Table 9 summarizes the results obtained from the corresponding breakthrough and saturation curves. The $AgNO_3$/MCM-41 adsorbent exhibited higher adsorption capacity that was capable of removing 0.49 and 1.0 mmol of sulfur per gram at breakthrough and saturation, respectively. As seen in Figure 52, nearly 15.0 mL of product fuel in which sulfur concentration was less than 10.0 ppmw could be obtained by the desulfurization of JP-5 (1172 ppmw S) with the fresh $AgNO_3$/MCM-41 adsorbent. It can be seen that the sulfur capacity of $AgNO_3$/MCM-41 for JP-5 was higher than that of $AgNO_3$/SBA-15. From Table 7, the $AgNO_3$/MCM-41 contained more silver than that of $AgNO_3$/SBA-15, 2.21 vs. 1.17 mmol/g. In addition, the BET surface area of $AgNO_3$/MCM-41 was larger than that of $AgNO_3$/SBA-15, 490 m^2/g vs. 408 m^2/g. However, the average pore size of $AgNO_3$/MCM-41 was smaller than that of $AgNO_3$/SBA-15, 19.1Å vs. 48.8Å. The pore volume of $AgNO_3$/MCM-41 was smaller than that of $AgNO_3$/SBA-15, 0.27 cm^3/g vs. 0.55 cm^3/g. Since the pore sizes for both

sorbents were considerably larger compared with the sizes of the sorbate (sulfur) molecules, the pore size difference (19.1Å vs. 48.8Å) is not a factor in determining the desulfurization performance, as we have observed previously with similar mesoporous sorbent materials.[27] The higher sulfur capacity of the $AgNO_3$/MCM-41 was likely caused by the larger BET surface area and higher silver loading of the adsorbent. From these results, MCM-41 was a better support than SBA-15 for the $AgNO_3$ supported adsorbents in the desulfurization of JP-5. This order was in agreement with our previous conclusion for the desulfurization of JP-5 by SBA-15 and MCM-41 supported cuprous oxide.[28] Table 9 also shows the ratios of the adsorbed sulfur molecules per silver cation at breakthrough and saturation. It can be seen that the ratios of sulfur to sliver metal were 0.51 and 0.45 mmol/mmol for $AgNO_3$/SBA-15 and $AgNO_3$/MCM-41 at saturation, respectively. This result indicates that during the desulfurization of JP-5, almost equal utilization of $AgNO_3$ occurred on $AgNO_3$/SBA-15 and $AgNO_3$/MCM-41. This is in agreement with the above conclusion that the diffusion of sulfur compounds is not a key factor for these adsorbents.

The pore (or aperture) size of the CuY zeolite is approximately 7 Å. It is similar to that of the sulfur molecules in the jet fuel (i.e., alkyl-benzothiophenes). The strong diffusion limitation of desulfurization was manifested by the long residence time that were needed for desulfurization. The strong diffusion limitation has also been shown by the strong dependence of desulfurization on the flow rates.[36]

The desulfurization results on Cu(I)Y (VPIE) and $AgNO_3$/MCM-41 were also compared as shown in Figures 5-7. Figure 53 gives a direct comparison between these two sorbents for the model jet fuel. The model jet fuel contained only benzothiophene

and methyl-benzothiophene (at 75 ppmw-S each). As seen from Figure 49, the main sulfur compounds in the JP-5 were alkylated benzothiophenes with much larger molecules. As shown above, Cu^+ forms stronger bonds with the sulfur molecules than Ag^+. For the model fuel, the sulfur molecules were sufficiently small compare to the aperture size of the Cu(I)Y zeolite, hence diffusion was not a factor for the desulfurization performance. As a result, the sulfur capacity of Cu(I)Y was higher than that of $AgNO_3$/MCM-41 for the model fuel, as shown in Figure 53.

Figures 54 and 55 show the sulfur breakthrough curves for the light fraction of JP-5 (841 ppmw-S) on these two sorbents. It is seen that the desulfurization capacity of the $AgNO_3$/MCM-41 was much higher than that of Cu(I)Y zeolite. This result is a manifestation of the pore diffusion limitation for the sulfur molecules in the Cu(I)Y zeolite (~7 Å pores), as compared with the case of $AgNO_3$/MCM-41 with ~19 Å pores. The sulfur molecules in the JP-5 were mostly dimethylbenzothiophene, trimethylbenzothiophene and a small amount of tetramethylbenzothiophene, while that in model jet fuel were benzothiophene and methylbenzothiophene. So the larger sulfur molecules in JP-5 light fraction could diffuse more freely in the large pores of $AgNO_3$/MCM41 and not so in the much smaller pores of Cu(I)Y. As a result, $AgNO_3$/MCM41 showed better desulfurization result for JP-5.

Adsorbent regeneration. After saturation by JP-5, regeneration of the spent $AgNO_3$/MCM-41 was conducted *in situ* by heating in flowing air at 200 ^oC for 24 h. Figure 56 shows the total sulfur breakthrough curves for JP-5 (1172 ppmw S) with fresh $AgNO_3$/MCM-41 and regenerated $AgNO_3$/MCM-41 sorbents. Three desulfurization-regeneration cycles were performed. There was some loss of the sulfur capacity after the

first cycle. However, there was no further loss after the second cycle, as shown in Figure 56. The sulfur capacities at breakthrough and saturation over the fresh sorbent and regenerated sorbents are listed in Table 10. The results show that approximately 0.16 mmol of sulfur per gram at breakthrough can be removed, for the second and third regeneration cycles. From Figure 56, more than 5.0 ml of "sulfur free" (well below 1 ppm) fuel can be obtained over 1.0 g of regenerated $AgNO_3$/MCM-41 sorbents after the second regeneration cycle. Nearly 50% total sulfur capacity of fresh sorbent could be recovered at saturation.

As mentioned, metal halides supported on MCM-41 and SBA-15 and Cu_2O supported on the same mesoporous silics supports have been studied for the desulfurization of JP-5.[26-27] A comparison of the results showed that $AgNO_3$/MCM-41 was superior because it yielded the largest regenerable "sulfur free" fuel product. It is concluded that the $AgNO_3$/MCM-41 sorbent is the best sorbent for desulfurization of high sulfur jet fuels.

Conclusion

Desulfurization of a JP-5 (1172 ppmw S) for on-board fuel cell applications was investigated by π-complexation adsorption with SBA-15 or MCM-41 supported $AgNO_3$. It was found that significant breakthrough occurred near 15.0 mL/g for desulfurization of the JP-5 by $AgNO_3$/MCM-41. The spent $AgNO_3$/MCM-41 was regenerated by heating in air at 200^oC, and the regenerated adsorbent was tested for re-use. The results showed that ~ 50% of the sulfur capacity could be recovered for re-use. Compared with all sorbents developed for the high sulfur jet fuels, $AgNO_3$/MCM-41 showed the best desulfurization performance.

Acknowledgments

This work was supported by NSF Grant CBET 0852129 and Office of Naval Research via NAVSEA. Discussions with Mr. John M. Heinzel and Dr. Donald J. Hoffman were helpful.

Note

The contents of this chapter have been published in Chem. Eng. Sci. 2009, 64, 5240.

References:

1. Hernández-Maldonado, A.J., Yang, R.T., Desulfurization of Transportation Fuels by Adsorption. Catalysis Reviews - Science and Engineering 2004, 46, 111-150.
2. Ma, X.L., Sun, L., Song, C.S., A New Approach to Deep Desulfurization of Gasoline, Diesel fuel and Jet Fuel by Selective Adsorption for Ultra-Clean Fuels and for Fuel Cell Applications. Catalysis Today 2002, 77, 107-116.
3. Wang, Y.H., Yang, F.H., Yang, R.T., Heinzel, J.M., Nickens, A.D., Desulfurization of High-Sulfur Jet Fuel by Pi-Complexation with Copper and Palladium Halide Sorbents. Industrial and Engineering Chemistry Research 2006, 45, 7649-7655.
4. Heinzel, J., Cervi, M., Hoffman, D., Nickens, A., Kuseian, J., 2005. Fuel Cell System Models for US Navy Shipboard Application. In: USFCC Fuel Cell Seminar, Palm Springs, CA.
5. Hernández-Maldonado, A.J., Yang, R.T., 2004b. Desulfurization of Diesel Fuels by Adsorption via π-Complexation with Vapor-Phase Exchanged Cu(I)−Y Zeolites. Journal of the American Chemical Society 126, 992-993.
6. Haji, S., Erkey, C., 2003. Removal of Dibenzothiophene from Model Diesel by Adsorption on Carbon Aerogels for Fuel Cell Applications. Industrial and Engineering Chemistry Research 42, 6933-6937.
7. McKinley, S.G., Angelici, R.J., 2003. Deep Desulfurization by Selective Adsorption of Dibenzothiophenes on Ag+/SBA-15 and Ag+/SiO2. Chemical Communications, 2620-2621.
8. Chica, A., Strohmaier, K., Iglesia, E., 2004. Adsorption, Desorption, and Conversion of Thiophene on H-ZSM5. Langmuir 20, 10982-10991.
9. Jeevanandam, P., Klabunde, K.J., Tetzler, S.H., 2005. Adsorption of Thiophenes out of Hydrocarbons Using Metal Impregnated Nanocrystalline Aluminum Oxide. Microporous and Mesoporous Materials 79, 101-110.
10. Kim J.H., Ma X.L., Zhou A.N., Song C.S., 2006. Ultra-deep Desulfurization and Denitrogenation of Diesel Fuel by Selective Adsorption over Three Different Adsorbents: A Study on Adsorptive Selectivity and Mechanism. Catalysis Today 111, 74-83.
11. King, D.L., Faz, C., 2006. Desulfurization of Tier 2 Gasoline by Divalent Copper-Exchanged Zeolite Y. Applied Catalysis A 311, 58-65.
12. Jiang, M., Ng, F.T.T., 2006. Adsorption of Benzothiophene on Y Zeolites Investigated by Infrared Spectroscopy and Flow Calorimetry. Catalysis Today 116, 530-536.
13. Laborde-Boutet, C., Joly, G., Nicolaos, A., Thomas, M., Magnoux, P., 2006. Selectivity of Thiophene/Toluene Competitive Adsorptions onto NaY and NaX Zeolites. Industrial and Engineering Chemistry Research 45, 6758-6764.
14. Etemadi, O., Yen T.F., 2007. Surface Characterization of Adsorbents in Ultrasound-Assisted Oxidative Desulfurization Process of Fossil Fuels. Journal of Colloid and Interface Science 313, 18-25.
15. Yang, L.M., Wang, Y.J., Huang, D., Luo, G.S., Dai, Y.Y., 2007. Preparation of High Performance Adsorbents by Functionalizing Mesostructured Silica Spheres for Selective Adsorption of Organosulfur Compounds. Industrial and Engineering Chemistry Research 46, 579-583.

16. Seredych, M., Bandosz, T.J., 2007. Template-Derived Mesoporous Carbons with Highly Dispersed Transition Metals as Media for the Reactive Adsorption of Dibenzothiophene. Langmuir 23, 6033-6041.
17. Ko, C.H., Park, J.G., Park, J.C., Song, H., Han, S.S., Kim, J.N., 2007. Surface Status and Size Influences of Nickel Nanoparticles on Sulfur Compound Adsorption. Applied Surface Science 253, 5864-5867.
18. Yang, X.X., Cao, C.D., Klabunde, K.J., Hohn, K.L., Erickson, L.E., 2007. Adsorptive Desulfurization with Xerogel-Derived Zinc-Based Nanocrystalline Aluminum Oxide. Industrial and Engineering Chemistry Research 46, 4819-4823.
19. Nuntang S., Prasassarakich, P., Ngamcharussrivichai, C., 2008. Comparative Study on Adsorptive Removal of Thiophenic Sulfurs over Y and USY Zeolites. Industrial and Engineering Chemistry Research 47, 7405-7413.
20. Landau, M.V., Herskowitz, M., Agnihotri, R., Kegerreis, J.E., 2008. Ultradeep Adsorption−Desulfurization of Gasoline with Ni/Al−SiO2 Material Catalytically Facilitated by Ethanol. Industrial and Engineering Chemistry Research 47, 6904-6916.
21. Yang, H.Y., Sothen, R., Cahela, D.R., Tatarchuk, B.J., 2008. Breakthrough Characteristics of Reformate Desulfurization Using ZnO Sorbents for Logistic Fuel Cell Power Systems. Industrial and Engineering Chemistry Research 47, 10064-10070.
22. Landau, M.V., Herskowitz, M., Hoffman, T., Fuks, D.; Liverts, E., Vingurt, D., Froumin, N., 2009. Ultradeep Hydrodesulfurization and Adsorptive Desulfurization of Diesel Fuel on Metal-Rich Nickel Phosphides. Industrial and Engineering Chemistry Research, Articles ASAP.
23. Jeon, H.J., Ko, C.H., Kim, S.H., Kim, J.N., 2009. Removal of Refractory Sulfur Compounds in Diesel Using Activated Carbon with Controlled Porosity. Energy Fuels, Articles ASAP.
24. Heinzel, J., Cervi, M., Hoffman, D., Nickens, A., 2006. Advances in Logistic Fuels Desulfurization. American Chemical Society, San Francisco, CA.
25. Wang, Y.H., Yang. R.T., 2007. Desulfurization of Liquid Fuels by Adsorption on Carbon-Based Sorbents and Ultrasound-Assisted Sorbent Regeneration. Langmuir 23, 3825-3831.
26. Wang, Y.H., Yang, R.T., Heinzel, J.M., 2008. Desulfurization of Jet Fuel by π-Complexation with Metal Halides Supported on MCM-41 and SBA-15 Mesoporous Materials. Chemical Engineering Science 63, 356-365.
27. Wang Y.H., Yang R.T., Heinzel, J.M., 2009. Desulfurization of Jet Fuel JP-5 by MCM-41 and SBA-15 Supported Cuprous Oxide for Fuel Cell Applications. Industrial and Engineering Chemistry Research 48, 142-147.
28. Padin, J., Yang, R.T., 1999. New Sorbents for Olefin/Paraffin Separations and Olefin Purification for C4 ydrocarbons. Desulfurization of Jet Fuel JP-5 by MCM-41 and SBA-15 Supported Cuprous Oxide for Fuel Cell Applications 38, 3614-3621.
29. Padin, J., Yang, R.T., 2000. New Sorbents for Olefin-Paraffin Separations by Adsorption via π-Complexation: Synthesis and Effects of Substrates. Chemical Engineering Science 55, 2607-2616.

30. Xie, Y.C., Tang, Y.Q., 1990. Spontaneous Monolayer dispersion of Oxides and Salts onto Surfaces of Supports: Applications to Heterogeneous Catalysis. Advances in Catalysis 37, 1-43.
31. Hernández-Maldonado, A.J., Qi, G.S., Yang, R.T., 2005. Desulfurization of Commercial Fuels by π-Complexation: Monolayer CuCl/γ-Al2O3. Applied Catalysis B 61, 212-218.
32. Yang, F.H., Hernández-Maldonado, A.J., Yang, R.T., 2005. Selective Adsorption of Organosulfur Compounds from Transportation Fuels by π-Complexation. Separation Science Technology 39, 1717-1732.
33. Frisch, M.J., Trucks, G.W., Schlegel, H.B., 2004. Gaussian, Inc., Wallingford CT.
34. Russo, T.V., Martin, R.L., Hay, P.J., 1995. Journal of physical chemistry 99, 17085-17087.
35. Yang, R.T., Hernandez-Maldonado, A.J., Yang, F.H., 2003. Desulfurization of Transportation Fuels with Zeolites under Ambient Conditions. Science 301, 79-81.
36. Li, Y.W., Yang, F.H., Qi, G.S., Yang, R.T., 2006. Effects of Oxygenates and Moisture on Adsorptive Desulfurization of Liquid Fuels with Cu(I)Y Zeolite. Catalysis Today 116, 512-518.
37. Barrett, E., Joyner, L., Halenda, P., 1951. The Determination of Pore Volume and Area Distributions in Porous Substances. I. Computations from Nitrogen Isotherms. Journal of the American Chemical Society 73, 373-380.

adsorbent	metal loading (mmol/g)	BET surface area (m^2/g)	BJH pore size (Å) [a]	BJH pore volume (cm^3/g) [b]
SBA-15	-	901	58.7	1.14
$AgNO_3$/SBA-15	1.77	408	48.8	0.55
MCM-41	-	1225	28.7	1.17
$AgNO_3$/MCM-41	2.21	490	19.1	0.27

[a] BJH desorption average pore diameter (4V/A). [b] BJH desorption cumulative pore volume.

Table 7. N_2 adsorption characterization of different adsorbents

Adsorbate	ΔE on CuZ[a]	ΔE on CuCl	ΔE on $AgNO_3$
Thiophene	21.4	13.5	10.6
Benzene	20.5	12.4	10.1
Benzothiophene	22.9	16.2	12.0
4,6-Dimethyldibenzothiophene	23.5	18.4	13.6
2-Methylbenzothiophene	23.3	17.2	13.2

[a]. CuZ: Z denotes zeolite anion using cluster model for zeolite framework.

Table 8. Energy of adsorption (ΔE, in kcal/mol) for different adsorbate/adsorbent (Z: zeolite anion using cluster model)

adsorbent	adsorption capacity (mmol S/g)		ratio of sulfur on metal (mmol/mmol) [b]	
	breakthrough [a]	saturation	breakthrough [a]	saturation
SBA-15	0.01	0.17	-	-
$AgNO_3$/SBA-15	0.32	0.91	0.18	0.51
MCM-41	0.02	0.22	-	-
$AgNO_3$/MCM-41	0.49	1.0	0.22	0.45

[a] The concentration of sulfur was ~10 ppmw S at breakthrough. [b] 1.77 mmol/g of silver on SBA-15 adsorbent or 2.21 mmol/g of silver on MCM-41 adsorbent.

Table 9. Sulfur capacity at breakthrough and saturation over fresh adsorbents for JP-5 (1172 ppmw S)

adsorbent	breakthrough loading (mmol/g) [a]	saturation loading (mmol/g)
fresh	0.49	1.0
1st regen'd $AgNO_3$/MCM-41	0.16	0.50
2nd regen'd $AgNO_3$/MCM-41	0.16	0.52

[a] The concentration of sulfur was ~10 ppmw S at breakthrough.

Table 10. Sulfur capacity at breakthrough and saturation over regenerated $AgNO_3$/MCM-41 for JP-5 (1172 ppmw-S)

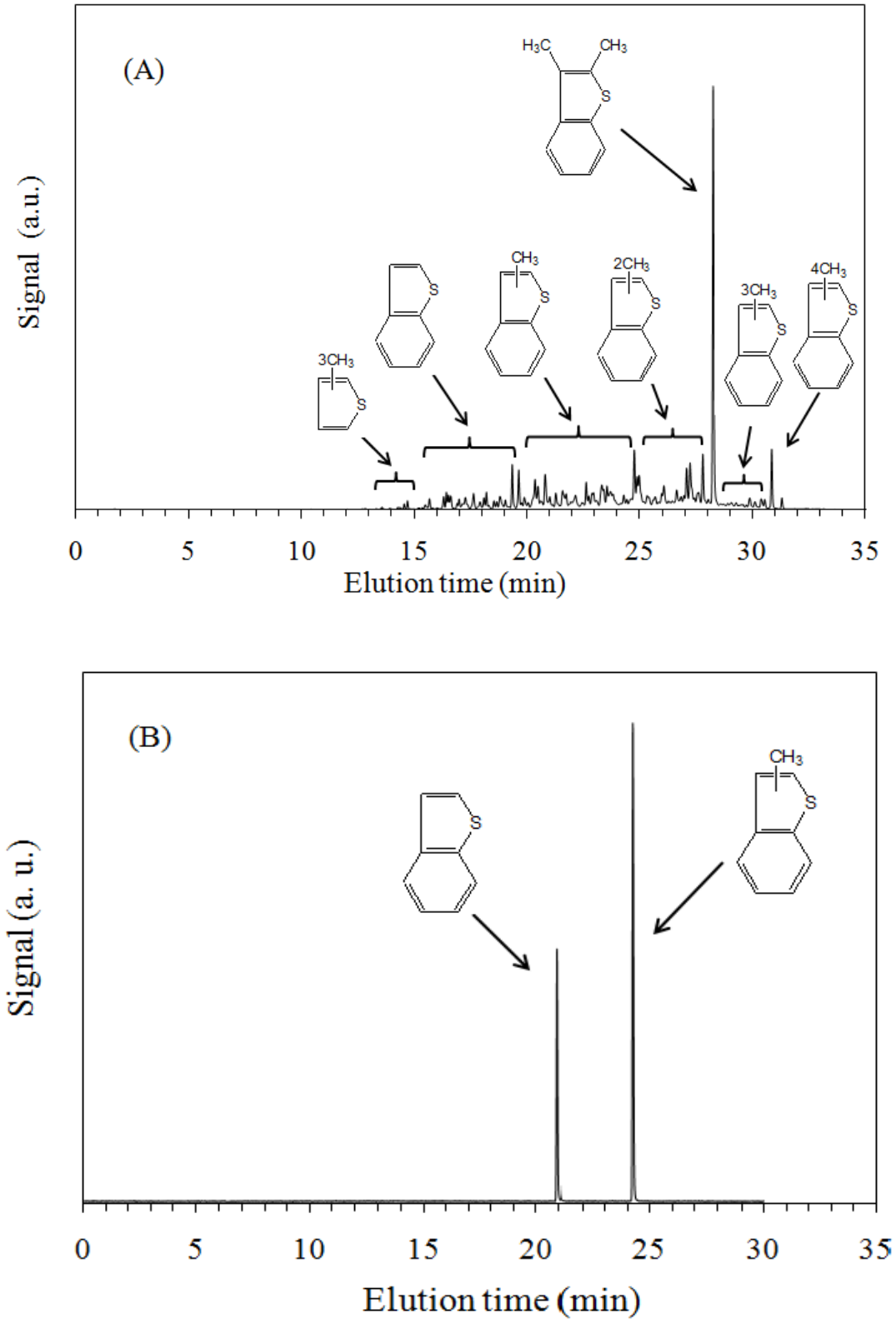

Figure 49. GC-FPD chromatograms of JP-5 light fraction (A) and model jet fuel (B)

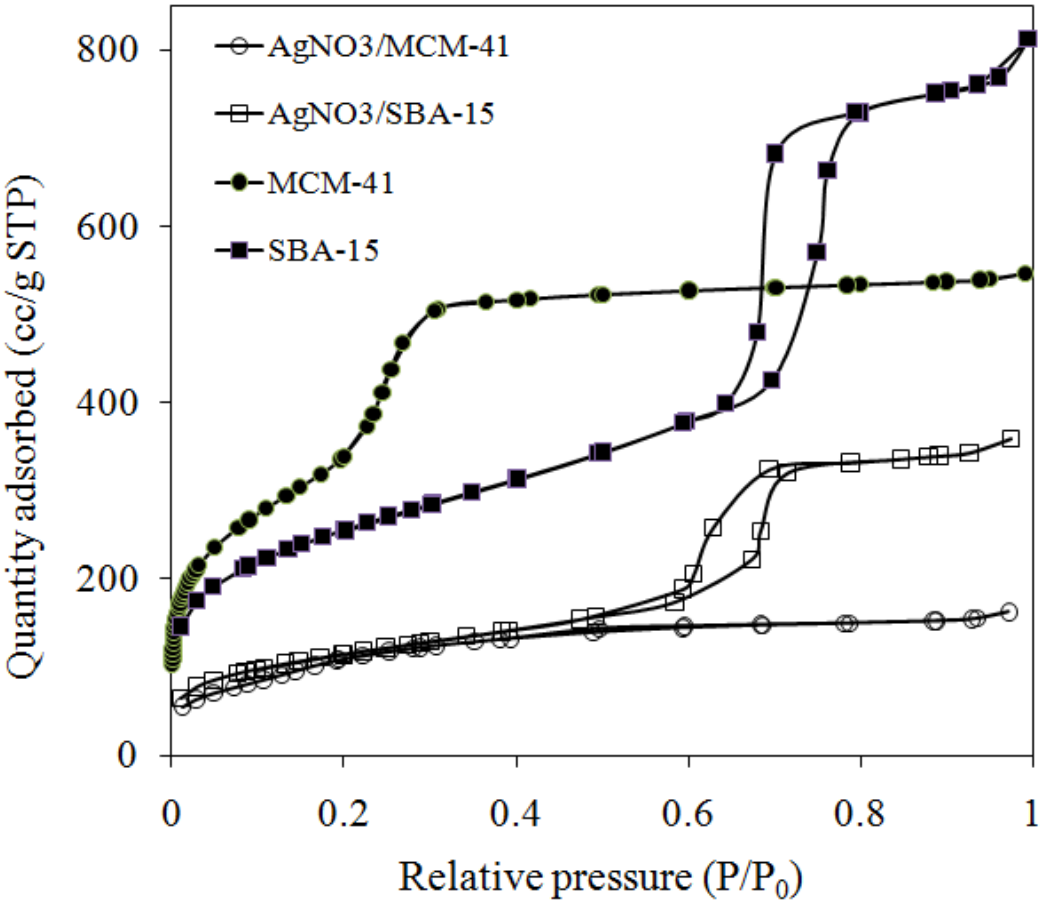

Figure 50. Nitrogen adsorption-desorption isotherm plots for SBA-15 (■) MCM-41 (●), $AgNO_3$/SBA-15 (□) and $AgNO_3$/MCM-41 (○); P_0 is 760mmHg.

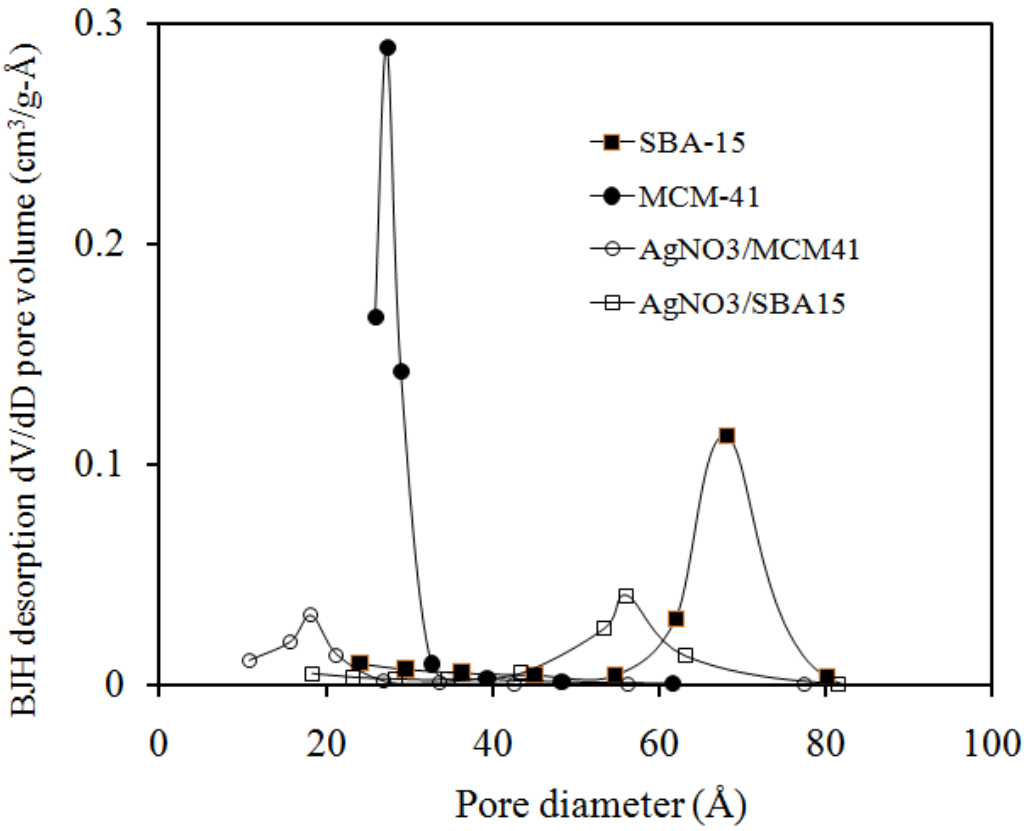

Figure 51. BJH pore volume plots of SBA-15 (■), MCM-41 (●), $AgNO_3$/SBA-15 (□) and $AgNO_3$/MCM-41 (○).

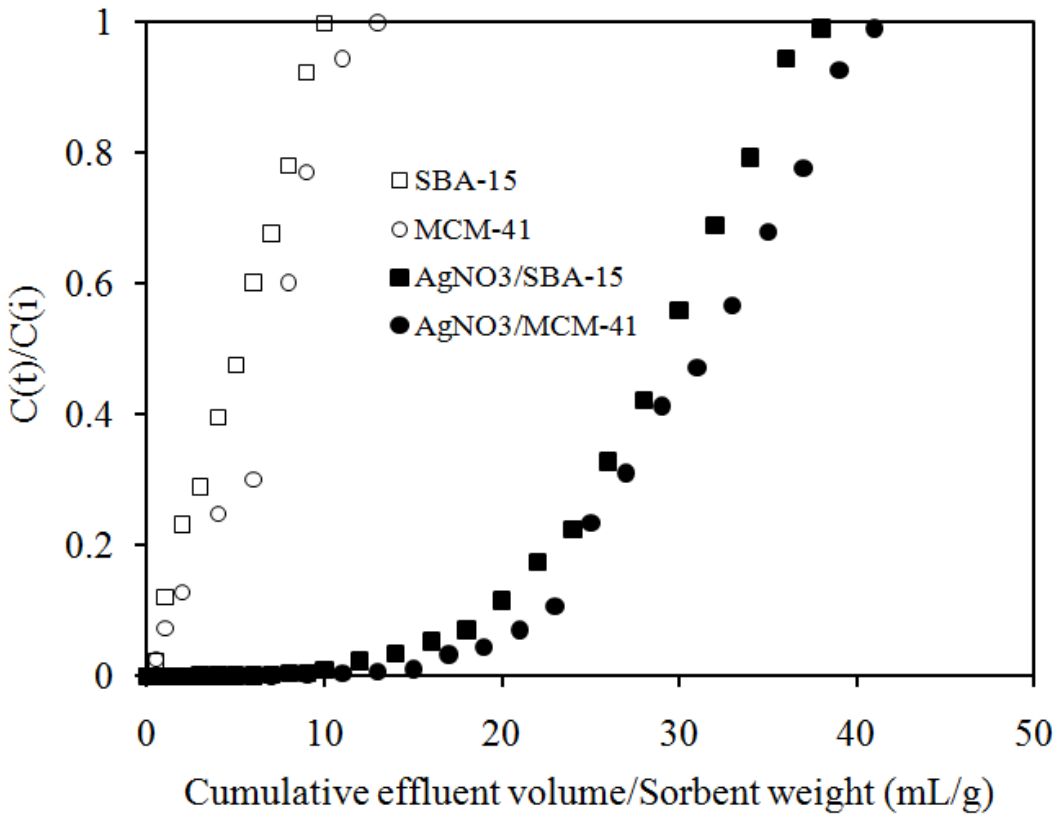

Figure 52. Breakthrough of total sulfur in a fixed-bed adsorber with SBA-15 (□), MCM-41 (○), monolayer $AgNO_3$/SBA-15 (■).and monolayer $AgNO_3$/MCM-41 (●) for JP-5 Jet fuel (1172 ppmw-S) at room temperature. Ci is the total sulfur concentration of the feed at flow rate 1.0 mL/40 min, based on 1 gram of sorbents (S.V. = 1.25 h^{-1}).

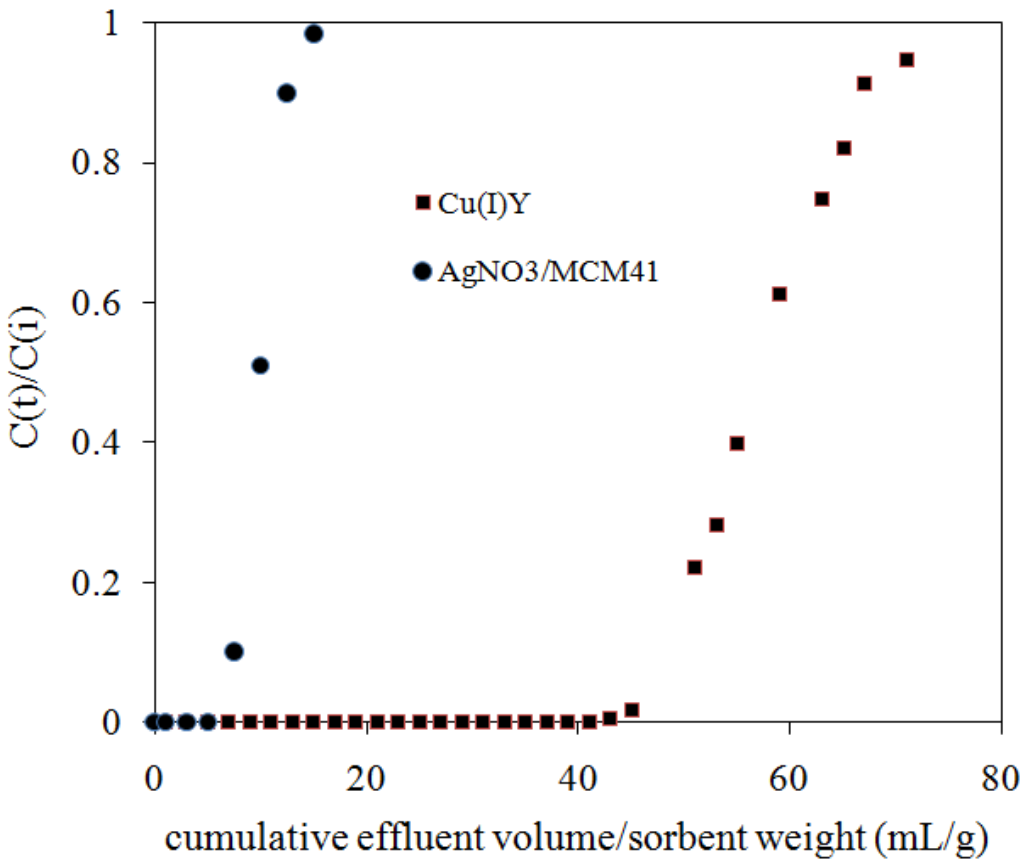

Figure 53. Breakthrough of total sulfur in a fixed-bed adsorber with Cu(I)Y and $AgNO_3$/MCM-41 for Model Jet fuel (150 ppmw-S) at room temperature. C_i is the total sulfur concentration of the feed at flow rate 1.0 mL/40 min, based on 1 gram of sorbents (S.V. = 1.25 h^{-1}).

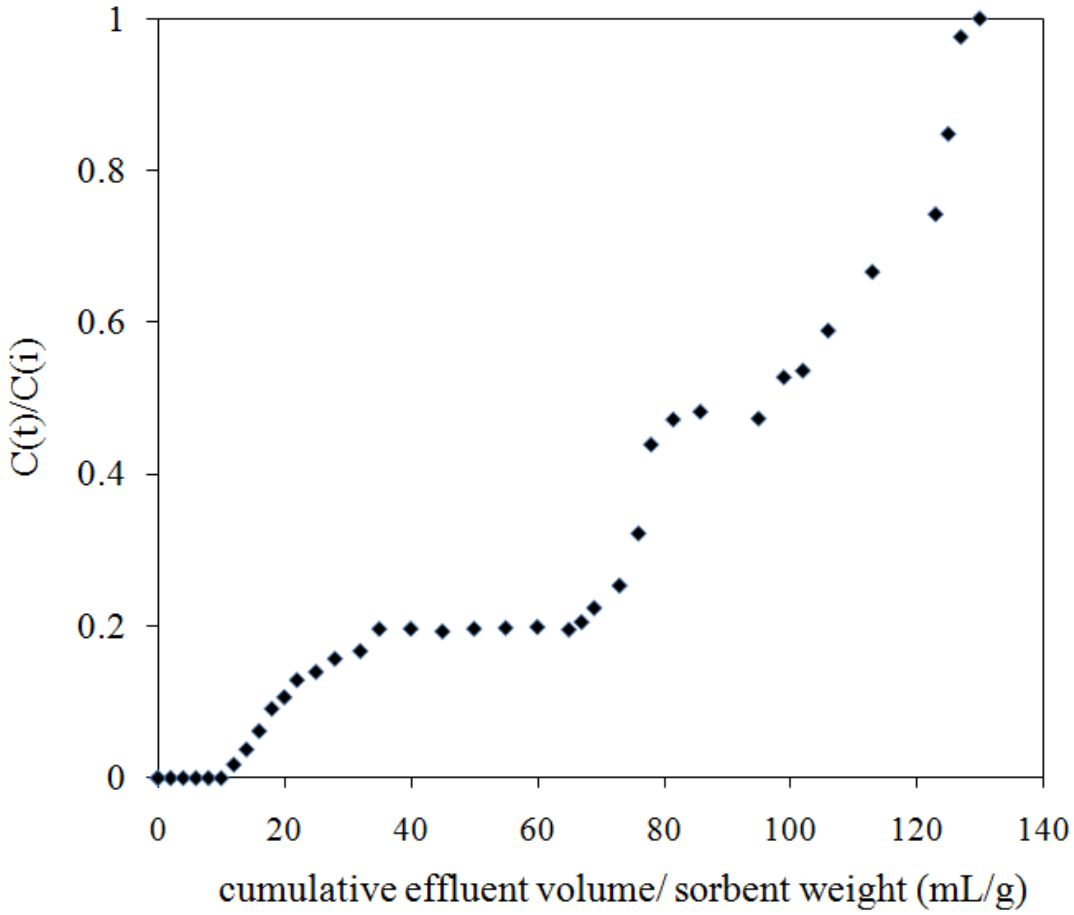

Figure 54. Breakthrough of total sulfur in a fixed-bed adsorber with $AgNO_3$/MCM-41 for JP-5 light fraction (841 ppmw-S) at room temperature. C_i is the total sulfur concentration of the feed at flow rate 1.0 mL/40 min, based on 1 gram of sorbents (S.V. = 1.25 h^{-1}).

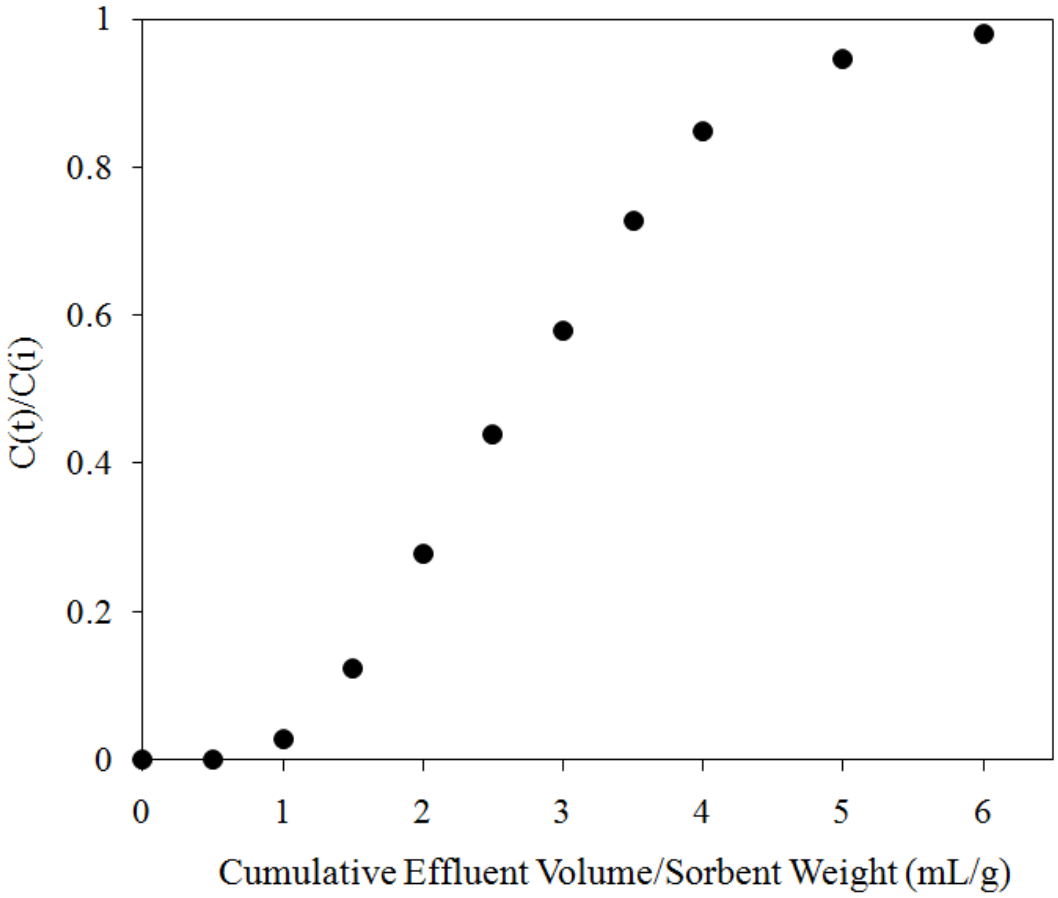

Figure 55. Breakthrough of total sulfur in a fixed-bed adsorber with Cu(I)-Y (VPIE), for JP-5 light fraction (841 ppmw-S) at room temperature. Ci is the total sulfur concentration of the feed at flow rate 1 mL/20 min, based on 1 gram of sorbents (S.V. = 2.5 h^{-1})

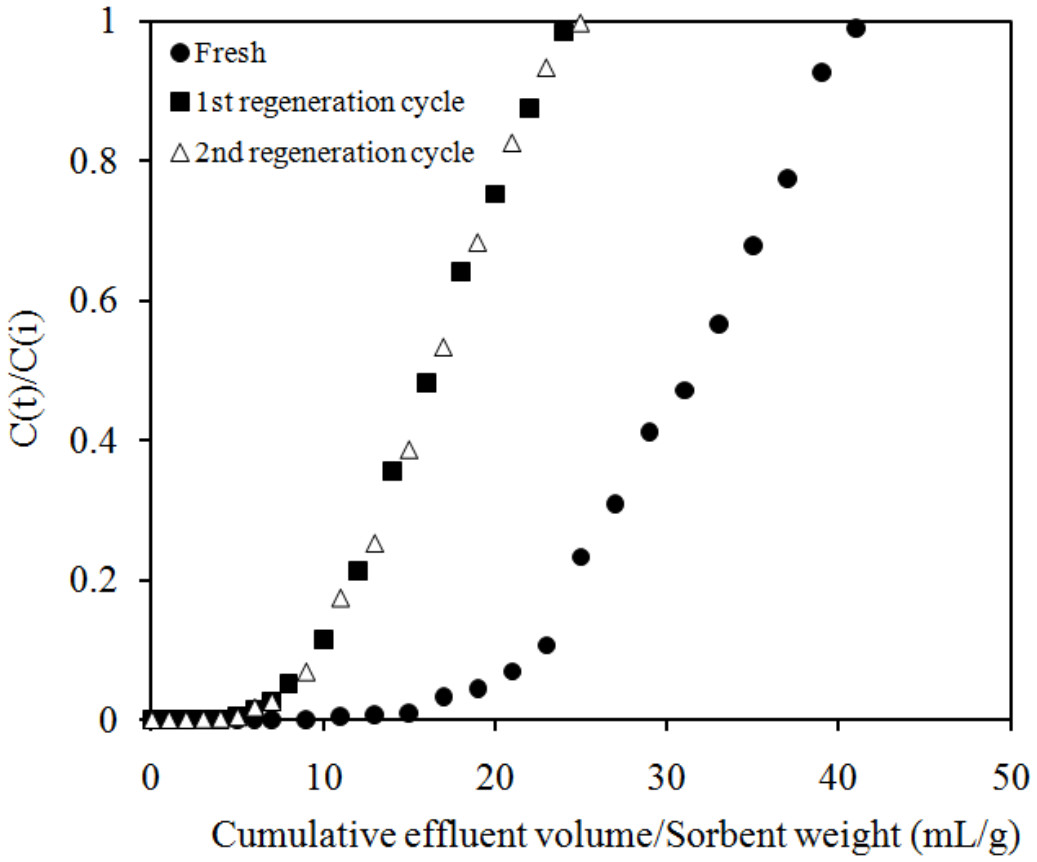

Figure 56. Breakthrough of total sulfur in a fixed-bed adsorber with fresh and regenerated $AgNO_3$/MCM-41 for JP-5 Jet fuel (1172 ppmw-S) at room temperature. Ci is the total sulfur concentration of the feed at flow rate 1.0 mL/40 min, based on 1 gram of sorbents (S.V. = 1.25 h^{-1}).

Chapter 6: Conclusions and Perspectives

This section summarized the previous results and made some perspectives for future work. From Chapter 1, it was found that TiF_3 is an effective catalyst for hydrogen spillover on Pt doped Maxsorb at 298K. Upon TiF_3 doping, the BET surface area and pore volume of the Pt/Maxsorb decreased slightly, and consequently the hydrogen uptake amount also decreased slightly. However, the hydrogen adsorption and desorption rates on Pt/Maxsorb after doping TiF_3 were 1.5 times that without TiF_3. Moreover, heat treatment of the doped TiF_3 at a higher temperature (675K vs. 475K) was found to be more effective, which could double both the hydrogen adsorption and desorption rates on Pt doped Maxsorb carbon. XPS analyses showed that C-F bonds were formed upon heat treatment and that the amount of C-F bonds increased with the heat treatment temperature. The catalytic effects also increased with the heat treatment temperature. Thus, the catalytic mechanism seems to involve the formation of the C-F bonds on the carbon edge sites.

From Chapter 2, a series of Pt-doped IRMOF-8 samples have been prepared via organometallic chemical vapor deposition. It was found that the catalyst (Pt) size was affected by the doping temperature and number of doping cycles. The hydrogen storage studies showed the storage capacities via hydrogen spillover on Pt-doped IRMOF-8 samples were enhanced by a factor 1.1 – 1.9 when compared to undoped IRMOF-8. Catalyst size was a crucial factor that determined the enhancements of the storage capacity of Pt-doped MOFs.

From Chapter 3, a series of Pt-doped HKUST-1, MIL-53 and ZIF-8 samples were synthesized via colloidal nanoparticles incipient wetness impregnation and CVD method. Their stabilities in the presence of dihyrogen molecules and dissociated hydrogen were

examined by XRD and XPS measurements. Al-based and Zn-based frameworks exhibited good stabilities in both dihydrogen molecules and dissociated hydrogen environments at elevated temperatures (up to 150°C). The structure of Cu-based framework HKUST-1 remained intact in dihydrogen environment but the structure of the Pt-doped HKUST-1 began to collapse upon exposure to H_2, as a result of spillover of the dissociated hydrogen. The degree of collapse increased with temperature. The stabilities of MOFs with different metal clusters in H_2 and dissociated hydrogen environments are related to the different reduction potentials of the metal elements. A further comparison of the stabilities of MOF-74 (with open coordination sites) and ZIF-8 (without open coordination sites) confirmed that the stability of MOF was related to reduction potential of metal in MOF not the presence/absence of open sites. This work provides useful information for future optimization of MOFs as hydrogen storage candidate materials, which should have good stabilities in the presence of H_2 or dissociated hydrogen at ambient as well as elevated temperatures. Moreover, significant difference in stabilities between Pt-HKU-CVD and Pt-HKU (via. incipient wetness) showed that the contacts between Pt metal and the framework played an important role in hydrogen spillover.

From Chapter 4, a series of TPD experiments were conducted on two Zn-ZSM-5 samples with different zinc concentration. It is found higher dosing temperature leads to higher activation energy for desorption, i.e., the interaction between hydrogen and Zn-ZSM-5 is stronger at higher dosing temperature. Meanwhile, more hydrogen chemisorbed on Zn-ZSM-5 at higher dosing temperature due to more external energy provided to overcome the energy barrier for hydrogen chemisorption. TPD studies also demonstrate that Zn cations play a significant role in hydrogen chemisorption on zeolites. Higher

concentration of zinc ions in zeolites will strengthen the interaction between hydrogen and zeolites, thus leads to more hydrogen chemisorbed on ZSM-5 but it requires higher temperature to release hydrogen due to stronger interaction between hydrogen and zeolites. This effect of Zn on hydrogen chemisorptions on zeolites is also influenced by the framework of zeolites. Different types of frameworks exhibited different behaviors for hydrogen chemisorptions (the amount of chemisorbed hydrogen, the strength of the interaction between chemisorbed hydrogen and zeolites).

From Figure 5, desulfurization of a JP-5 (1172 ppmw S) for on-board fuel cell applications was investigated by π-complexation adsorption with SBA-15 or MCM-41 supported $AgNO_3$. It was found that significant breakthrough occurred near 15.0 mL/g for desulfurization of the JP-5 by $AgNO_3$/MCM-41. The spent $AgNO_3$/MCM-41 was regenerated by heating in air at 200^oC, and the regenerated adsorbent was tested for re-use. The results showed that ~ 50% of the sulfur capacity could be recovered for re-use. Compared with all sorbents developed for the high sulfur jet fuels, $AgNO_3$/MCM-41 showed the best desulfurization performance.

Based on the above conclusions, several perspectives can be made. Although TiF_3 can increase the hydrogen sorption rates on metal-carbon system by a factor of 50%-100%, it still requires a long time to reach saturation compared with pristine adsorbents. Thus the development of more efficient and stable catalysts to facilitate hydrogen spillover will be desired for future industrial applications. More specifically, the other transition metal halides are worth to be tested for this purpose, e.g., ZrF_4, CrF_3, ZnF_2, etc. For the same metal cation, the more stable halides are preferred. Metal particle size was found to be a crucial factor influencing the final performance of metal doped adsorbents

for hydrogen storage at ambient conditions. However, it still lacks a good way to ensure small particles and even distribution. Moreover, considering the different properties of different metals, developing a general way as the guidance for future material synthesis adds more difficulties to the task. Further investigation of the mechanism of hydrogen spillover and the factors affecting hydrogen spillover will be very helpful to obtain the most promising adsorbent for hydrogen storage. One prerequisite for adsorbents application for hydrogen storage is that the materials should be stable in such environment. It has been shown that the reduction potential of metal clusters have a great impact on the stabilities of MOFs in hydrogen environment, especially in atomic hydrogen environment. From the point view of stabilities, Cu based MOF was not recommended. Moreover, the stabilities of MOFs against moisture are also important. Thus the future selection of proper MOFs for hydrogen storage requires comprehensive consideration on moisture/air stability, hydrogen stability, cost, life cycle, etc. Zinc ion was found to be a catalyst for hydrogen chemisorption on zeolites and previous literature has shown its effect on hydrogen dissociation in the process of propane dehydrogenation. However, preliminary results showed that the catalytic effect of zinc ion is not as significant as noble-metal catalysts. Thus a more effective catalyst is needed to reduce the cost and keep the catalytic activity. $AgNO_3$ doped on SBA-15 and MCM-41 was proved to be very effective for sulfur deep removal from jet fuel with high sulfur content. However, the stabilities of these two adsorbents upon desulfurization cycles are not satisfying (only 50% desulfurization capacity was recovered). A more efficient regeneration method needs to be developed to re-activate the adsorbents more thoroughly.